The University of Maine
DigitalCommons@UMaine

Electronic Theses and Dissertations | Fogler Library

12-2004

Temporal Variability of Satellite-Derived Chlorophyll and Sea Suface Temperature in the California Current

Kasey Legaard

Follow this and additional works at: http://digitalcommons.library.umaine.edu/etd

 Part of the Oceanography Commons

Recommended Citation
Legaard, Kasey, "Temporal Variability of Satellite-Derived Chlorophyll and Sea Suface Temperature in the California Current" (2004). *Electronic Theses and Dissertations*. 167.
http://digitalcommons.library.umaine.edu/etd/167

This Open-Access Thesis is brought to you for free and open access by DigitalCommons@UMaine. It has been accepted for inclusion in Electronic Theses and Dissertations by an authorized administrator of DigitalCommons@UMaine.

TEMPORAL VARIABILITY OF SATELLITE-DERIVED CHLOROPHYLL AND SEA SURFACE TEMPERATURE IN THE CALIFORNIA CURRENT

By

Kasey Legaard

B.S. Idaho State University, 2001

A THESIS

Submitted in Partial Fulfillment of the

Requirements for the Degree of

Master of Science

(in Oceanography)

The Graduate School

The University of Maine

December, 2004

Advisory Committee:

Andrew Thomas, Professor of Oceanography, Advisor

Mary Beard-Tisdale, Chairperson and Professor of Spatial Information Science and Engineering

Mary Jane Perry, Professor of Marine Sciences and Oceanography

TEMPORAL VARIABILITY OF SATELLITE-DERIVED CHLOROPHYLL AND SEA SURFACE TEMPERATURE IN THE CALIFORNIA CURRENT

By Kasey Legaard

Thesis Advisor: Dr. Andrew Thomas

An Abstract of the Thesis Presented
in Partial Fulfillment of the Requirements for the
Degree of Master of Science
(in Oceanography)
December, 2004

Physical forcing and biological response within the California Current coastal upwelling system are highly variable over a wide range of scales. Satellite remote sensing offers the only feasible means of quantifying this variability over the full extent of this current system. Here we quantify and compare patterns of physical and biological variability acting over seasonal, interannual and dominant intraseasonal time scales throughout the California Current System using more than five years (1997-2003) of daily SeaWiFS chlorophyll and NOAA/NASA AVHRR Oceans Pathfinder SST imagery. Mean seasonal cycles were modeled as the sum of annual and semiannual harmonics. Interannual variability was estimated by filtering non-seasonal time series. Dominant patterns of intraseasonal variability were determined using geostatistical semivariograms calculated from residual series following the removal of seasonal and interannual variability. We provide the first systematic and quantitative analysis of dominant temporal variability of chlorophyll and SST across the entire California Current System.

Coastal upwelling circulation dictates the nature of seasonal variability along northern and central California, where weak seasonal cycles of SST fluctuate between spring minima and late summer maxima and chlorophyll concentrations peak in mid- to late summer. Off northern California, chlorophyll summer maxima are bounded by the seasonally recurrent meandering path of the upwelling front and jet. Seasonal cycles along South-central Baja appear to be more strongly affected by processes other than local upwelling, and mesoscale circulation plays a lesser role in determining seasonally recurrent spatial distributions of chlorophyll. Seasonal cycles differ notably across the Pacific Northwest and within the inner Southern California Bight. Interannual variation is generally dominated by El Niño and La Niña conditions. Relative levels of sensitivity to basin-scale forcing differ between SST and chlorophyll at most locations. Dominant patterns of intraseasonal variability are caused by the seasonally recurrent formation, intensification and westward migration of the upwelling jet and surrounding eddies. The distortion of large-scale SST and chlorophyll distributions by prominent eddies and meanders defines a dominant time scale of ~60 days (equivalent to a dominant period of ~120 days) throughout much of the region. SST variance is shifted toward a time scale of ~40 days across much of the Pacific Northwest. Dominant chlorophyll variability is consistently shifted to 25-40 days inshore. Dominant scales of SST and chlorophyll variation deviate most markedly along the California coast between Point Conception (34.4° N) and Cape Mendocino (40.4° N), where major realignments of mesoscale currents may temporarily dissociate patterns of surface temperature and phytoplankton abundance.

ACKNOWLEDGEMENTS

I sincerely thank the SeaWiFS Science Project and the GSFC DAAC for access to SeaWiFS data, the NOAA/NASA AVHRR Oceans Pathfinder project and the JPL PO.DAAC for access to Pathfinder SST data, and the NOAA NDBC for access to buoy surface temperature data. Support for this project was provided under NASA grants NAG5-6558, -6004 and -10620, and NSF grant 0000899 (U.S. GLOBEC Program) awarded to Andrew Thomas.

I thank my major advisor, Andrew Thomas, for his patience and support throughout this project. I also thank Kate Beard and Mary Jane Perry for serving on my committee and for providing helpful advice and creative suggestions whenever needed, and Phaedon Kyriakidis for suggesting the use of EOF analysis as a means of summarizing semivariogram structure. I would like to extend my appreciation to Ryan Weatherbee and Steve Cousins for ensuring that the computers worked for me and not against me, and to Peter Brickley for always taking the time to think through my occasional questions.

I deeply thank my wife, Erin Simons, who makes everything possible. And finally, I owe my family and hers everything that I can give.

TABLE OF CONTENTS

LIST OF FIGURES

LIST OF SYMBOLS

$a(x)$	spatial amplitude function or principle component, dimensionless
$C(\cdot)$	covariance function, dimensionless
c_0	nugget semivariance, $(^{\circ}C)^2$ or $(\text{mg Chl m}^{-3})^2$
$E(\cdot)$	expectation function, dimensionless
$e(h)$	eigenvector or empirical orthogonal function, dimensionless
$f(h)$	general function of time lag, unspecified units
f_1	annual frequency, cycles yr^{-1}
f_2	semiannual frequency, cycles yr^{-1}
$\text{ind}(\cdot)$	presence / absence indicator transform function, dimensionless
K	number of time lags for which semivariance is calculated, dimensionless
M	number of grid locations at which time series are constructed and semivariograms are calculated, dimensionless
N	number of observations available at a given location or comprising the realization $z(t)$ of the stochastic process $Z(t)$, dimensionless
$n(h)$	number of pairs of observations separated by time lag h, dimensionless
r	semivariogram range, days
$\text{sdev}(\cdot)$	standard deviation function, dimensionless
$\text{var}(\cdot)$	variance function, dimensionless
$\langle X \rangle$	angle brackets denote the mean of the variable or expression enclosed within the brackets, unspecified units
$Z(t)$	time-dependent stochastic process or random function, unspecified units

$Z_{res}(t)$	residual time series obtained by removing seasonal and interannual variability, °C or mg Chl m^{-3}
$Z_{seas}(t)$	seasonal component of variability, comprised of annual and semiannual harmonics plus a constant offset, °C or mg Chl m^{-3}
$z(t)$	realization of the stochastic process Z(t), unspecified units
α_0	constant offset of harmonic fit, °C or mg Chl m^{-3}
α_1	amplitude of annual harmonic, °C or mg Chl m^{-3}
α_2	amplitude of semiannual harmonic, °C or mg Chl m^{-3}
$\gamma(h)$	semivariance as a function of time lag, unspecified units
$\hat{\gamma}(h)$	empirical semivariance as a function of time lag, calculated from the residual time series $Z_{res}(t)$, $(°C)^2$ or $(\text{mg Chl } m^{-3})^2$
$\hat{\gamma}_I(h)$	empirical presence / absence indicator semivariance as a function of time lag, calculated from the residual time series $Z_{res}(t)$, dimensionless
$\tilde{\gamma}(h)$	approximate expansion of the empirical semivariogram $\hat{\gamma}(h)$ based on $K' \leq K$ functions $f_k(h)$, unspecified units
ζ_1	phase of annual harmonic, radians
ζ_2	phase of semiannual harmonic, radians
$\mu(t_i)$	mean of random variable $Z(t_i)$, unspecified units
σ^2	overall variance or C(0), $(°C)^2$ or $(\text{mg Chl } m^{-3})^2$ where explicitly referred to as a model parameter, units are otherwise unspecified

Chapter 1

INTRODUCTION

The west coast of North America from Vancouver Island to the tip of Baja California lies inshore of the California Current System (CCS), an eastern boundary current system where coastal upwelling driven by persistent equatorward winds fuels heightened primary production and the growth of phytoplankton that serve as the foundation of large commercial fisheries [Hutchings et al., 1995; Pauly and Christensen, 1995]. Physical and biological processes within the CCS are highly variable over a wide range of scales [recently reviewed by Hickey, 1998; Hill et al., 1998; Hutchings et al., 1995; Smith, 1995]. Seasonal changes in large-scale wind systems introduce strong latitudinally dependent seasonal cycles of physical forcing and biological response. Set against seasonal patterns of variation are recurrent and particularly intense patterns of mesoscale variability (acting over space scales of tens to several hundred kilometers and time scales of days to several months). Wind forcing is characteristically pulsed over periods of days to weeks even at locations of sustained upwelling. Persistent winds blowing adjacent to the coastline cause the seasonally recurrent formation of an energetic system of jets and eddies whose interactions further contribute to a highly variable pelagic environment. These scales of physical variability closely match those of the life cycles of the dominant plankton of the region, leading to potentially strong coupling between physical and biological processes [Hutchings et al., 1995]. Closely coupled physical and biological variability implies potential ecological sensitivity to climate

change and basin-scale atmospheric or oceanic processes acting over interannual time scales.

Multiyear time series of satellite-derived sea surface temperature and surface chlorophyll concentrations provide the sole basis for the quantitative description of patterns of physical and biological variability acting over seasonal and intraseasonal time scales at reasonably high spatial resolution across the entire CCS. Such a description has not yet been published. Numerous studies have provided quantitative analyses of mesoscale SST or ocean color imagery over the CCS. These however, used statistical techniques that restricted analysis to limited spatial or temporal windows of cloud-free coverage [e.g. Abbott and Barksdale, 1991; Denman and Abbott, 1994; Kelly, 1985; Lagerloef, 1992; Michaelsen et al., 1988; Smith et al., 1988]. Studies that have used multiyear time series to quantify the magnitude and timing of seasonal fluctuations have generally done so at the expense of either spatial resolution or spatial coverage [e.g. Espinosa-Carreon et al., 2004; Hill et al., 1998; Michaelsen et al., 1988; Strub et al., 1990; Thomas et al., 1994; Thomas et al., 2001]. Here we quantify and compare patterns of variability acting over seasonal, interannual and dominant intraseasonal time scales using more than 5 years of daily SST and chlorophyll data assembled over an 18 km grid. By adopting relatively simple but robust statistical tools, we are able to extend our analyses over the entire region (Figure 1.1).

A brief review of physical and biological processes within the CCS is provided in Chapter 2, followed by detailed descriptions of data and methods in Chapters 3 and 4. The magnitude and timing of seasonal cycles, estimated by fitting time series to annual and semiannual harmonics, are presented and discussed in Chapter 5. Chapter 6 provides

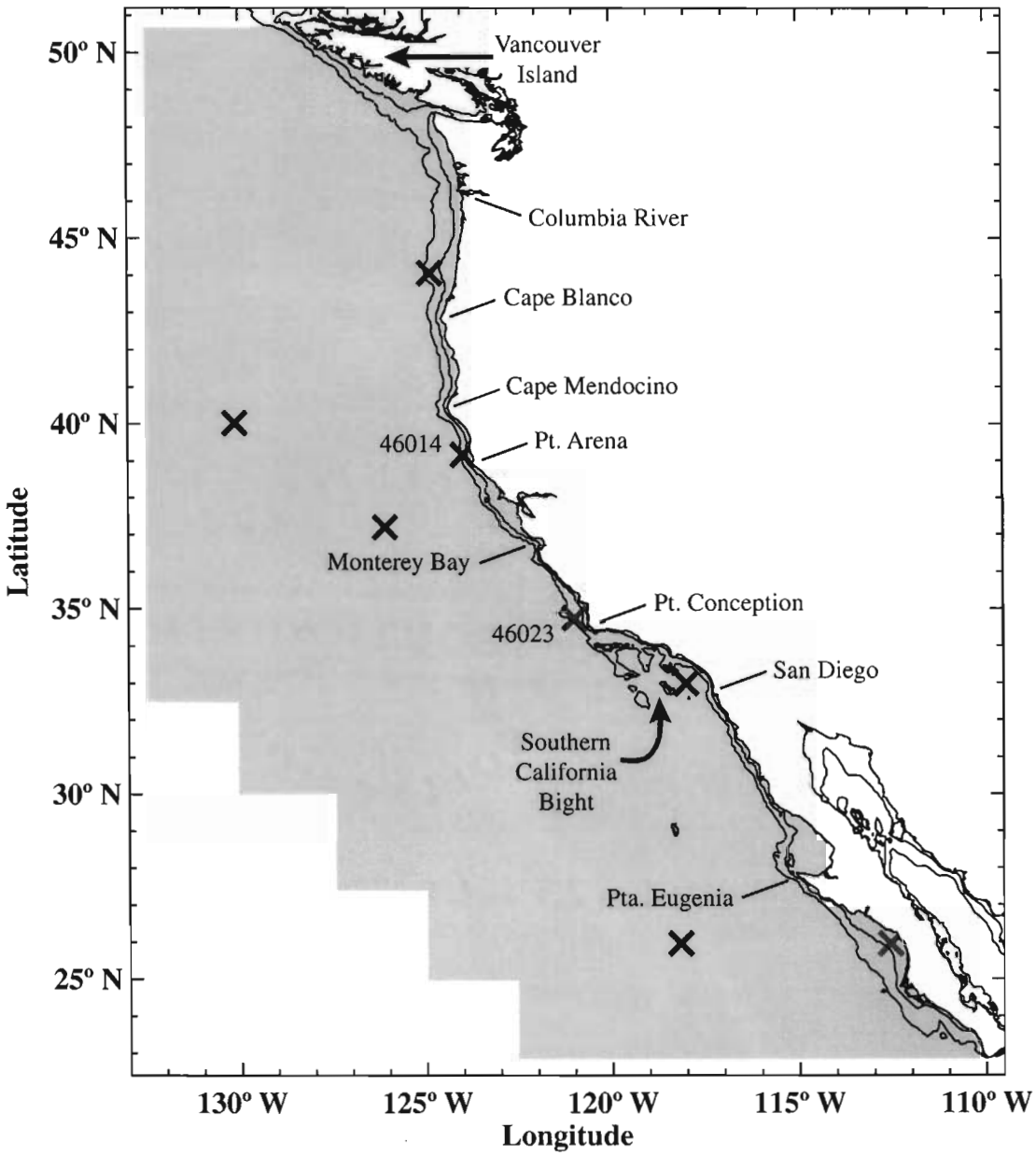

Figure 1.1 - *Study Region*
Map of the California Current study region, showing the area of interest (shaded) and locations of time series data discussed in detail within the text (X), including NDBC buoy stations 46014 and 46023. Also included are 100 and 500 m isobaths.

a description of the magnitude of interannual variability estimated by filtering non-seasonal residual series. Dominant patterns of intraseasonal variability were determined using geostatistical semivariograms or structure functions. Semivariograms have been used in the past as precursors to formal hypothesis testing [Thomas and Emery, 1988] or spatial prediction [Denman and Freeland, 1985]. They have also been effectively employed as a means of describing aspects of the spatial and temporal variability of satellite-derived SST and ocean color data [Deschamps et al., 1981; Doney et al., 2003; Fuentes et al., 2001; Wald, 1989; Yoder et al., 1987; Yoder et al., 2001]. The dominant scales of intraseasonal variability and the variance contributed by those scales are quantified and discussed in Chapter 7. Chapter 8 is a brief summary.

Chapter 2

BACKGROUND

The California Current (CC) carries relatively cool, fresh and enriched subarctic water southward as the eastern arm of the North Pacific subtropical gyre [Lynn and Simpson, 1987]. Warm, salty and nutrient-rich equatorial subsurface water enters the region from the south through the California Undercurrent, a narrow poleward flow found at mid-depth along the continental slope [Durazo and Baumgartner, 2002; Lynn and Simpson, 1987]. Persistent equatorward winds drive the offshore Ekman transport of the surface layer and the compensatory coastal upwelling of deeper waters. Upwelling-favorable winds tend to be strongest several hundred kilometers offshore, imparting substantial cyclonic wind stress curl seaward of the continental margin and providing an additional means of upward transport through Ekman suction [Bakun and Nelson, 1991; Pickett and Paduan, 2003]. Isopycnals shoal toward the eastern edge of the subtropical gyre so that water upwelled through either mechanism typically originates from below the nutricline, providing for the widespread enrichment of surface waters adjacent to the coastline.

Upwelling winds throughout the CCS are driven by anticyclonic circulation around the North Pacific subtropical high-pressure system. The North Pacific high attains its most northerly position and greatest strength in late spring and summer, coincident with the strengthening and expansion of a thermal low over the southwest U.S. and Mexico [Nelson and Husby, 1983; Strub and James, 1988]. Summer winds are driven by the pressure gradient between these two systems and are generally equatorward

and upwelling-favorable along the entire coastline [Dorman and Winant, 1995; Halliwell and Allen, 1987]. During mid- to late fall, high pressure weakens and retreats to the south ahead of an expanding and deepening Aleutian low [Strub and James, 1988]. Winter cyclones swing southward from the low-pressure center over the Gulf of Alaska and force a poleward, downwelling-favorable monthly mean wind stress along northern California and the Pacific Northwest. Upwelling-favorable winds persist along central California and the Baja Peninsula, although their strength is diminished [Dorman and Winant, 1995; Halliwell and Allen, 1987]. Along southern California, an abrupt eastward bend in the coastline between Point Conception (34.4° N) and San Diego (32.8° N) forms the Southern California Bight (SCB) (Figure 1.1), an area sheltered year-round from the stronger wind forcing found to the north and south [Dorman and Winant, 1995; Winant and Dorman, 1997].

The annual cycle accounts for no more than about half of the total variance of alongshore winds along the U.S. west coast. Much of the remaining variance is comprised of fluctuations with periods of days to weeks whose origins and statistical properties are themselves seasonally variable [Dorman and Winant, 1995]. Winter winds are dominated by events of 2-4 days duration driven by propagating synoptic-scale pressure systems [Dorman et al., 1995]. With the springtime expansion and strengthening of the North Pacific high, the paths of propagating storm systems are generally diverted to the Pacific Northwest, where summer winds remain highly variable [Beardsley et al., 1987; Dorman and Winant, 1995; Nelson and Husby, 1983]. Farther to the south, divergent circulation along the eastern flank of the North Pacific high causes large-scale subsidence and promotes the formation of a strong low-level inversion

wherein warm, dry and stable upper air overlies the cool, moist and turbulent marine boundary layer [Beardsley et al., 1987; Dorman and Winant, 1995]. The inversion base intersects the coastal mountains of northern and central California at low altitudes so that equatorward surface winds are channeled along the coastline, forcing strong and sustained upwelling [Beardsley et al., 1987; Dorman and Winant, 1995]. Equatorward winds within the marine layer accelerate as they round major headlands, further enhancing Ekman transport and suction within local upwelling centers [Edwards et al., 2002; Pickett and Paduan, 2003; Samelson et al., 2002]. Variations in synoptic pressure distributions and propagating coastally trapped disturbances cause considerable variation in the strength of upwelling, even at such locations [Halliwell and Allen, 1987; Beardsley et al., 1987; Dorman, 1987]. Fluctuating winds force pulsed upwelling and a correspondingly pulsed pattern of biological production [Hutchings et al., 1995].

The spring transition from poleward or more variable winds to stronger or more persistent equatorward winds forces a dramatic oceanic response, typically most pronounced along Oregon and northern California where climatological winds reverse seasonally [Strub and James, 1987; Strub and James, 1988]. Coastal sea levels drop as cool, saline and dense water is upwelled over the shelf and upper slope. Isopycnals curve upward toward the coast resulting in strong cross-shelf density gradients and the outcropping of a coastal upwelling front [Huyer et al., 1979; Strub et al., 1987]. Surface waters accelerate equatorward within a narrow, surface-intensified geostrophic jet [Smith, 1995; Winant et al., 1987]. The upwelling front and jet remain over the central Oregon shelf and slope throughout the ensuing upwelling season [Huyer et al., 1979; Strub et al., 1987]. They are however, quickly displaced offshore of the shelves of

northern California leaving behind a weakly stratified water column subject to frequent current reversals during periods of weak or poleward winds [Strub et al., 1987; Winant et al., 1987]. The northernmost point of jet separation is Cape Blanco, Oregon (42.8° N) (Figure 1.1), where topographic steering and a local orographic intensification of equatorward winds force its deflection into deeper waters [Barth et al., 2000; Samelson et al., 2002].

Where displaced from the shelf, the upwelling jet quickly migrates seaward of the continental margin under sustained wind forcing as the high-velocity core of the CC [Lynn et al., 2003; Strub and James, 2000]. Various instability processes quickly lead to the growth of meanders that, in time, develop into cyclonic and anticyclonic eddies to either side of the current core [Strub and James, 2000; Strub et al., 1991]. Cool and productive water is advected seaward within narrow upwelling filaments lying along the inshore edges of the offshore-directed legs of prominent meanders as they intensify and gradually extend offshore [Strub et al., 1991]. Vigorous eddy activity promotes rapid exchange between shelf waters and the open ocean and contributes to the expansion of productive waters several hundred kilometers seaward of the California coastline [Strub and James, 2000; Strub et al., 1991]. By late summer, equatorward winds weaken, coastal sea levels rise and an inshore poleward countercurrent develops along southern and central California [Strub and James, 2000]. Poleward coastal currents strengthen and extend northward, displacing the upwelling jet from the shelves of the Pacific Northwest [Batteen, 1997; Strub and James, 2000]. The jet and eddy system migrates westward through the fall and winter at speeds consistent with Rossby wave dynamics, gradually decaying along the way [Kelly, 1998; Strub and James, 2000]. This cycle of mesoscale

circulation is renewed at the coastline during the following spring with the intensification of equatorward winds and the formation of another upwelling front and jet [Lynn et al., 2003; Strub and James, 2000].

The CC core serves as a porous boundary between oceanic and coastal upwelling ecosystems [Strub et al., 1991]. The strongly stratified oceanic waters to the west are dominated by small phytoplankton whose growth is fueled by regenerated nutrients and culled by protozoan grazers. The lack of any major source of allochthonous nutrients allows for a steady balance between growth, grazing and nutrient remineralization [Landry et al., 1997]. Upwelling inshore of the CC core, however, introduces large quantities of nutrients into the euphotic zone during episodic enrichment events. As cool and nutrient-rich waters are entrained within local surface currents or advected seaward with the Ekman drift, surface heating and lateral mixing with warmer waters gradually stabilize the upper water column. A simultaneous release from nutrient and light limitation follows, allowing for the rapid growth of large-celled phytoplankton. Phytoplankton growth largely escapes consumption by virtue of the characteristically slow response of metazoan grazer populations in terms of juvenile growth and maturation. Nutrients are exhausted within days, leading to bloom senescence and the sedimentation of largely intact cells [Hutchings et al., 1995]. Upwelling communities inshore of the CC core therefore display a fundamental mismatch between time scales of production and consumption. Moreover, the variable winds and energetic mesoscale circulation characteristic of the region likely contribute to a generally poor coupling between producers and consumers in space and time [Hutchings, 1992].

Whereas a highly variable and stochastic environment favors the loss of production to the sediments, regular patterns of environmental variation promote the transfer of materials and energy between trophic levels [Legendre and Le Févre, 1992]. The dominant fisheries of the CCS are sustained by a short food chain in which large-celled phytoplankton are consumed by crustacean zooplankton which provide for the ample growth of planktivorous fish. The limited motility of zooplankton and larval fish imply a heavy dependence of these populations upon circulation structures that promote the recirculation or retention of individuals near nutrient-rich and productive locales while limiting the advective loss of individuals to the open ocean [Hutchings et al., 1995]. The entrainment and retention of biota within eddies regularly generated through instabilities of the CC core likely promotes trophic coupling and the recruitment of pelagic fish [e.g. Logerwell et al., 2001]. Moreover, interactions between coastal topography or shelf/slope morphology and local currents and winds lead to seasonally recurrent and stable flow features. Numerical and laboratory models suggest the formation of standing waves manifest as fixed meanders and stationary eddies [Batteen, 1997; Marchesiello et al., 2003; Narimousa and Maxworthy, 1987; 1989] and numerous observational studies have confirmed the seasonal recurrence of such features [e.g. Lagerloef, 1992; Simpson et al., 1986; Strub and James, 2000; Strub et al., 1991]. Stable patterns of along-shelf and cross-shelf flow at the surface and at depth may provide dependable avenues of dispersal for local populations and may promote the recirculation of biota near the productive coastal zone.

The fate of biological production fueled by upwelled nutrients, whether channeled into exploitable populations or exported to the sediments, is clearly dependent upon

patterns of environmental variability that are in turn sensitive to basin-scale atmospheric and oceanic processes. Changes in large-scale wind systems and currents over interannual and decadal scales likely modulate the timing, intensity and duration of upwelling and related mesoscale jet and eddy activity. We could expect different levels of response to interannual variability between areas of the CCS that tend to display different patterns of biophysical coupling or different levels of sensitivity to basin-scale atmospheric or oceanic forcing. Furthermore, recurrent and topographically locked flow features suggest the potential for site-specific mediation of large-scale physical forcing and biological response. Changing patterns of mesoscale variability have been implicated as potential sources of year-to-year variations in recruitment for a variety of species [Botsford, 2001; Logerwell et al., 2001; Parrish et al., 1981]. An improved understanding of year-to-year changes in ecosystem function should follow from an improved and integrated understanding of physical forcing and biological response over a wide range of scales.

Chapter 3

DATA

The SeaWiFS instrument provides global coverages of upwelled radiance within eight visible and near infrared spectral bands [Hooker and Esaias, 1993]. Chlorophyll concentrations are derived from empirical bio-optical algorithms relating ratios of the radiances of different visible bands to *in situ* data [O'Reilly et al., 1998; O'Reilly et al., 2000]. SeaWiFS data are provided by the NASA Goddard Space Flight Center Distributed Active Archive Center (GSFC DAAC) at several processing levels and at several spatial and temporal resolutions [Hooker and Esaias, 1993]. Level 1 data include raw radiance values with appended telemetry, navigation, and calibration data. Level 2 data are generated from Level 1 data following sensor calibration, atmospheric correction and application of bio-optical algorithms. For this study, we use Level 3 Standard Mapped Images of chlorophyll concentrations derived from the projection of binned Level 2 data onto an equal-angle grid with a nominal resolution of 9 km [Hooker and Esaias, 1993].

Daily imagery from the fourth SeaWiFS reprocessing spanning the period September 4, 1997 through July 5, 2003 were obtained from the GSFC DAAC and subset over the CCS. Time series of chlorophyll concentrations were constructed throughout the study region from the geometric means of pixels lying within non-overlapping 18 km x 18 km boxes. Spatial averaging of the daily 9 km data was employed primarily as a means of reducing the size of the data set used in subsequent calculations. Spatial averages were computed as geometric means and time series were transformed by the

natural log following the assumption that oceanic bio-optical data are distributed approximately log-normally [Campbell, 1995].

Time series of daily sea surface temperature were assembled from the NOAA/NASA AVHRR Oceans Pathfinder equal-angle, 9 km best-SST data product distributed through the NASA Physical Oceanography Distributed Active Archive Center at the Jet Propulsion Laboratory, California Institute of Technology. The AVHRR instrument is carried aboard each of the NOAA Polar-Orbiting Operational Environmental Satellites and collects data over five visible and infrared spectral bands [Kidwell, 1998]. The Pathfinder algorithm uses a nonlinear, empirical model relating 4 km infrared radiance data to SST. SST data values are flagged according to a series of multichannel and threshold tests designed to assess the likelihood that any given SST value was compromised by data processing errors, cloud contamination, or various viewing conditions related to the orientation of the satellite relative to the sun and earth. The results of all individual tests are pooled to define eight overall levels of quality for SST estimates. Quality levels are not associated with specific magnitudes of error in the SST estimates themselves, but rather serve as indications of the likelihood that certain estimates are erroneous. Binned SST values are subsequently computed over a 9 km grid using only the highest quality estimates available for each bin [Vazquez et al., 1998].

For comparison with the SeaWiFS data described above, we assembled concurrent time series from best-SST data in which only the four highest quality levels were retained [Vazquez et al., 1998]. These data were derived from the Pathfinder Version 4.1 (Sept. 4, 1997 - Dec. 31, 1999) and Interim Version 4.1 (Jan. 1, 2000 – July 5, 2003) algorithms using SST estimates collected from ascending passes only. Time

series were constructed from the arithmetic means of pixels lying within non-overlapping 18 km x 18 km boxes.

Cloud cover and satellite orbital geometry limited the number of observations available to considerably fewer than the 2131 days spanned by the chlorophyll and SST time series. Figure 3.1 shows the number of SST and chlorophyll observations available at any given location as a fraction of the total duration of our daily time series. At any particular grid location, SST estimates are available for about 15-55% of the total number of days. Fewer SST retrievals are available for many locations immediately adjacent to the coastline owing to known deficiencies in the Pathfinder SST landmask (NOAA/NASA AVHRR Oceans Pathfinder home page, http://podaac.jpl.nasa.gov/sst/). Overall patterns of chlorophyll data availability are similar to those of SST, although reduced by 5-10% in most areas.

For the most part, Figure 3.1 reflects predominant patterns of cloud cover observed throughout the data record [Nelson and Husby, 1983]. Cloud formation throughout much of the California Current region is related to the depth of the marine layer and height of the inversion base via the lifting condensation level (LCL), the altitude at which a parcel of air becomes saturated as it is lifted adiabatically from sea level [Beardsley et al., 1987]. Well offshore, the inversion base is high so that rising air within the marine layer can pass through the LCL and clouds can form. Closer to shore, the marine layer thins and the separation between the inversion base and the LCL is reduced. Cloud formation is suppressed where the elevation of the inversion base drops below the LCL. Large-scale patterns of upper level subsidence along the eastern flank of the North Pacific high therefore imply lower levels of mean cloud cover closer to shore, a

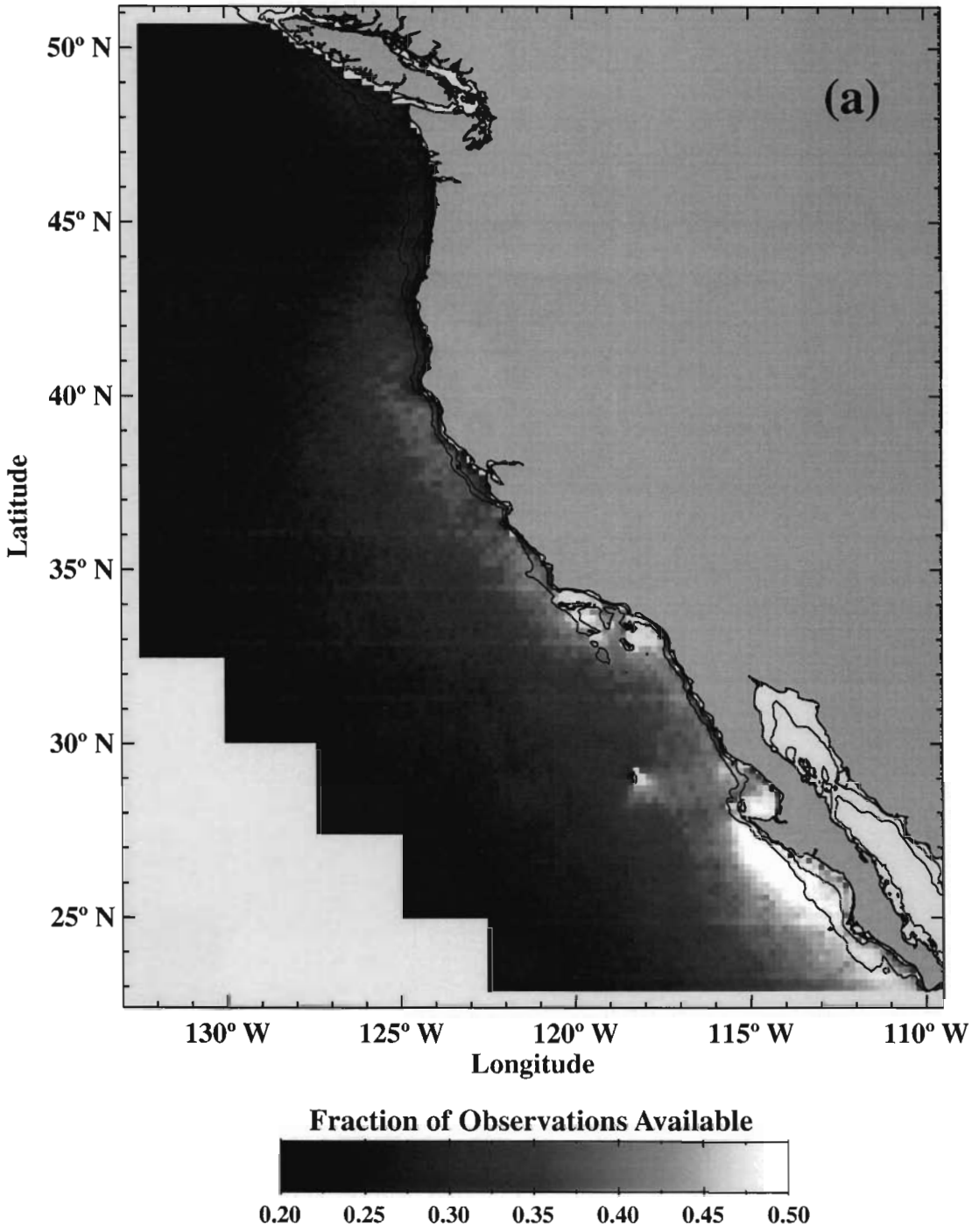

Figure 3.1 - *Time Series Data Availability*
(a) Number of daily observations available as a fraction of the total duration of the 2131-day Pathfinder SST time series.

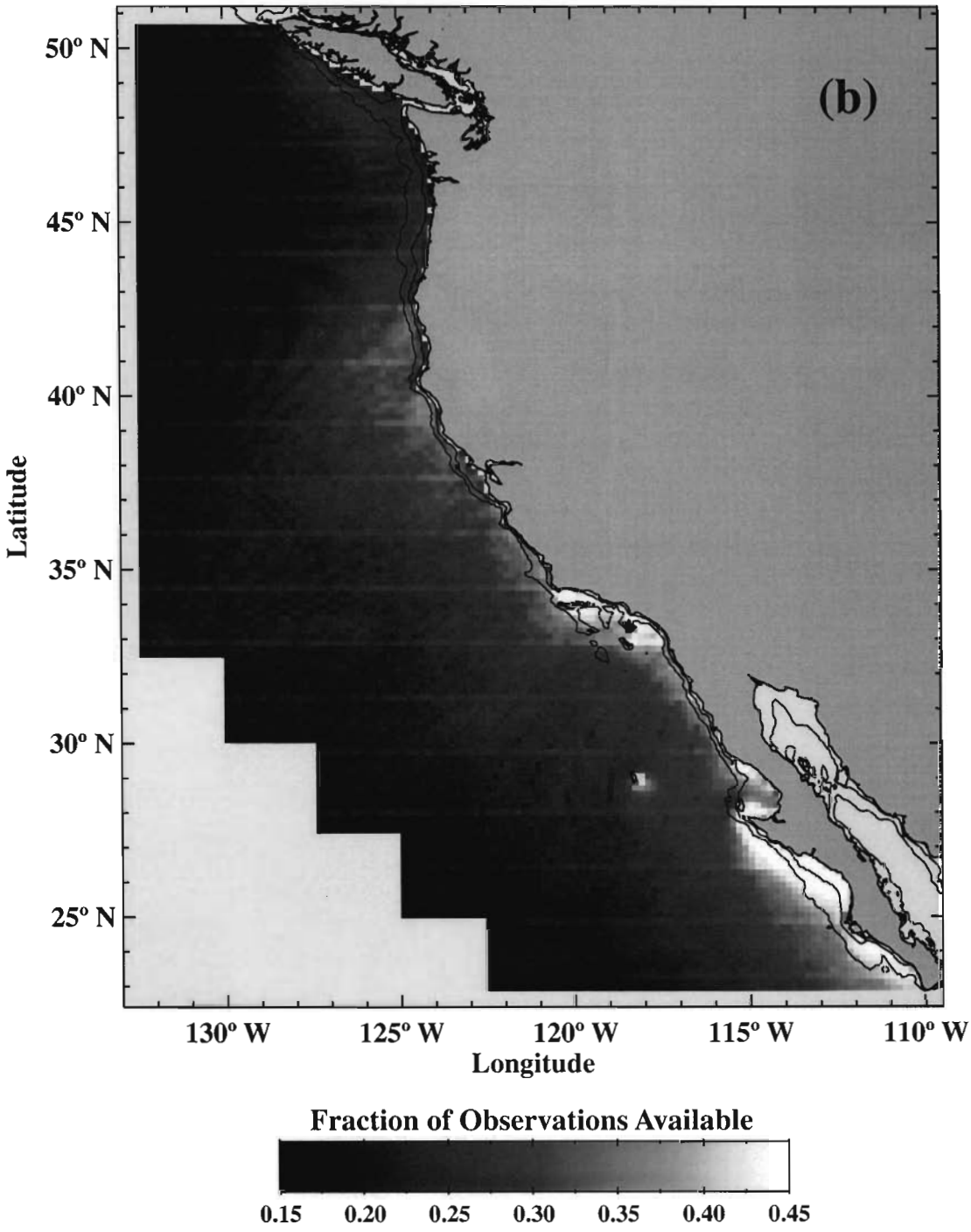

Figure 3.1 - *Continued*
(b) Number of daily observations available as a fraction of the total duration of the 2131-day SeaWiFS chlorophyll time series.

trend evident in Figure 3.1. Cloud cover is most strongly suppressed along the southern Baja coastline, where the persistent offshore flow of warm and dry continental air from the Sonoran Desert contributes to clear skies [Yashayaev and Zveryaev, 2001; Nelson and Husby, 1983]. Mean coastal cloud cover generally increases to the north due to a decrease in the overall influence of the North Pacific high and an increase in exposure to propagating synoptic-scale storm systems.

Chapter 4

METHODS

4.1 Statistical Approach

Because semivariograms have not been widely used in the ocean sciences, we include a relatively complete description of their theory and application here. A more thorough description can be found in any number of geostatistics texts [e.g. Goovaerts, 1997; Journel and Huijbregts, 1978; Webster and Oliver, 2001].

The methods of geostatistics provide a stochastic framework for investigating the behavior of spatially or temporally distributed data, predicting values at times or locations of missing observations, and quantifying the uncertainty associated with those predictions. By adopting a stochastic approach to the description of temporal variability, we consider a time series Z(t) at a given location as a random function comprised of a set of random variables $Z(t_i)$ corresponding to the N observations available at that location. Each random variable is characterized by some probability distribution from which the actual observed value of Z at time t_i, denoted $z(t_i)$, is drawn at random. The observed value $z(t_i)$ is one of an ensemble of possible realizations of Z at time t_i. The specification of a statistical model for the stochastic process Z(t) amounts to the specification of the probability distributions of the random variables comprising the process, or more specifically the joint probability distributions of all possible subsets of those variables.

In practice, analysis is usually simplified by considering probability distributions involving only one or two observations at a time and by considering only the first and second moments of those distributions. Variability is thereby decomposed into two

components. The first relates to variations of the mean through time and is generally described by a global or large-scale trend. The second relates to the temporal dependence of stochastic fluctuations about the mean and is described by the correlation structure of deviations from the trend. This division between first and second order structure serves as the basis for our descriptions of chlorophyll and SST variability. We define the large-scale trend of each time series as the sum of a regular seasonal cycle and an irregular component of interannual variability. Second order variation is assumed to arise from intraseasonal fluctuations. We focus on data description, although our methods may be readily adapted to provide an explicit statistical model useful for prediction or optimal averaging [e.g. Chelton and Schlax, 1991; Walker and Wilkin, 1998].

Seasonal cycles were modeled as the sum of annual and semiannual harmonics plus a constant offset or annual mean:

$$Z_{seas}(t) = \alpha_0 + \alpha_1 \cos(2\pi f_1 t + \zeta_1) + \alpha_2 \cos(2\pi f_2 t + \zeta_2) \quad (1)$$

where f_1 and f_2 are the annual and semiannual frequencies (f_1 = 1 cycle yr^{-1} and $f_2 = 2f_1$) and α_0, α_1, α_2, ζ_1, and ζ_2 are the offset, amplitudes and phases estimated through ordinary least squares regression. Interannual variation was estimated using a Gaussian kernel with a 365-day full width at half maximum applied to the time series following the removal of seasonal variability. The variance of the smoothed time series resulting from this step provides a measure of the magnitude of variability acting over interannual time scales at each grid location [e.g. Walker and Wilkin, 1998]. Intraseasonal variance and dominant intraseasonal time scales were determined from the correlation structure of residual time series following the removal of seasonal and interannual variability.

The covariance between any two random variables $Z_{res}(t_i)$ and $Z_{res}(t_j)$ constitutes a measure of the similarity between the two and is defined as

$$C(Z_{res}(t_i), Z_{res}(t_j)) = E\{[Z_{res}(t_i) - \mu(t_i)] \cdot [Z_{res}(t_j) - \mu(t_j)]\} \quad (2)$$

where $\mu(t_i)$ and $\mu(t_j)$ are the means of $Z_{res}(t_i)$ and $Z_{res}(t_j)$, and where $E(\cdot)$ denotes the expectation function. With only a single realization of the process available for observation, we have no direct means of estimating $C(t_i,t_j)$. Provided the data satisfy certain assumptions of statistical stationarity, however, values observed at different times can be treated as different realizations of the same random variable. The N time-distributed observations which comprise the data series can thereafter be used as a sample from which the probability distribution of $Z_{res}(t)$ could be inferred. Use of the covariance function requires the assumption of a constant mean and variance for all variables $Z_{res}(t_i)$ and a finite covariance that depends upon the time separation between observations only and not upon actual observation times. Thus $C(t_i,t_j)$ is constant for all times t_i and t_j separated by the same time lag $h = |t_i - t_j|$, or

$$C(Z_{res}(t), Z_{res}(t+h)) = C(h) \quad (3)$$

Taken together, these assumptions constitute second order or weak stationarity of the process $Z_{res}(t)$ and imply the complete absence of any remaining first order variation of the mean.

In practice, the delineation of first and second order variation is an arbitrary step imposed as a means of simplifying analyses. We use annual and semiannual harmonics as a partial description of trend because they provide a concise and useful description of seasonality. They cannot however, follow abrupt transitions between seasons and they cannot capture year-to-year changes in the timing or magnitude of the seasonal cycle. It

is therefore unlikely that all significant seasonal-scale variability will have been removed from the original time series, and the presence of any remaining seasonal-scale variability within the residuals will introduce modest departures from weak stationarity in which the mean appears to vary through time. Provided the mean of the residual series remains constant over shorter time lags, we can assume that

$$E[Z_{res}(t) - Z_{res}(t+h)] = 0 \tag{4}$$

for small h. If in addition we assume weak stationarity of the increments $[Z(t_i) - Z(t_j)]$, we can substitute the variance of the difference $[Z(t) - Z(t + h)]$ for the covariance to obtain an alternative measure of temporal dependence:

$$\gamma(h) = \frac{1}{2}\text{var}[Z_{res}(t) - Z_{res}(t+h)] \tag{5}$$

Equations (4) and (5) constitute intrinsic stationarity, a weaker form of stationarity in which only local homogeneity is required. The quantity $\gamma(h)$ for a given time lag h is referred to as semivariance and constitutes a measure of the average dissimilarity between data values separated by the lag h. As a function of time lag, $\gamma(h)$ is known as the semivariogram. Here we use the semivariogram as a means of describing intraseasonal variability because estimates of semivariance tend to be resistant to modest departures from weak stationarity deriving from the incomplete removal of trend.

For an autocorrelated and weakly stationary time series, the semivariogram is a mirror image of the covariance function about a line parallel to the lagged separation axis (time, in this case) (Figure 4.1a) and the two functions are related according to the expression

$$\gamma(h) = C(0) - C(h) \tag{6}$$

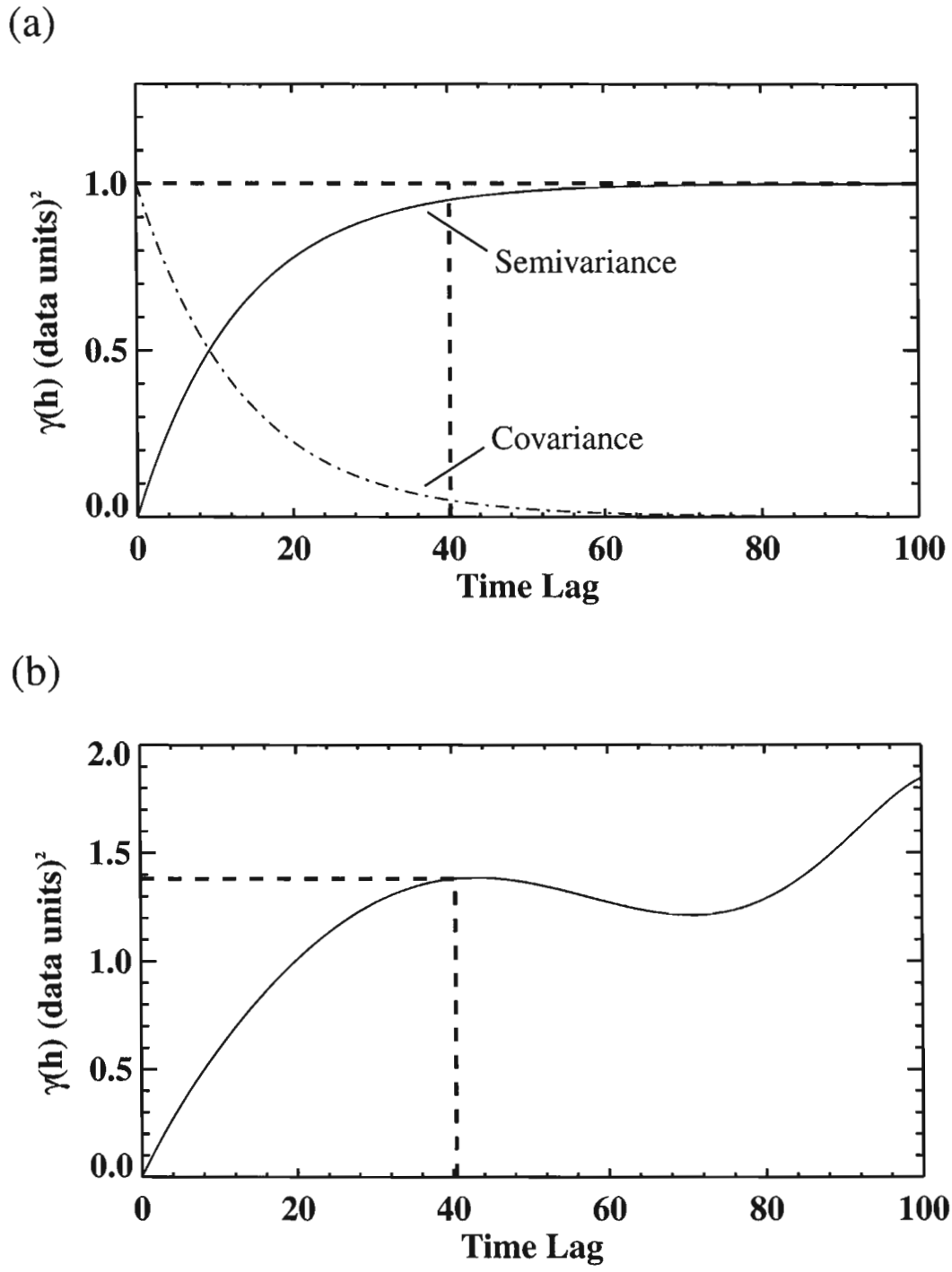

Figure 4.1 - *Idealized Semivariograms*
(a) Semivariogram and covariance function calculated from a weakly stationary time series. Vertical and horizontal dashed lines indicate range and sill, respectively. (b) Semivariogram illustrating the effect of regular repetition in the underlying time series. The vertical dashed line indicates the time lag corresponding to one-half of the dominant period. The horizontal dashed line indicates the magnitude of variability acting over the time scale of the dominant period.

where $C(0) = \sigma^2$, the overall variance of the process. When this is the case, the semivariogram climbs monotonically from small values at shorter lags to large values at longer lags, indicating an increase in average dissimilarity between data pairs with increasing separation times. The semivariogram will either attain or asymptotically approach an upper bound referred to as the sill, equal to the overall variance of the process. When the semivariogram attains or closely approaches the sill value at a given time lag, the semivariogram is said to have a range equal to that lag. Covariance drops to zero at the range so that observations separated by lag times greater than the range are no longer temporally correlated. The range therefore marks the outer limit of temporal dependence.

Regular repetition or periodicity within the time series will introduce a peak in semivariance at a time lag equal to one-half of the dominant period (Figure 4.1b). More generally, multiple scales of variability may lead to multiple, irregularly spaced peaks or sills. The time lag of a prominent peak corresponds to a dominant scale of variability and the value of peak semivariance equates to the magnitude of variability acting over that scale. Because significant correlation may persist at lags longer than those at the center of a local peak, a dominant scale in this case may not equate to the decorrelation scale of the process, and peak semivariance may or may not approximate the overall variance of the process. Nevertheless, we are generally interested in defining prominent peaks as a means of characterizing dominant time scales of variability. Finally, an unbounded increase in semivariance implies some degree of non-stationarity of the underlying process over the time lags considered. Although the covariance function may be ill defined under these conditions, the semivariogram will likely remain a valid descriptor of

temporal dependence provided the departure from stationarity is not so strong as to mask or distort evidence of temporal structure at shorter lags.

4.2 Application to SST and Chlorophyll Time Series

Here we illustrate the application of the statistical approach described above to image data series using a single location as an example. Figure 4.2a shows the time series of SST constructed from the 18 km sampling box located over outer slope waters about 75 km offshore of central Oregon (44.1° N, 124.8° W) (Figure 1.1). The trend line displayed in Figure 4.2a represents the combined contributions of the regular seasonal cycle and irregular interannual variations calculated in the manner described above. Annual and semiannual harmonics describe a mean seasonal cycle that accounts for 88% of the total temporal variance of SST. Although seasonal fluctuations at this location are clearly dominated by a strong annual cycle, the semiannual harmonic plays a significant role in accommodating an asymmetric seasonal cycle, prolonging the winter minimum at the expense of the summer maximum. We estimate the significance of fitted harmonic parameters using the nonparametric bootstrap technique described by Efron and Tibshirani [1998]. Michaelsen et al. [1988] also provide a concise description of this method, and we will not repeat that here. The amplitudes and phases of both annual and semiannual harmonics at this particular location are significant at better than the 90% level according to bootstrapped estimates of their standard errors.

Figure 4.3a displays the ln-transformed time series of SeaWiFS chlorophyll collected from the same location as the SST data described above. Seasonal variability is evident within this time series, although a large amount of variability acting over

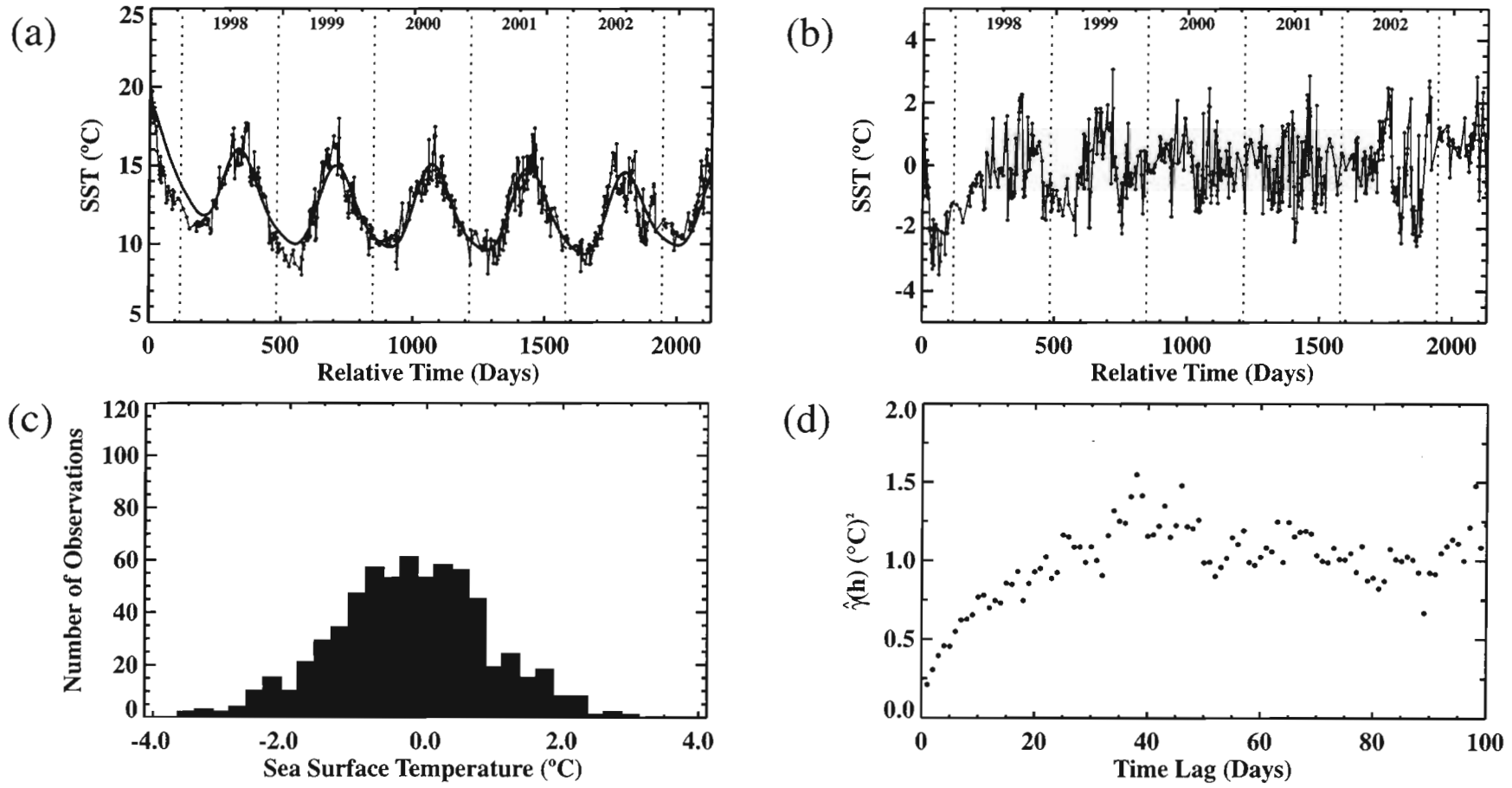

Figure 4.2 - *Example Application of Statistical Approach to SST Time Series*
(a) Time series of Pathfinder SST assembled from the 18 km sampling box located at 44.1° N, 124.8° W (location shown in Figure 1.1). The large-scale trend represents the combined contributions of annual and semiannual harmonics and an irregular component of interannual variation. (b) Residual time series calculated by subtracting the large-scale trend from the original time series shown in (a). (c) Histogram of the residual data shown in (b). (d) Empirical semivariogram estimated from the residual time series shown in (b).

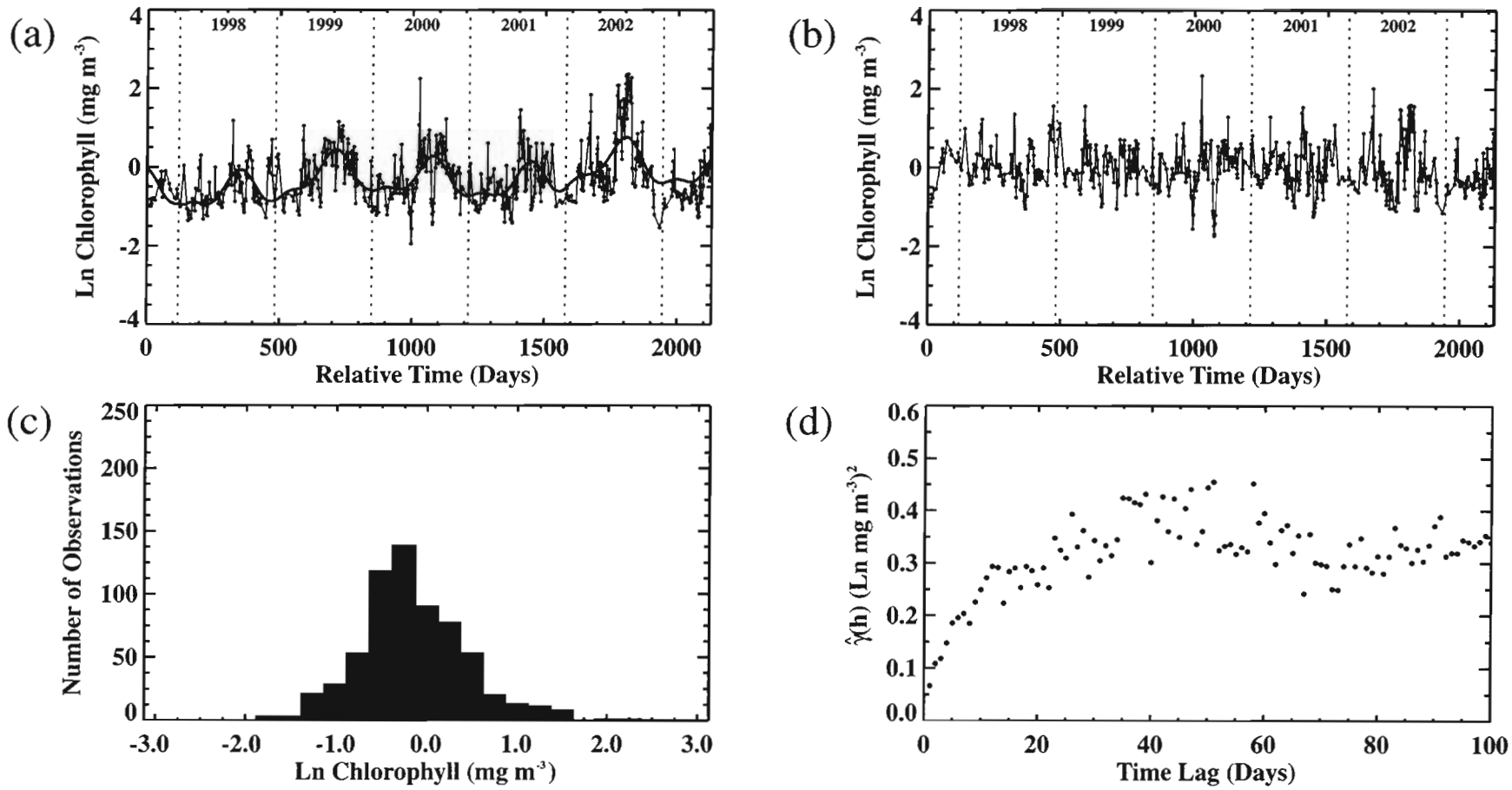

Figure 4.3 - *Example Application of Statistical Approach to Chlorophyll Time Series*
(a) Time series of ln-transformed SeaWiFS chlorophyll assembled from the 18 km sampling box located at 44.1° N, 124.8° W (location shown in Figure 1.1). The large-scale trend represents the combined contributions of annual and semiannual harmonics and an irregular component of interannual variation. (b) Residual time series calculated by subtracting the large-scale trend from the original time series shown in (a). (c) Histogram of the residual data shown in (b). (d) Empirical semivariogram estimated from the residual time series shown in (b).

intraseasonal and interannual time scales tends to obscure regular fluctuations. The semiannual harmonic plays a substantive role in describing a semiannual periodicity apparent in most years. The mean seasonal cycle at this location peaks in mid-August, decreases through late summer and fall to a minimum in late December, and then increases very slightly in mid-winter before climbing back to its mid-summer maximum. Annual and semiannual harmonics explain only 36% of the total variance of the ln-transformed series, although the amplitudes and phases of both annual and semiannual harmonics are significant at better than the 90% level.

Both time series exhibit considerable year-to-year variability in the magnitude and timing of seasonal extremes and in the rate at which temperatures and chlorophyll concentrations rise and fall between extremes. Figures 4.2b and 4.3b show residual time series of SST and chlorophyll obtained by subtracting the large-scale trend from each from the original time series. Considering time scales of several weeks to several months, SST residuals exhibit clear departures from stationarity where temperatures are consistently overestimated by the large-scale trend during late 1997 and early 1999. This observation illustrates the inability of annual and semiannual harmonics to model non-stationary seasonal-scale fluctuations and supports our use of the semivariogram as a robust measure of residual temporal dependence.

Figures 4.2c and 4.3c display histograms compiled from the residual series of SST and chlorophyll. At this particular location, SST residuals are very nearly normal. The distribution of chlorophyll residuals, however, is clearly skewed toward positive values and possesses somewhat thicker tails than those expected of a normal process. Chlorophyll residuals were moderately skewed at nearly all locations. Residual

distributions of both variables typically displayed thick tails. Chlorophyll residuals tended to deviate from normality more strongly than SST residuals, although deviations from normality could be deemed significant for both variables throughout most of the region (D'Agostino-Pearson K^2, $p < 0.01$) [D'Agostino, 1986].

Because empirical estimates of semivariance are generally sensitive to skewed distributions and extreme values, we used a robust estimator of semivariance proposed by Cressie and Hawkins [1980]:

$$\hat{\gamma}(h) = \frac{\frac{1}{2}\left(\frac{1}{n(h)} \sum_{n(h)} \left| z(t_i) - z(t_i + h) \right|^{\frac{1}{2}} \right)^4}{\left(0.457 + \frac{0.494}{n(h)} \right)} \tag{7}$$

where n(h) is the number of pairs of observations separated by the time lag h. Semivariance was estimated to a maximum time lag of 100 days, a scale below which most (of the residual) temporal structure of interest was observed to occur. The analytical derivation of confidence limits for estimates of semivariance is generally complicated by nonrandom sampling of the underlying process, correlations between estimates, and the use of the same data in multiple estimates [Webster and Oliver, 2001]. For practical applications, the assessment of what constitutes a statistically sufficient number of data pairs used to estimate semivariance at a given lag appears to be somewhat subjective. We considered an estimate of semivariance to be valid provided at least 30 data pairs were used in its calculation, a criterion suggested by Journel and Huijbregts [1978] and similarly employed by Doney et al. [2003] and Fuentes et al. [2000] for the estimation of spatial semivariograms from SeaWiFS data. Only valid estimates were included in subsequent analyses.

Figures 4.2d and 4.3d show empirical semivariograms computed from the residual time series of SST and chlorophyll. Empirical estimates of semivariance are subject to error arising primarily through incomplete sampling of the underlying process. In our case, sampling error introduced chiefly through intermittent cloud cover contributed considerable scatter to all semivariograms. Nevertheless, the SST and chlorophyll semivariograms shown here display clear trends toward peak values ~40-50 days. Because semivariance at lag zero must be zero, the semivariogram truly representative of SST and chlorophyll data series must increase continuously from the origin. In practice however, as lag time decreases toward zero, empirical estimates of semivariance typically approach a positive value of semivariance referred to as the nugget. The nugget arises from a combination of measurement error and unresolved variation acting over time scales shorter than the sampling interval. Both semivariograms displayed in Figures 4.2d and 4.3d indicate a significant nugget effect. The temporal distributions of the residual series of both variables are therefore comprised of a temporally correlated component of variability superimposed over an uncorrelated, random component whose contribution is given by the nugget.

In order to objectively discriminate coherent structural features from the more or less erratic behavior introduced by sampling fluctuations, an Empirical Orthogonal Function (EOF) analysis [Priesendorfer, 1988] was performed on each of the SST and chlorophyll semivariance data sets (Appendix A). EOF analysis partitions the total variance of a two-dimensional data set into a series of orthogonal structures or functions that maximize the amount of variance that can be explained by the fewest such structures. We used this technique to decompose each of our spatially distributed sets of chlorophyll

and SST semivariograms into a set of orthogonal functions (the EOFs) describing characteristic patterns of semivariance and a set of spatial amplitude functions describing the relative contribution of each EOF to the empirical semivariogram calculated at each grid location. The set of EOFs and corresponding spatial amplitude functions define a set of orthogonal statistical modes of variability that collectively partition the total structure of the semivariance data.

Consider a data set of M semivariograms, each comprised of 100 semivariance estimates and each calculated from data collected at a different location. EOF analysis seeks to express the semivariogram $\hat{\gamma}_m(h)$ calculated at some location x_m as the weighted sum of 100 orthogonal functions $e_k(h)$, for k=1, 2, …, 100, such that

$$\hat{\gamma}_m(h) = \sum_{k=1}^{100} a_k(x_m) e_k(h) \tag{8}$$

where $a_k(x)$ is the spatial amplitude function or principle component corresponding to the k^{th} orthogonal function. In this context, the semivariogram at location x_m is expressed as a linear combination of 100 functions $e_k(h)$, whose contributions are determined by 100 location-dependent amplitude functions $a_k(x)$. For each EOF, the amplitude function $a_k(x)$ constitutes a spatial map of coefficients which define the relative contribution of that EOF to the structure of the original semivariograms calculated at all locations.

EOFs provide the most efficient representation of the semivariance data in that for some fixed number of functions K' < 100, there is no approximate expansion

$$\tilde{\gamma}_m(h) = \sum_{k=1}^{K'} a_k(x_m) f_k(h) \tag{9}$$

that leads to a lower mean square error

$$\left\langle [\hat{\gamma}_m(h) - \tilde{\gamma}_m(h)]^2 \right\rangle \tag{10}$$

than that attained when $f_k = e_k$ [Davis, 1976]. A reconstruction of a given semivariogram based on the first few dominant EOF modes therefore retains only that variance structure which operates coherently across the time lags considered. In this manner, EOF analysis provides a means of filtering incoherent variability or noise from empirical semivariograms to isolate dominant structures of potential interest. The EOF of the first mode, the mode that accounts for the greatest amount of total structure of the semivariance data set, describes the semivariogram shape most representative of empirical semivariograms calculated throughout the region. We use the combined structure assigned to statistically significant higher modes as a means of describing coherent structural deviations from the first-mode semivariogram.

Prior to analysis, each empirical semivariogram was centered and then normalized by its standard deviation so that EOF modes were not biased by semivariograms computed from high-variance time series. Missing data at longer time lags proved to be a problem only for a small number of semivariograms computed from the most poorly sampled SST time series at locations immediately adjacent to the coastline. We exclude results from those locations. The statistical significance of each EOF mode was evaluated using the Monte Carlo technique described by Overland and Priesendorfer [1982]. Based on this approach, a given mode was assumed significant provided it explained a greater amount of overall semivariance structure than did 95% of the corresponding modes derived from the analyses of 100 random data sets of the same size.

Chapter 5

MEAN SEASONAL CYCLE

Here we describe seasonal cycles of SST and chlorophyll by presenting estimates of the amplitudes and phases of annual and semiannual harmonics. The magnitude and timing of seasonal maxima and minima result from the combined contributions of both harmonics. Because the relative timing of seasonal extremes between locations is often made ambiguous by strong semiannual fluctuations, phase estimates generally provide the clearest delineation of areas in which SST or chlorophyll concentrations vary in unison over seasonal scales, presumably in response to common dominant forcing mechanisms. We present offsets, amplitudes and phases only at those grid locations where estimates are significant at the 80% level as determined from bootstrapped standard errors. Throughout this chapter we refer to specific time series assembled at locations shown in Figure 1.1.

5.1 SST

Mean surface temperatures estimated from the offset of harmonic fits reflect broad patterns of summer surface circulation set against latitudinal gradients of surface heating which tend to dominate winter temperature distributions (Figure 5.1a). Isotherms south of ~47° N generally tend toward the southeast, consistent with the equatorward transport of cool subarctic water within the CC. Mean temperatures are further reduced along the U.S. west coast at mid-latitudes, where summer upwelling causes annual mean isotherms to parallel the coastline. Cool water recently upwelled near Point Conception

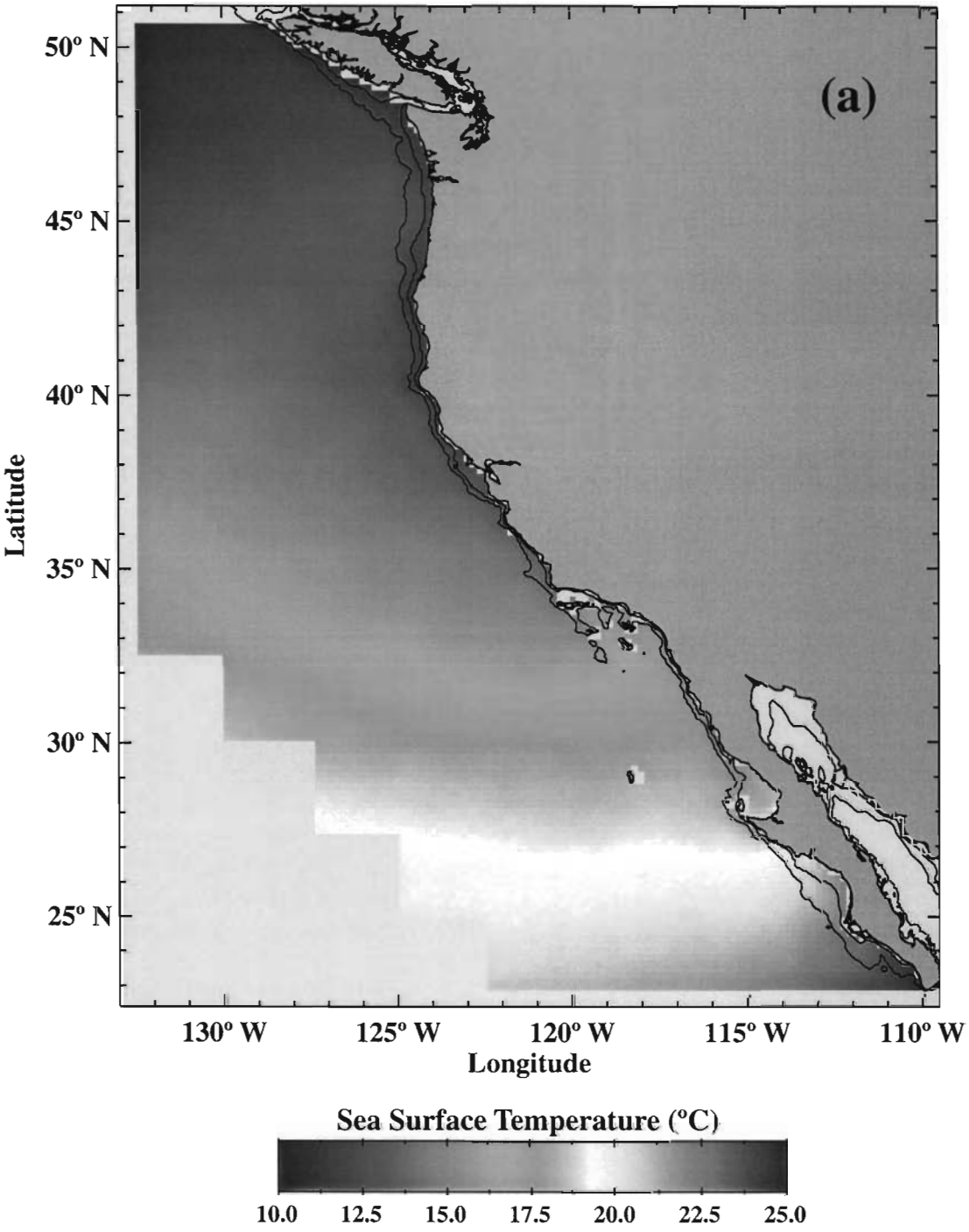

Figure 5.1 - *Mean Seasonal Cycle Fit to SST Time Series*
(a) Mean temperature estimated from the offset of the harmonic fit.

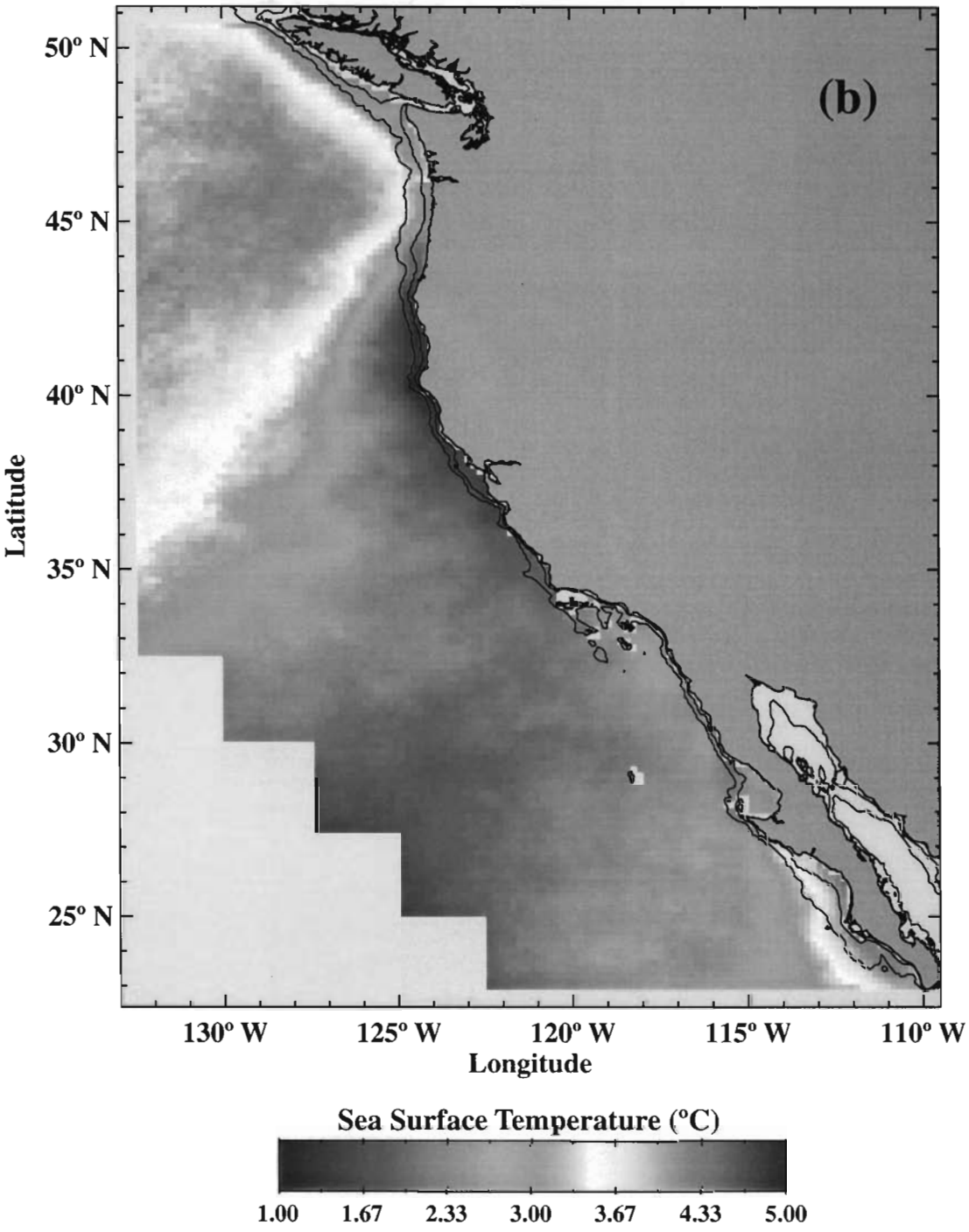

Figure 5.1 - *Continued*
(b) Amplitude of the annual harmonic.

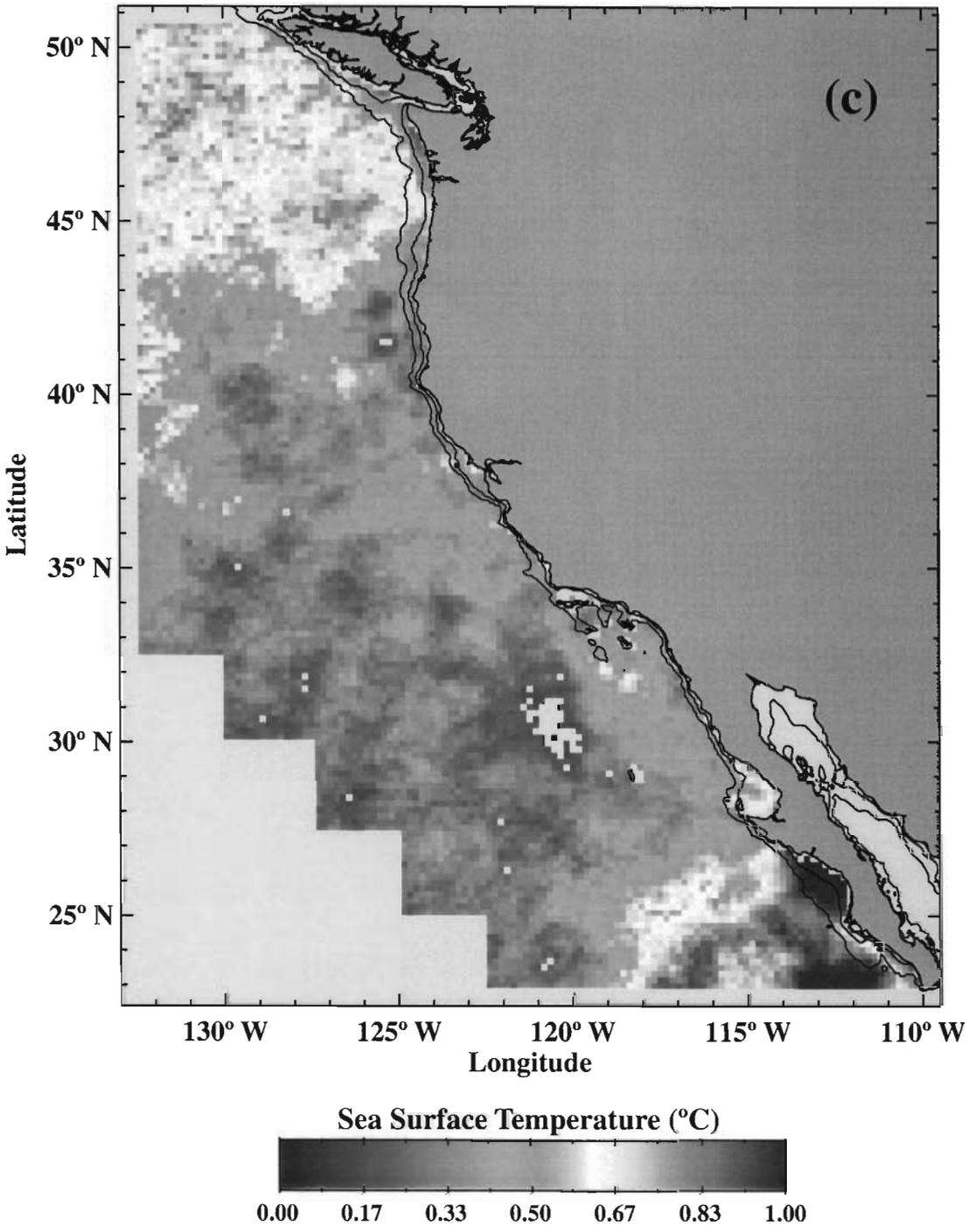

Figure 5.1 - *Continued*
(c) Amplitude of the semiannual harmonic.

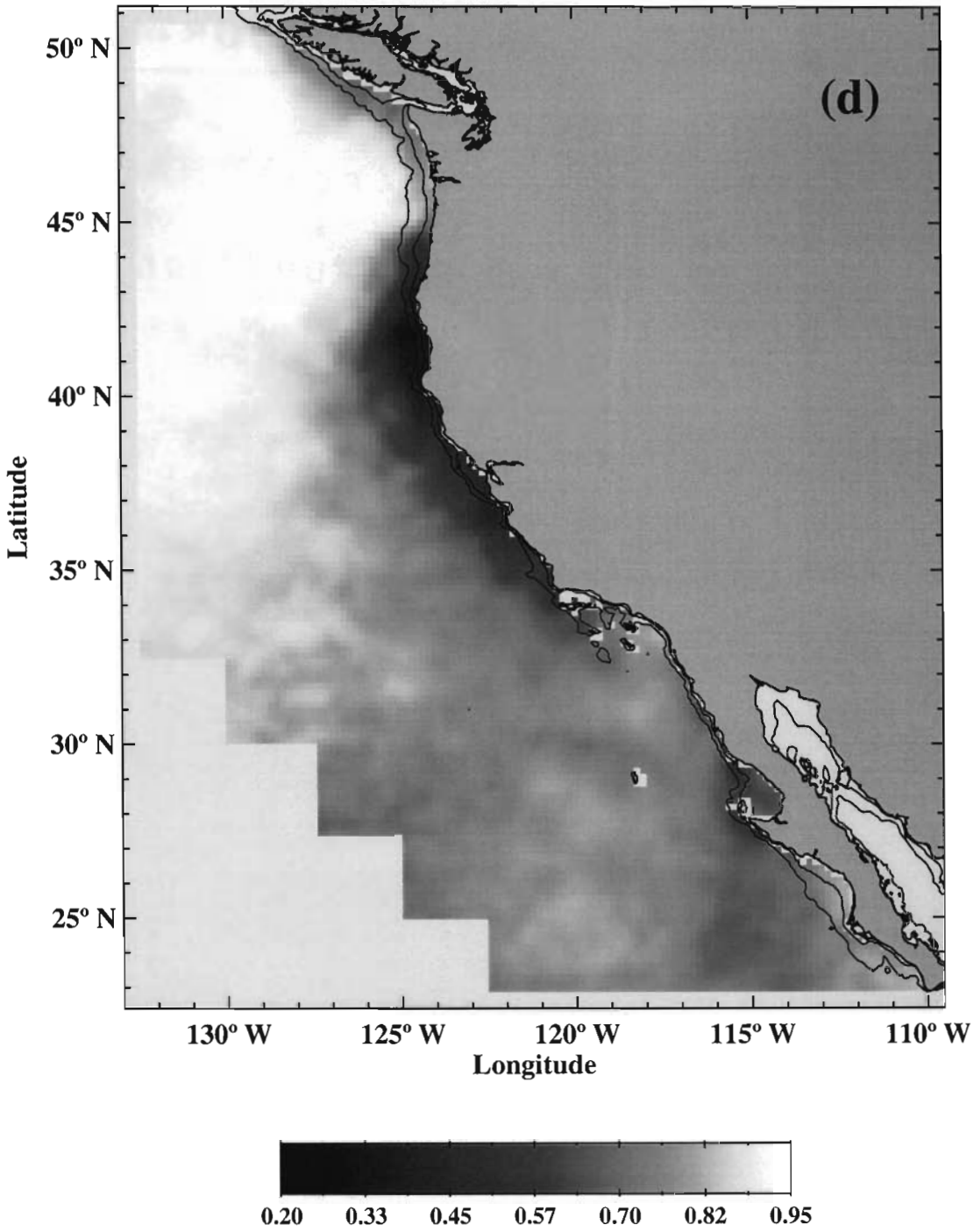

Figure 5.1 - *Continued*
(d) Fraction of total SST variance contributed by annual and semiannual harmonics. Total variance was approximated as the sum of variance contributed by the mean seasonal cycle, dominant intraseasonal variability and interannual variability. Data were smoothed with a 5 x 5 moving average.

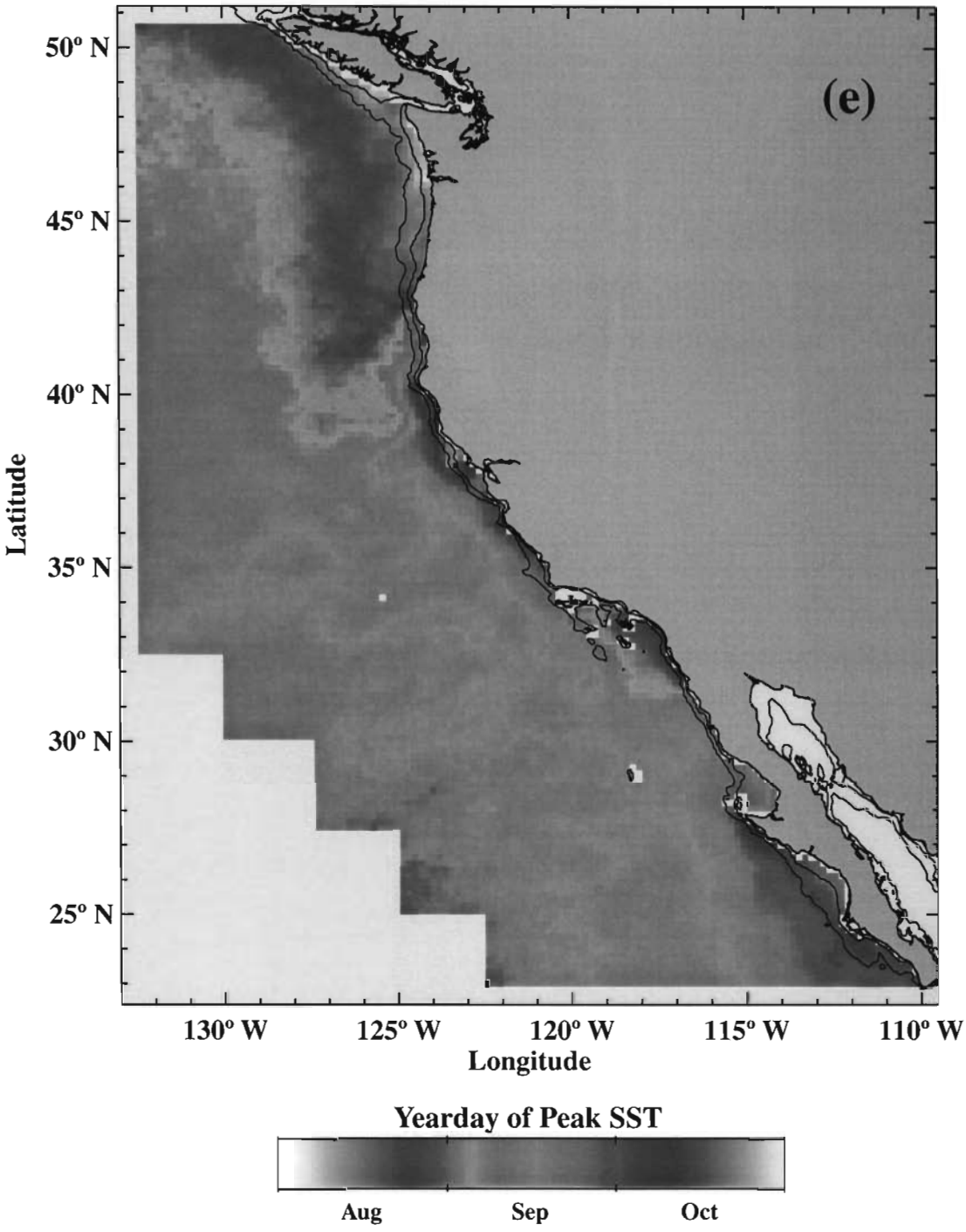

Figure 5.1 - *Continued*
(e) Phase of the annual harmonic.

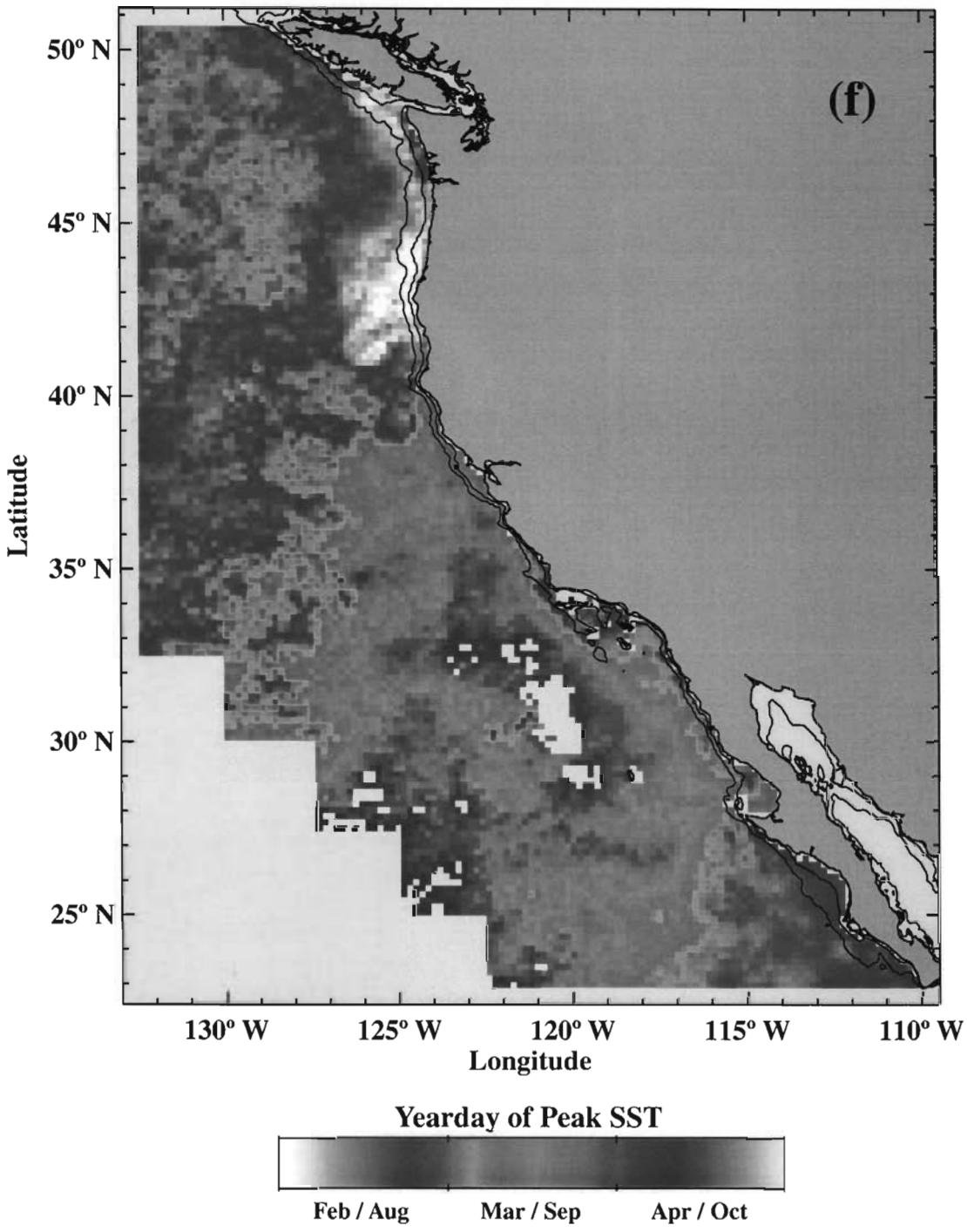

Figure 5.1 - *Continued*
(f) Phase of the semiannual harmonic.

is routinely advected to the south, depressing surface temperatures along the outer boundary of the SCB [Strub and James, 2000]. South of Point Conception at ~31° N, a portion of the CC core branches eastward toward shore to feed poleward flow into the eastern end of the SCB as part of a cyclonic recirculation feature historically referred to as the Southern California Eddy [Lynn and Simpson, 1987; Strub and James, 2000]. At the eastern end of the Bight, advection of warmer water from the south, weak spring and summer upwelling, reduced wind mixing and elevated surface heating raise mean temperatures well above those found to the west [Caldeira and Marchesiello, 2002; Strub and James, 2000; Winant and Dorman, 1997]. The remainder of the CC core continues southward along the Baja Peninsula, where elevated surface heating and lateral mixing with subtropical surface water from the west gradually erode its surface signature [Durazo and Baumgartner, 2002; Nelson and Husby, 1983]. At lower latitudes, strong surface heating aided by persistently cloudless conditions masks evidence of upwelling in mean SST adjacent to the Baja coastline, despite year-round equatorward winds [Nelson and Husby, 1983].

Annual amplitudes of SST are shown in Figure 5.1b. Coastal upwelling north of Point Conception depresses seasonal fluctuations of SST by arresting the summer heating cycle as cool water from depth replaces warmer water advected offshore with the Ekman drift. Inshore areas of depressed seasonality are confined to the shelf and slope north of central Oregon but expand seaward to the south, consistent with the expansion of upwelled waters associated with mesoscale jet and eddy activity [Strub and James, 2000; Strub et al., 1991]. Low amplitudes along the U.S. west coast are contiguous with low amplitudes in subtropical waters to the southwest. The latter are part of a larger swath of

low seasonality extending toward the tropics beneath the southeastern flank of the North Pacific high [Yashayaev and Zveryaev, 2001], where extensive and persistent summer cloud cover likely curbs surface heating [Nelson and Husby, 1983].

Close to the coast, consistently lower levels of summer cloud cover cause a strong gradient of incident solar radiation, increasing toward the coastline [Nelson and Husby, 1983]. North of Point Conception, coastal upwelling apparently overwhelms any shoreward increase in surface heating so that summer temperatures inshore remain much lower than those offshore. Within the SCB and along the Baja Peninsula, summer surface heating appears to play a more dominant role in mediating seasonal fluctuations of SST such that nearshore waters show a stronger seasonality than those found farther offshore. An area of very high annual amplitude lies along the inshore margin of southern Baja California, gradually expanding seaward south of Punta Eugenia (27.7° N) (Figure 1.1). Espinosa-Carreon et al. [2004] attribute seasonal temperature fluctuations along this stretch of coastline to upwelling and lateral heat advection. Yashayaev and Zveryaev [2001] however, identify this feature as part of a larger area of elevated annual amplitude extending throughout much of the Gulf of California and as far south as 20° N. The extent of this larger high-amplitude area suggests that seasonal cycles of SST south of Punta Eugenia are more closely associated with surface heat exchange driven by the seasonal advection of continental air from the Mexican mainland.

Semiannual amplitudes of SST are everywhere much less than annual amplitudes (Figure 5.1c), and the strength of the annual cycle largely determines the magnitude of seasonal fluctuations (Figure 5.2). Semiannual harmonics generally remain significant despite their lesser magnitude, accommodating asymmetric seasonal cycles by adjusting

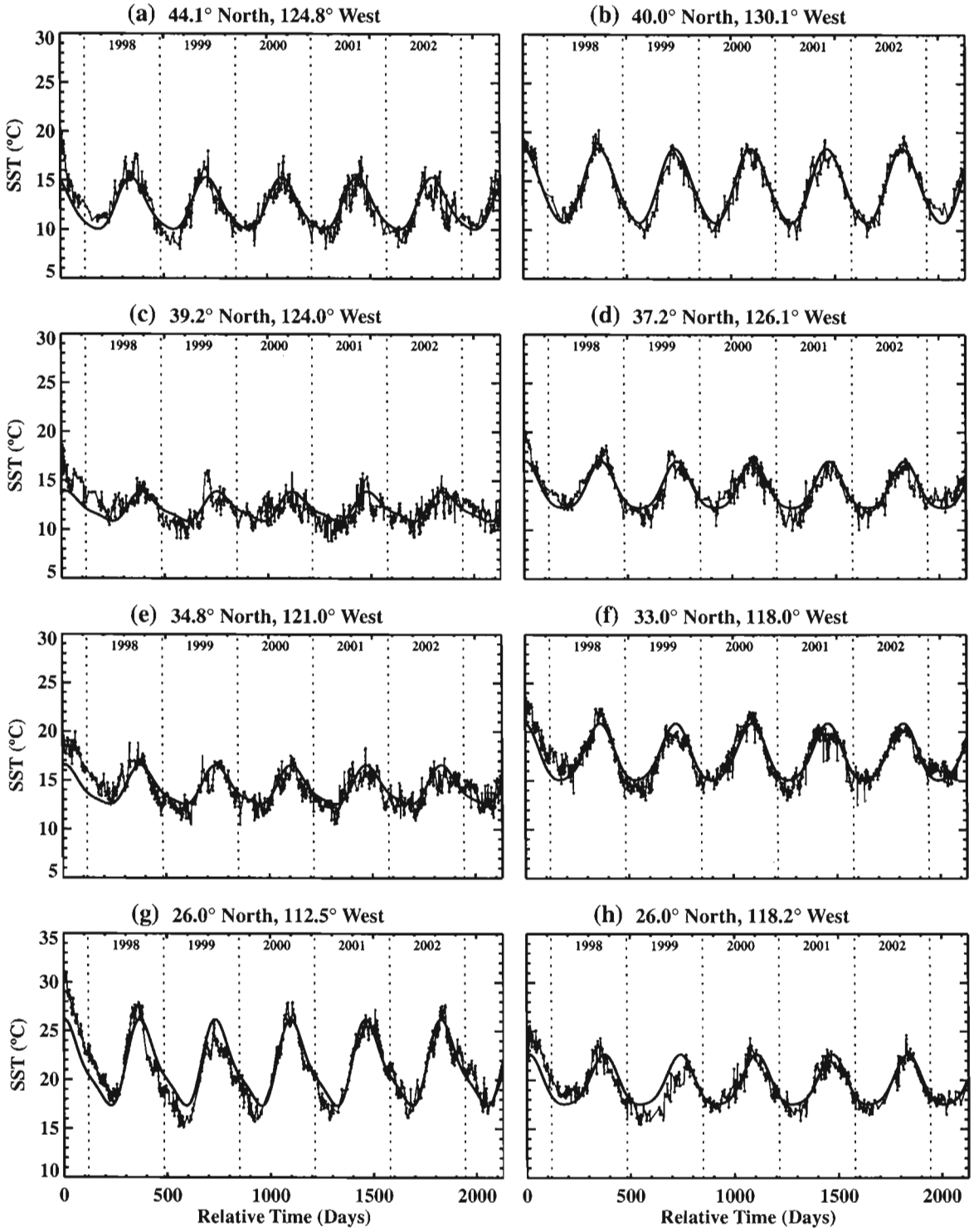

Figure 5.2 - *SST Time Series - Mean Seasonal Cycles*
Time series of Pathfinder SST assembled at locations shown in Figure 1.1. Trend lines represent mean seasonal cycles estimated from annual and semiannual harmonics.

the relative timing of seasonal maxima and minima. This point was similarly noted by Yashayaev and Zveryaev [2001] who suggest that, although a number of physical processes may introduce semiannual periodicity at mid-latitudes, semiannual cycles of SST generally arise through the attempt to model an asymmetric seasonal cycle with a limited number of harmonic frequencies. We therefore interpret semiannual amplitudes and phases in light of their apparent impact on the timing of seasonal extremes.

Figure 5.1d displays the fraction of total variance attributable to the mean seasonal cycle, where total variance was estimated according to the combined contributions of the seasonal variability described here and the interannual and dominant intraseasonal variability described in forthcoming chapters. Seasonal fluctuations dominate SST variability in the temperate waters of the North Pacific where annual amplitudes are very strong and seasonal cycles account for more than 90% of total variance (e.g. Figure 5.2b). Also consistent with the annual amplitudes of Figure 5.1b, seasonal variation is notably depressed along Vancouver Island and the U.S. west coast north of Point Conception, but most strongly so between Cape Blanco and Cape Mendocino (40.4° N) (Figure 1.1). The strength of seasonal fluctuations as a fraction of total variation is not noticeably elevated along the southern Baja coastline despite the presence of very strong annual and semiannual amplitudes.

Figures 5.1e and 5.1f describe the phases of annual and semiannual harmonics according to the yearday of peak SST attributable to annual and semiannual cycles. Within about 100 km of the U.S. west coast north of Point Conception, the phases of annual and semiannual cycles are largely determined by the timing, duration and intensity of the local upwelling season. Patterns in the spatial distribution of the annual phase

appear to be largely determined by the timing of seasonal minima, although the semiannual harmonic tends to shift actual minima to dates about one month later than they otherwise would be based on the annual cycle alone. Between Point Conception and Cape Mendocino where the annual cycle peaks from late September to mid-October (Figure 5.1e), minimum temperatures typically occur from late April to mid-May, several months following the arrival of seasonal minima farther offshore (compare Figures 5.2c-5.2e). About the time oceanic water temperatures drop to their seasonal lows in late-February or March, upwelling-favorable winds begin to strengthen along the California coastline [Dorman and Winant, 1995]. Cool water floods the shelf and upper slope at the onset of the spring transition [Strub et al., 1987] and surface temperatures continue to cool through April and into May as winds strengthen toward their late-spring or early summer maxima [Dorman and Winant, 1995].

Largier et al. [1993] note a tendency for monthly mean buoy surface temperatures along northern California to display two distinct minima associated with winter cooling and spring upwelling, with winter minima dominating to the north. A similar tendency is not generally evident in our daily time series. Mean seasonal cycles do show a progressive shift toward winter minima moving northward from Cape Mendocino (compare Figures 5.2a, 5.2c and 5.2e), following a shift toward stronger winter cooling, weaker spring upwelling and an often delayed onset of the spring transition relative to more southerly latitudes [Largier et al., 1993; Strub et al., 1987; Strub and James, 2000]. Seasonal maxima show a similar shift to earlier dates with increasing latitude, from late summer or early fall maxima along central California to mid- or late summer maxima along the Pacific Northwest. The timing of seasonal extremes is such that the weakest

annual amplitudes between Cape Blanco and Cape Mendocino (Figure 5.1b) reflect seasonal fluctuations between winter minima and summer maxima. Between Cape Mendocino and Point Conception, amplitudes generally reflect fluctuations between spring minima and late summer or early fall maxima, consistent with moored observations described by Dorman and Winant [1995].

Annual cycles of SST off the Baja Peninsula south of Punta Eugenia show a similar timing to that observed along central California, with late September or early October maxima and late March or early April minima (Figure 5.1e). Particularly strong semiannual harmonics generally peaking in late February/August (Figures 5.1c and 5.1f) shift seasonal minima to still later dates, typically late April or early May (e.g. Figure 5.2g). The arrival of minimum temperatures is generally concurrent with maximum equatorward wind stress and is therefore consistent with a spring cooling driven by coastal upwelling [Espinosa-Carreon et al., 2004]. Spring minima however, adhere to the spatial distribution of strong semiannual cycles peaking in February/August, extending seaward from the coastline at Punta Eugenia to as far as 600 km offshore of the southern tip of the peninsula. The timing of seasonal minima must therefore be determined in part by processes acting over much larger scales, such as surface cooling mediated by the advection of continental air. Seasonal cycles peak in mid-September, largely in phase with neighboring oceanic waters (compare Figures 5.2g and 5.2h). Seasonal maxima are delayed only slightly where annual cycles peak later in the year, consistent with the equatorward advection of cool water from the upwelling center at Punta Eugenia.

Seasonal cycles of surface temperature at the eastern, inshore end of the SCB are somewhat out of phase with those of surrounding waters (compare Figures 5.2e and 5.2f).

Annual cycles with February minima and August maxima lead the March minima and September maxima found to the south and west (Figure 5.1e). Semiannual harmonics peaking in February/August over much of the western Bight (Figure 5.1f) extend August maxima to the Channel Islands and shift September maxima somewhat closer to shore. Semiannual harmonics further shift western minima to slightly later dates and eastern minima to slightly earlier dates. While spring minima along the outer boundary of the Bight are consistent with the advection of cool, upwelled water from the north, the timing of seasonal fluctuations along southern California is otherwise consistent with differences in local wind forcing between the inner Bight and waters offshore. The sharp change in coastal orientation at Point Conception shelters surface waters along the northern and eastern margins of the SCB from prevailing northwesterly winds during all seasons [Winant and Dorman, 1997]. Upwelling within the interior of the Bight at the onset of the spring transition is generally too weak to shift seasonal minima within the inner Bight from the winter minima typical of oceanic waters. The disparate timing of seasonal maxima between the inner Bight and waters to the south and west supports a substantial role of local heating in the evolution of SST within the Bight, as suggested by Caldeira and Marchesiello [2002]. Reduced wind mixing throughout the spring and summer provides for a shallow mixed layer and a more strongly stratified upper water column [Caldeira and Marchesiello, 2002]. Suppression of the downward transfer of heat by turbulent diffusion may cause surface heating and cooling to play a more prominent role in the phasing of seasonal cycles within the inner Bight and may cause seasonal maxima to arrive at earlier dates, nearer to the mid-summer maxima of the surface heating cycle.

We could invoke a similar explanation for the broad lobe of August annual maxima lying offshore of the Pacific Northwest (Figure 5.1e), a southerly extension of a band of August maxima running along the coastlines of Alaska and British Columbia [Yashayaev and Zveryaev, 2001]. An annual excess of precipitation over evaporation increases upper ocean stability throughout this area [Husby and Nelson, 1982]. This area also lies beneath a band of negative wintertime wind stress curl resulting from the weakening and anticyclonic turn of prevailing winds as they round the Aleutian low [Murphree et al., 2003b]. Improved upper ocean stability coupled with a tendency for convergent surface flow beneath anticyclonic winds may shift annual maxima and minima to progressively earlier dates toward shore. Nearshore waters of the Pacific Northwest are further influenced by freshwater discharge from the Columbia River (46.1° N) (Figure 1.1) and Juan de Fuca Strait (48.2° N), which may be responsible for early February/August semiannual maxima (Figure 5.1f) that tend to shift seasonal maxima and minima to still earlier dates. Finally, a broad and relatively coherent band of February/August semiannual maxima extends from the northern California and Oregon coastlines to the southwest and beyond the boundary of our study region. This feature appears to have little if any influence on the timing of seasonal minima, but it does consistently shift seasonal maxima to earlier dates, typically by about one week. The origin of this feature is unclear, although its spatial pattern suggests a possible association with changes in surface pressure and marine layer winds at the change of the seasons.

5.2 Chlorophyll

Mean chlorophyll concentrations reflect prominent, region-wide patterns of surface enrichment (Figure 5.3a). Mean concentrations are greatest over shelf and slope waters, where upwelling driven by equatorward wind stress and cyclonic wind stress curl provide the dominant means of upward entrainment of new nutrients. In the absence of sustained wind forcing, various processes including episodic upwelling, sediment resuspension and interactions between tidal or coastal currents and shelf/slope morphology maintain a narrow high-pigment band adjacent to the coastline [Thomas and Strub, 1989]. The lateral advection of nutrient-rich subarctic water from the north and west [Strub and James, 2003] contributes to high concentrations throughout the Pacific Northwest despite relatively weak upwelling driven by variable summer winds. The seaward expansion of moderately elevated concentrations off the California coastline is consistent with summer upwelling driven by strong and sustained equatorward winds and with the expansion of productive waters associated with mesoscale jet and eddy activity [Strub and James, 2000; Strub et al., 1991]. Similarly elevated concentrations extending southeastward along the outer boundary of the SCB coincide with cooler average temperatures (Figure 5.1a), and are maintained by the advection of nutrients and biota from the upwelling center near Point Conception and by local enrichment associated with the doming of nutrient isopleths at the center of the Southern California Eddy [Thomas and Strub, 1990; Chelton, 1982]. Low concentrations lie above the deep basins of the eastern Bight, where warm oceanic waters are introduced by the northeastward turn of the CC core and where local upwelling and wind mixing are weak [Caldeira and

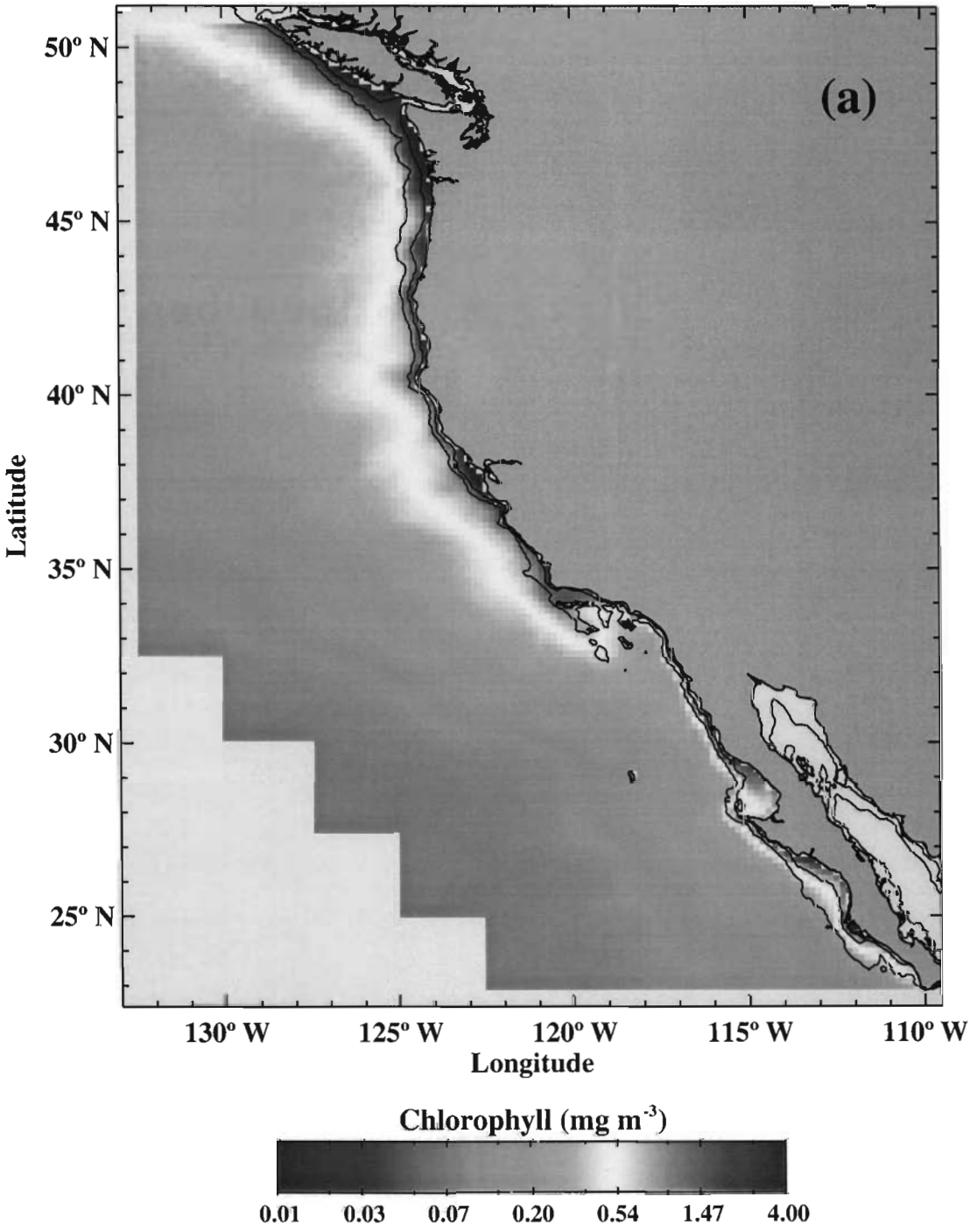

Figure 5.3 - *Mean Seasonal Cycle Fit to Chlorophyll Time Series*
(a) Mean chlorophyll estimated from the offset of the harmonic fit.

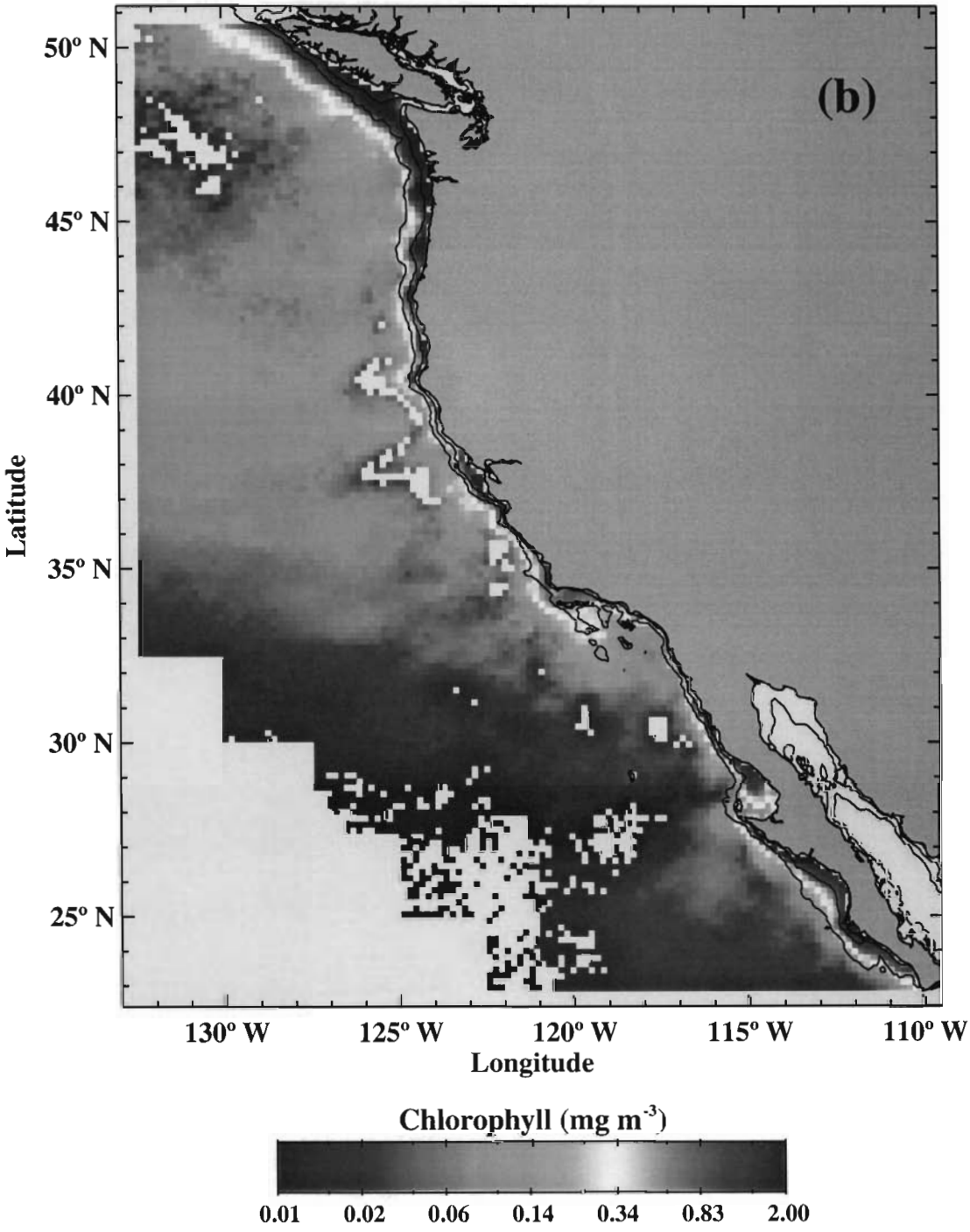

Figure 5.3 - *Continued*
(b) Amplitude of the annual harmonic.

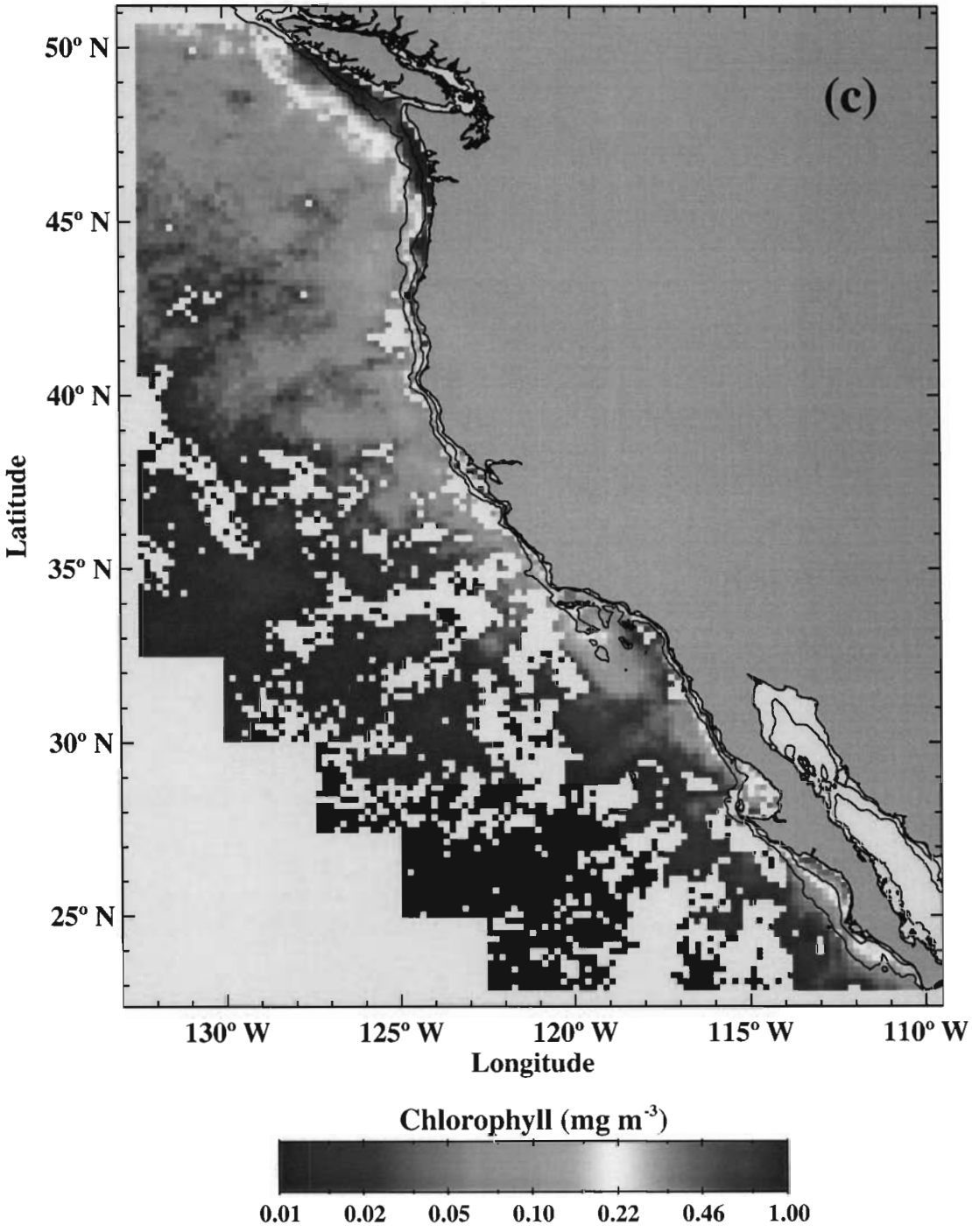

Figure 5.3 - *Continued*
(c) Amplitude of the semiannual harmonic.

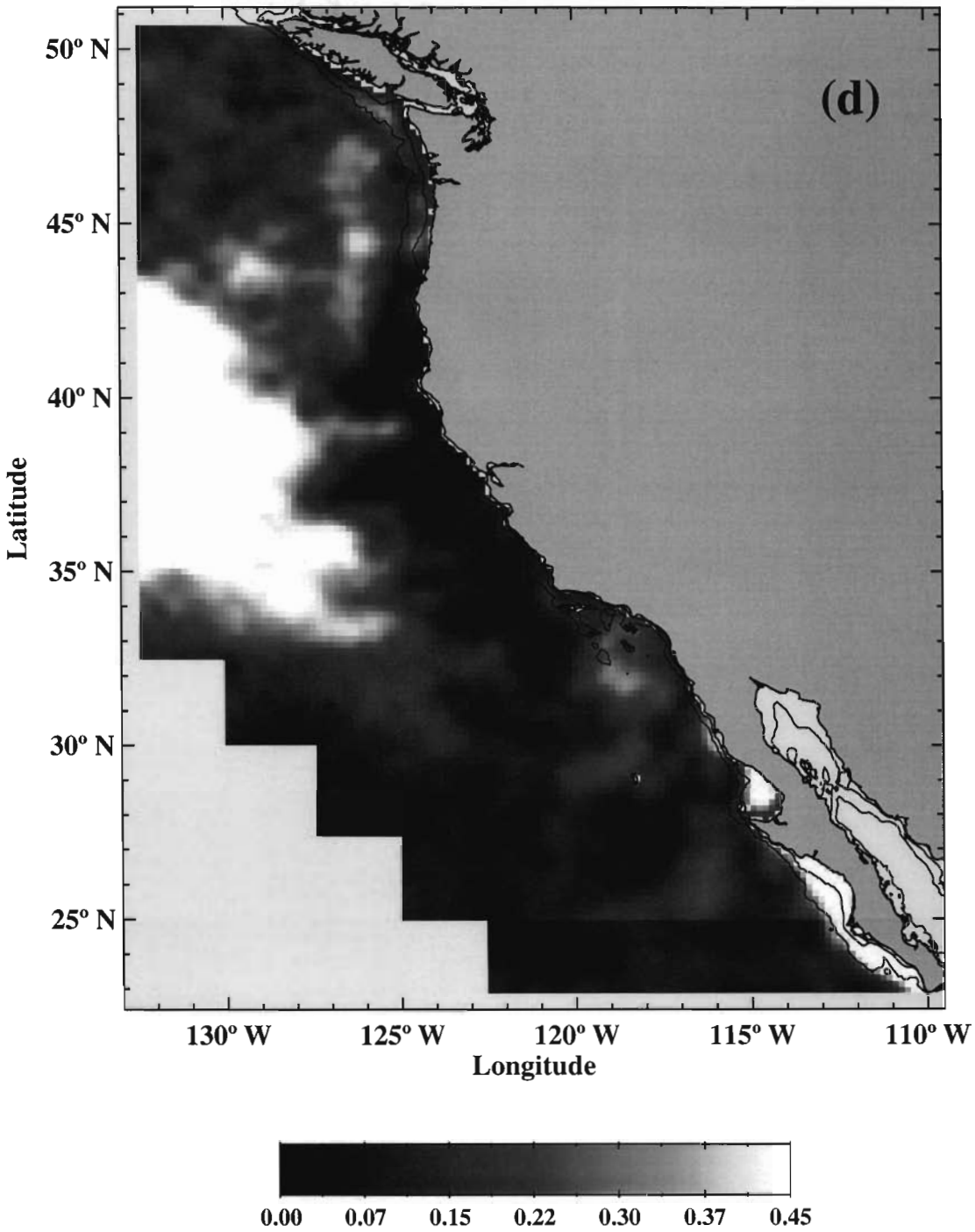

Figure 5.3 - *Continued*
(d) Fraction of total chlorophyll variance contributed by annual and semiannual harmonics. Total variance was approximated as the sum of variance contributed by the mean seasonal cycle, dominant intraseasonal variability and interannual variability. Data were smoothed with a 5 x 5 moving average.

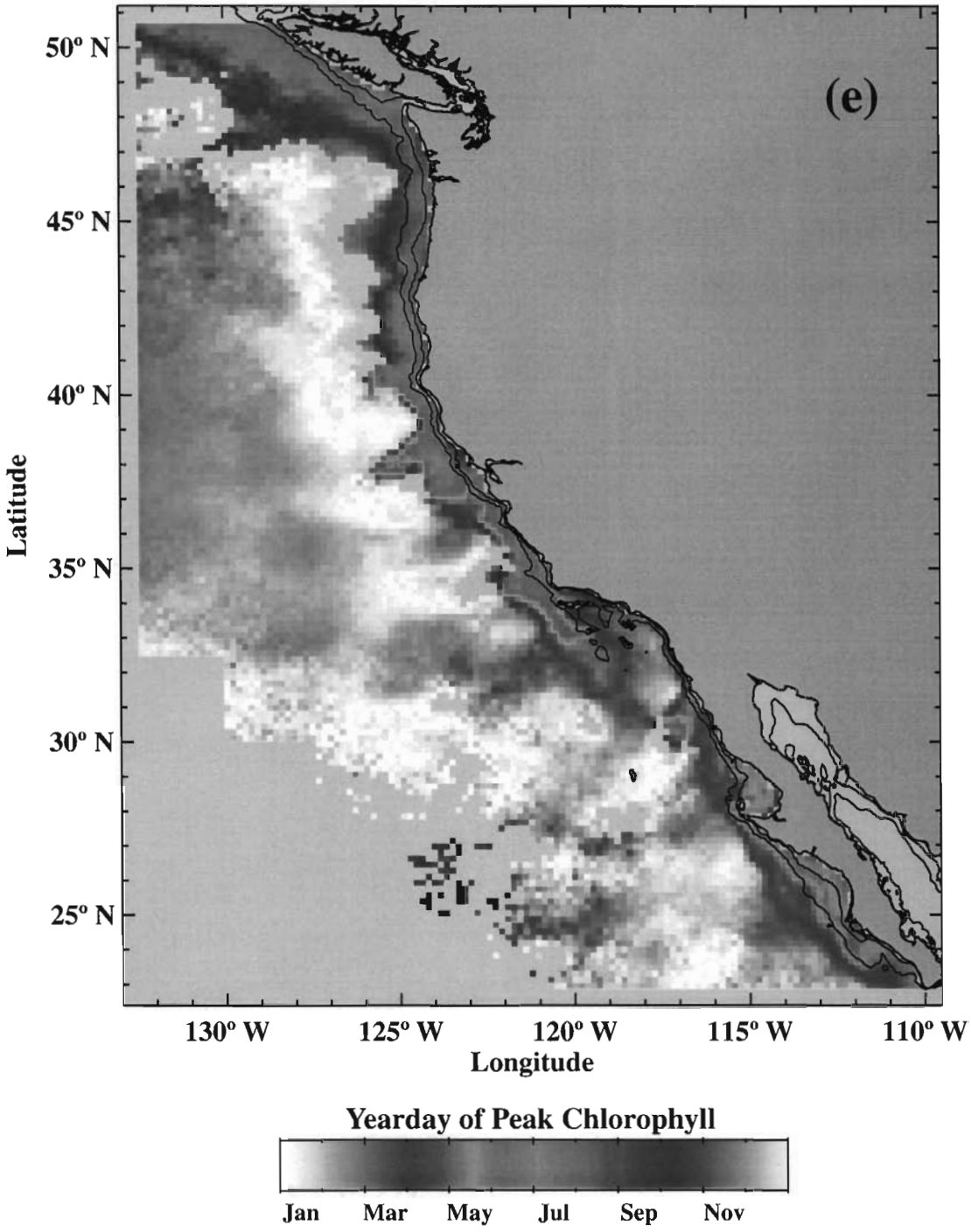

Figure 5.3 - *Continued*
(e) Phase of the annual harmonic.

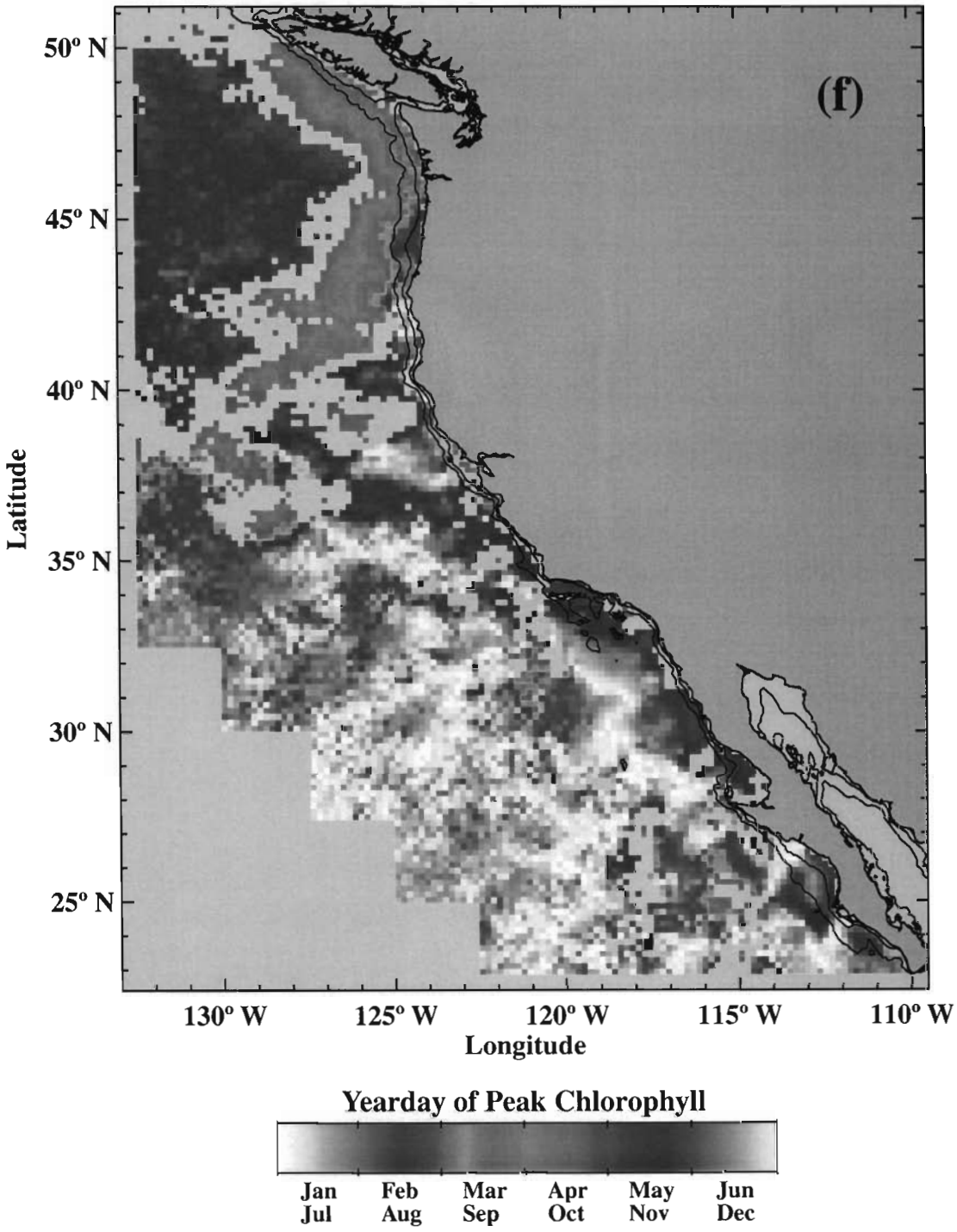

Figure 5.3 - *Continued*
(f) Phase of the semiannual harmonic.

Marchesiello, 2002; Hayward and Venrick, 1998; Strub and James, 2000]. High concentrations along the Baja Peninsula are retained over the shelf and slope.

Estimates of annual and semiannual amplitudes are provided in Figures 5.3b and 5.3c. Amplitudes of both harmonics are typically significant at the 80% level where they exceed 0.02 mg m^{-3}. Seasonal fluctuations are strong along central California near the Gulf of the Farallones and Monterey Bay (36-38° N) (Figure 1.1) but are considerably weaker to the immediate north and south. Weak amplitudes near Cape Mendocino and Point Arena (39.0° N) (Figure 1.1) generally coincide with weak seasonal cycles of SST (Figures 5.1b-5.1d) and with strong seasonal cycles of alongshore wind stress, alternating between the sustained equatorward winds of summer and the storm-forced poleward winds of winter [Dorman and Winant, 1995; Thomas et al., 2001]. Seasonal fluctuations contribute little to the total variance of nearshore chlorophyll from Cape Blanco to Point Conception (Figures 5.3d, 5.4a, 5.4c and 5.4e), where seasonal contributions to total SST variance are similarly depressed by spring and summer upwelling (Figure 5.1d). Annual and semiannual amplitudes are weak within the eastern half of the SCB and along the northernmost stretch of Baja California (Figures 5.3b and 5.3c), consistent with perennially weak winds and the inshore intrusion of oceanic surface waters from the west [Strub and James, 2000; Winant and Dorman, 1997]. Elevated amplitudes along the outer boundary of the Bight suggest a strong seasonal modulation of the intensity or length of the high-pigment extension to the southeast of Point Conception, as was described by Thomas and Strub [1990]. Inshore annual and semiannual cycles are very strong across the northern CCS, where seasonal cycles of coastal wind forcing and incident solar radiation (reinforced by seasonal cycles of cloud cover) are also strong.

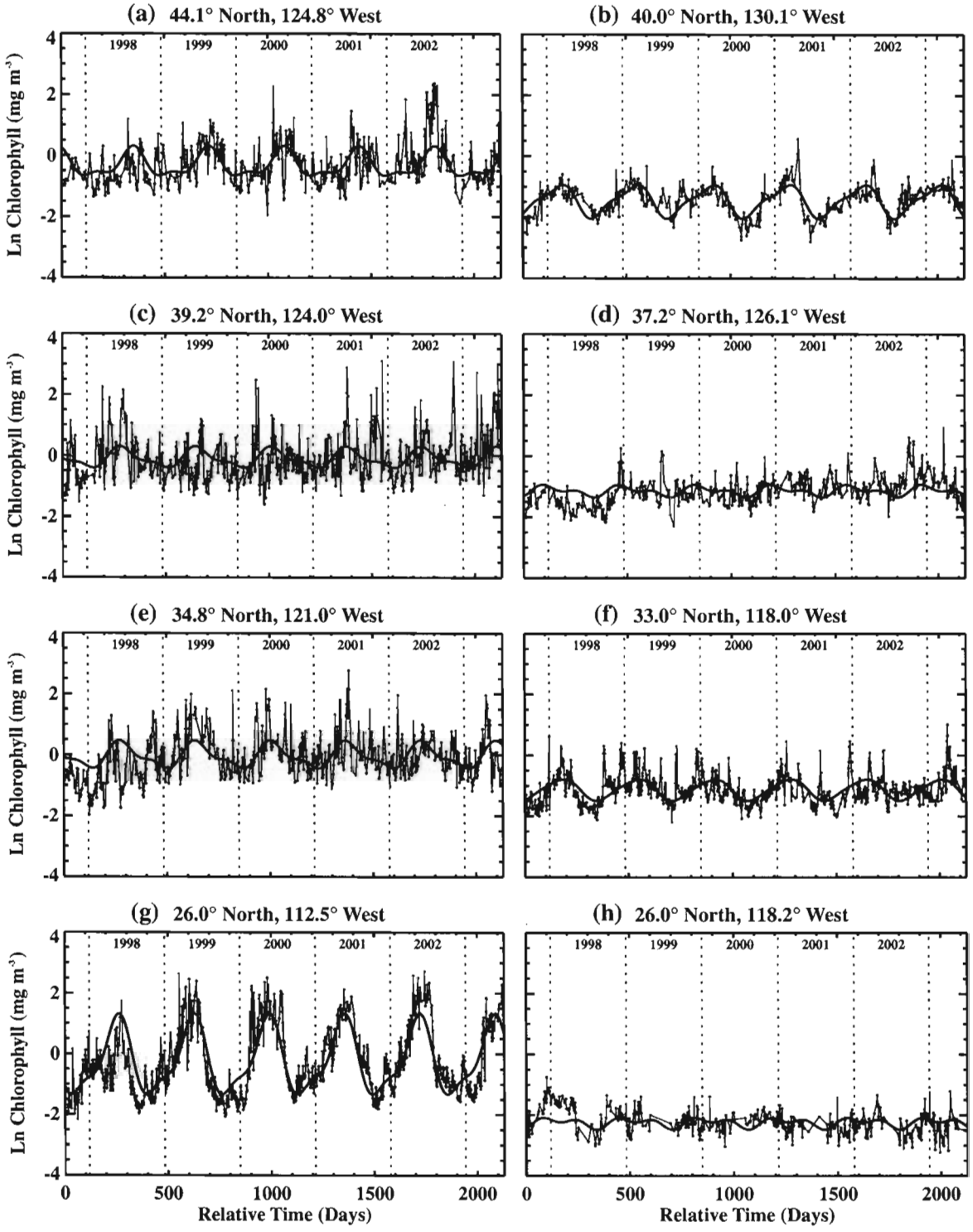

Figure 5.4 - *Chlorophyll Time Series - Mean Seasonal Cycles*
Time series of ln-transformed SeaWiFS chlorophyll assembled at locations shown in Figure 1.1. Trend lines represent mean seasonal cycles estimated from annual and semiannual harmonics.

Chlorophyll seasonality is of comparable strength along South-central Baja, where seasonal fluctuations contribute the majority of total variance (Figures 5.2d and 5.4g). South of Punta Eugenia, strong chlorophyll seasonality coincides with strong SST seasonality (Figure 5.1b) and it seems likely that processes other than local upwelling drive seasonal fluctuations.

Perhaps the most striking feature evident within seasonal variations of SeaWiFS chlorophyll is a narrow, meandering ribbon of weak and statistically insignificant annual amplitude estimates lying some 100-300 km offshore of northern California between 37° and 41° N (Figure 5.3b). The CC core typically follows a very similar path through the early summer, meandering several hundred kilometers offshore of Cape Mendocino and Point Arena as it flows equatorward through California waters [Kosro et al., 1991; Strub and James, 2000; Strub et al., 1991]. The inshore edge of the summertime jet acts as a more or less continuous physical and biological boundary. Inshore waters are cool and nutrient-rich, with variable but generally high abundances of phytoplankton dominated by large, neritic diatoms. Chlorophyll concentrations are greatest near the surface and production is maintained by the introduction of new nutrients from a shallow or outcropping nutricline. Offshore surface waters are warm, depleted of nutrients, and support a phytoplankton assemblage largely comprised of small, solitary cells. Typical of the oligotrophic open ocean, phytoplankton biomass is low and chlorophyll maxima lie near a deep nutricline [Chavez et al., 1991; Hood et al., 1991; Hood et al., 1990; Kosro et al., 1991].

The significance of the current core with respect to SeaWiFS imagery derives from the segregation of inshore and offshore water masses whose annual cycles of near-

surface chlorophyll content (beyond the continental margin) are of comparable magnitude (Figure 5.3b) but opposing phase (Figure 5.3e). The zonal band of comparatively strong open ocean annual amplitudes (~0.2 mg m^{-3}) between ~35° and 43° N represents the eastern end of the North Pacific transition zone, where summer stratification alternates with deep winter mixing and strong annual cycles with summer minima and winter maxima generally dominate near-surface chlorophyll fluctuations (Figures 5.3d and 5.4b) [Longhurst, 1998]. In contrast, annual cycles of inshore chlorophyll at these latitudes generally fluctuate in phase with equatorward winds [Thomas et al., 2001], with summer maxima and winter minima (Figure 5.3e). Annual amplitudes are depressed along the boundary between inshore summer maxima and offshore summer minima (e.g. Figure 5.4d), which along northern California appears to be determined by the position of the meandering CC jet. No such structure is evident in seasonal variations of SST, where inshore and offshore cycles fluctuate with more similar phases (Figure 5.1e, and compare Figures 5.2b-5.2e).

The path of the CC jet is highly variable, often maintained for several weeks at a time but capable of rapid and dramatic reorientation within a matter of days [Huyer et al., 1991]. The signature of a narrow frontal feature within the mean seasonal evolution of surface chlorophyll is testimony not of the jet's constancy in any given year, but rather of its year-to-year recurrence and apparently close association with coastal topography or shelf/slope morphology. Several numerical models have suggested the topographic trapping of current meanders where major coastal protrusions such as Cape Mendocino and Point Arena cause the seaward deflection and intensification of alongshore flow [Batteen, 1997; Haidvogel et al., 1991; Marchesiello et al., 2003]. Based on a series of

stratified laboratory experiments, Narimousa and Maxworthy [1987, 1989] interpret the meander off Point Arena not as the result of flow instability, but as the first standing wave generated by the Mendocino Ridge.

We should also note that local growth or loss of phytoplankton could cause the surface chlorophyll front associated with the CC jet to diverge from the path of the jet itself, in which case the meandering boundary evident in Figures 5.3b and 5.3e may not actually trace the true mean path of the summer current core. The seaward extension of high chlorophyll concentrations is in part caused by the entrainment and seaward advection of nutrients and biota from rich coastal waters [Hood et al., 1990; Hood et al., 1991; Strub et al., 1991]. Yet downwelling along the path of the meandering jet may cause considerable attenuation of the surface chlorophyll signal moving offshore of its coastal origin [Barth et al., 2002]. Perhaps more importantly, the upward tilting of isopycnals associated with the high-speed flow draws cool, nutrient-rich water upward along the inshore side of the jet, providing a source of local enrichment capable of stimulating intense phytoplankton growth [Chavez et al., 1991; Hood et al., 1990; Hood et al., 1991; Kosro et al., 1991]. During early and mid-July 1988, Chavez et al. [1991] mapped an area of high surface nitrate, surface chlorophyll, and diatom abundance inshore of the Point Arena jet, extending south to ~37.5° N. Although concurrent near-surface velocity fields suggest weak and poorly organized onshore flow at this latitude [Huyer et al., 1991], the CC jet continued to flow several hundred kilometers seaward of central California and did not itself define the southern boundary of high-chlorophyll, as may be suggested by Figures 5.3b and 5.3e.

The Point Arena jet lies at the northern end of a broader region of more convoluted flow along central California, where multiple filaments and jets extend from local upwelling centers and coherent equatorward flow is embedded within a rich and more varied eddy field [Strub et al., 1991]. Average steric height profiles gathered along repeated cross-shelf transects off northern and central California suggest a general widening of the frontal zone south of Point Arena [Kosro et al., 1991]. Consistent with this description, a broader region of somewhat depressed annual amplitude and weak seasonal variation (Figures 5.3b and 5.3d) extends southward from central California and gradually blends into the very weak seasonality of the subtropical gyre. Annual summer maxima are confined within 50-100 km of the coastline between Monterey Bay and Point Conception but extend several hundred kilometers southeastward of Point Conception within a narrow feature running along the outer boundary of the SCB (Figure 5.3e). The CC core itself flows some 100-200 km farther offshore [Brink et al., 2000; Lynn and Simpson, 1987; Strub and James, 2000], suggesting that local inshore circulation features are responsible for the seaward boundary and southeastward extension of summer chlorophyll maxima.

There is no indication of inshore summer maxima within the SCB or along the northern Baja Peninsula, save for a small feature at 30° N, 117° W, apparently associated with a recurrent cyclonic eddy near San Quintín (Figure 5.3e) [Peláez and McGowan, 1986; Soto-Mardones et al., 2004]. Annual phase estimates emphasize the oceanic character of the inner Bight. Weak seasonal cycles peak in mid- to late winter (e.g. Figure 5.4f) when the thermocline is relatively deep and chlorophyll is evenly distributed throughout the mixed layer [Michaelsen et al., 1988]. During spring and early summer,

density layers shoal and tilt upward toward the coastline, but not so far as to allow the nutricline to intersect the surface. Although episodic wind events may thereafter draw nutrients into the surface layer, biomass is concentrated within deep chlorophyll maxima at the base of the thermocline, below the upper attenuation depth of the euphotic zone and generally deeper than the sampling depth of the SeaWiFS instrument [Hayward and Venrick, 1998; Michaelsen et al., 1988]. Near-surface concentrations drop to their annual minima in mid- to late summer, as cyclonic flow within the Southern California Eddy strengthens [Lynn and Simpson, 1987; Strub and James, 2000], surface temperatures approach their seasonal maxima (Figure 5.1e) and the upper water column becomes most strongly stratified [Michaelsen et al., 1988].

Farther to the south along central and southern Baja, chlorophyll concentrations over the shelf and upper slope adhere to a similar annual cycle as that observed north of Point Conception, generally peaking with maximum equatorward winds in late spring (Figure 5.3e) [Espinosa-Carreon et al., 2004]. Although surface circulation offshore the Baja margin is generally dominated by the meandering core of the CC and associated eddy activity [Soto-Mardones et al., 2004], a coherent jet path is not evident in seasonal patterns of chlorophyll variability as is the case off California. This likely follows from the extremely weak seasonality of the adjacent subtropical gyre (Figures 5.2b-5.2d and 5.4h), although Soto-Mardones et al. [2004] observed that the formation and evolution of eddies and meanders generally do not display a regular seasonal dependence.

From the southern tip of the Baja Peninsula to at least as far north as central California, semiannual cycles within several hundred kilometers of the coastline generally peak in mid- to late spring/fall (Figure 5.3f). With the exception of the inner

Bight, annual and semiannual cycles describe a mean seasonality of satellite-derived surface chlorophyll consistent with the previously published work of Abbott and Barksdale [1991], Espinosa-Carreon et al. [2004], Peláez and McGowan [1986], Strub et al. [1990], Thomas et al. [2001], Thomas et al. [1994], and Thomas and Strub [2001, 1990, 1989]. Winter concentrations are generally low with a relatively uniform offshore distribution. A typically diffuse bloom extending well offshore follows the spring transition to strong and sustained equatorward winds. Chlorophyll-rich filaments begin to form shortly thereafter. The outer boundary of productive waters develops a scalloped appearance by mid- to late summer as the upwelling front and jet meander offshore of the continental margin. Inshore concentrations peak at about this same time, coincident with maximum equatorward winds and upwelling. At this point, however, the spatial distribution of high concentrations is determined as much by patterns of mesoscale circulation as by patterns of wind forcing. Coastal concentrations thereafter drop as winds weaken and temperatures climb toward their seasonal maxima. A generally diffuse cross-shelf expansion of productive waters follows in late summer or early fall, as poleward coastal currents displace the summer circulation structure offshore [Strub and James, 2000]. Concentrations thereafter subside to winter levels.

A similar progression takes place off the Pacific Northwest, although the retention of the summertime upwelling front and jet over the continental margin contribute to a different phasing of annual and semiannual cycles (Figures 5.3e and 5.3f). Inshore annual phases north of Cape Blanco appear to be largely determined by the occurrence of winter minima, common to inshore waters north of Point Conception (compare Figures 5.4a, 5.4c and 5.4e). Semiannual maxima shift to progressively later dates moving

poleward of northern California, apparently reflecting a similar shift in the arrival of seasonal maxima from July off southern Oregon to August and early September off Washington and Vancouver Island. North of Cape Mendocino, the annual harmonic captures the seaward migration of productive waters through the fall and into winter, consistent with the diffuse fall expansion described by others [Strub et al., 1990; Thomas and Strub, 2001; Thomas et al., 1994] and consistent with the seaward displacement of the equatorward jet [Strub and James, 2000]. A continuous band of insignificant phase estimates roughly parallels the coastline north of Cape Mendocino, suggesting year-to-year variability in the timing of this fall chlorophyll expansion. Lastly, semiannual harmonics peaking in late March/September or early April/October tend to shift seasonal minima to slightly earlier mid-summer dates along a broad band extending southwestward from the shores of Washington and Oregon. This band roughly coincides with a comparable feature in the semiannual phase of SST (Figure 5.1f). Here again, the effect of this feature is slight and its origin is unclear.

Chapter 6

INTERANNUAL VARIABILITY

Following removal of the mean seasonal cycle from chlorophyll and SST time series, a Gaussian kernel with a 365-day full width at half maximum was applied to the residuals to obtain an estimate of variation acting over interannual time scales. Figure 6.1a displays the variance of the smoothed residual series of SST, examples of which are plotted in Figure 6.2. Although surface temperatures show moderately elevated interannual variance along much of the coastline, the strongest variability is concentrated within two relatively distinct areas. The first extends some 200 km offshore of southern Oregon and northern California. The second lies along the coast of southern Baja, extending offshore to a more or less meridional boundary at ~116 ° W and from the coastline at ~30° N to a zonal boundary near 24° N. Although very near to the southern edge of our study region, this latter area appears distinct from any similarly elevated SST variability farther to the south. As a fraction of total variance (Figure 6.1b), elevated interannual variability along Oregon and northern California is of comparable strength to the mean seasonality described in the previous section. This is not the case along Baja California.

The launch of SeaWiFS and the beginning of our study period occurred in the midst of the 1997-1998 El Niño, the strongest on record by several measures [McPhaden, 1999] and a dominant cause of elevated interannual variance of SST. Westerly wind anomalies over the western equatorial Pacific at the end of 1996 and early in 1997 initiated the collapse of the trade winds and the eastward expansion of the western Pacific

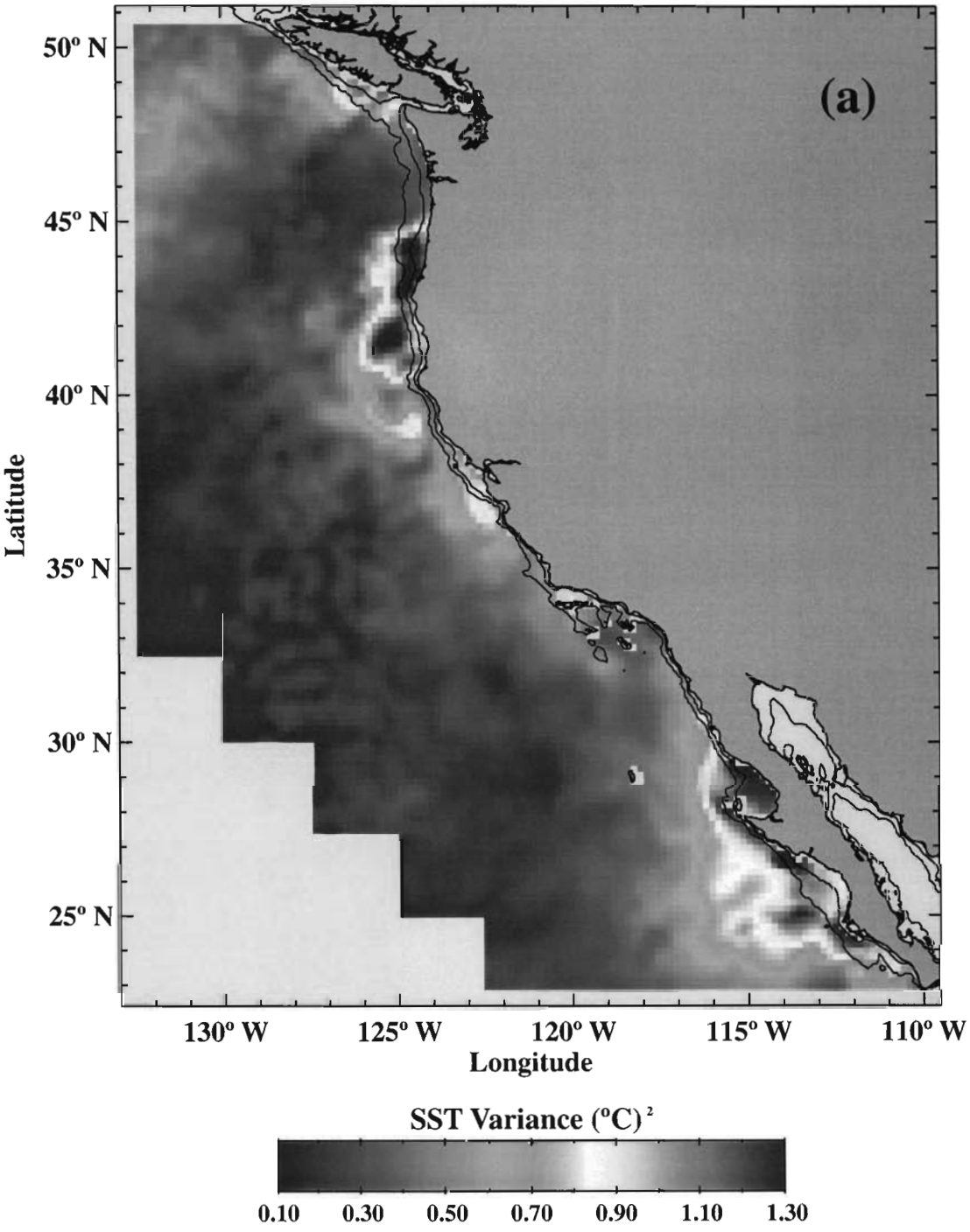

Figure 6.1 - *Interannual Variance of SST Time Series*
(a) Interannual variance of SST, estimated as the variance of smoothed time series following the application of a low-pass Gaussian filter to non-seasonal residual time series. Data were smoothed with a 5 x 5 moving average.

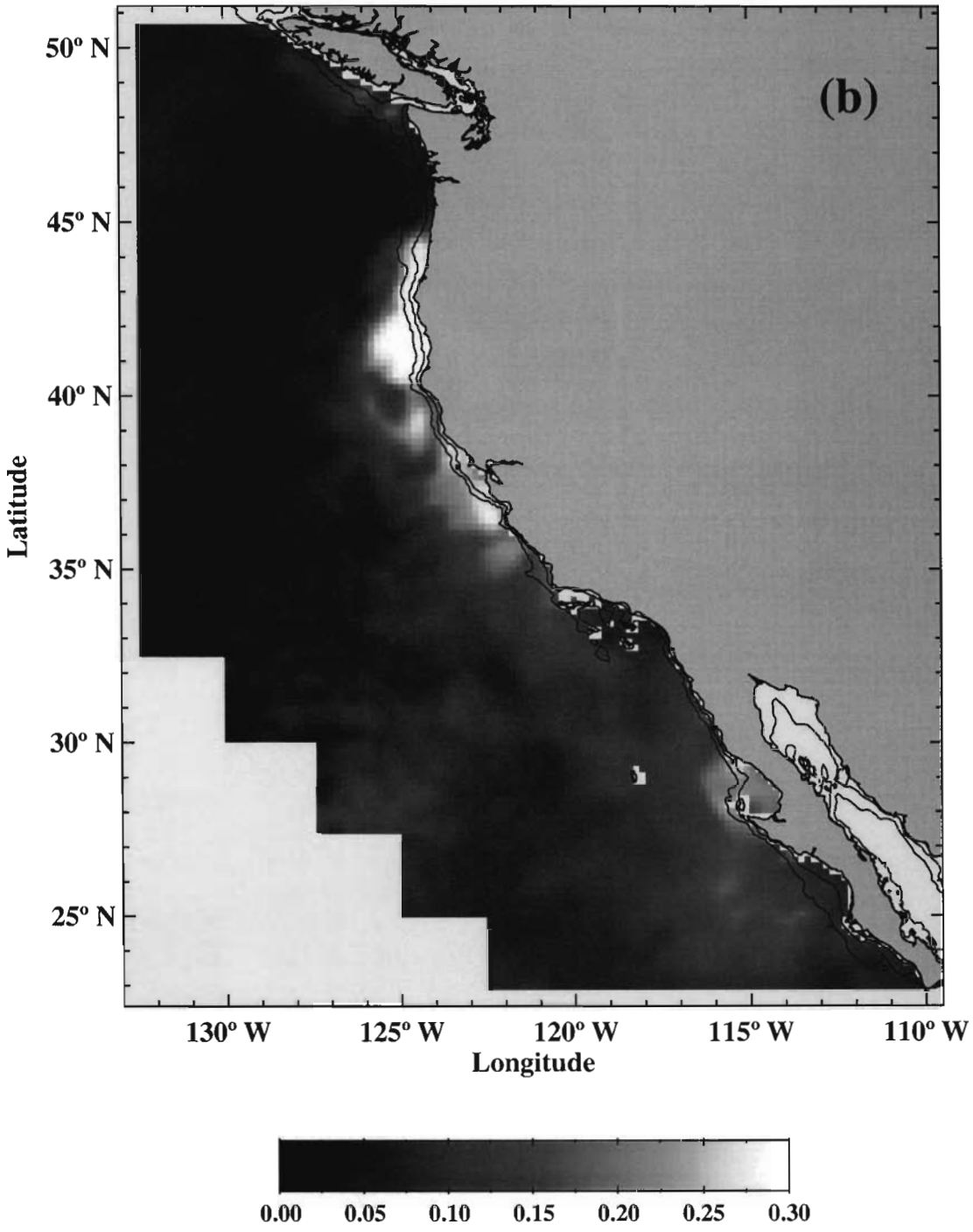

Figure 6.1 - *Continued*
(b) Fraction of total SST variance contributed by interannual variability. Total variance was approximated as the sum of variance contributed by the mean seasonal cycle, dominant intraseasonal variability and interannual variability. Data were smoothed with a 5 x 5 moving average.

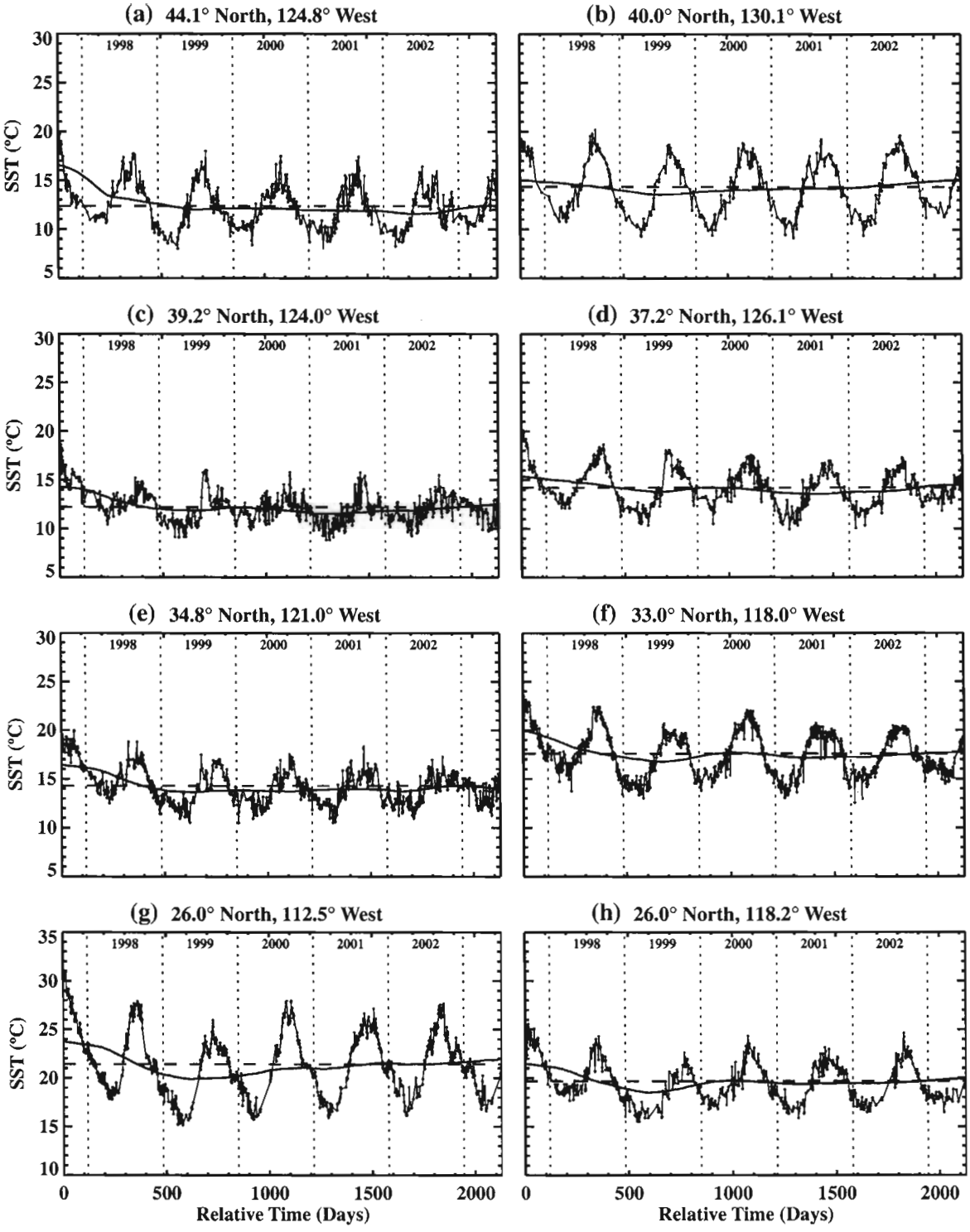

Figure 6.2 - *SST Time Series - Interannual Variability*
Time series of Pathfinder SST assembled at locations shown in Figure 1.1. Solid trend lines represent interannual variation estimated by filtering non-seasonal time series. Broken horizontal lines indicate annual mean SST values.

warm pool. The progressive intensification of westerly winds excited a series of Kelvin waves that propagated eastward along the equator to the South American coastline [McPhaden, 1999]. Equatorial waves impinging on the eastern boundary in turn excited poleward propagating, coastally trapped waves whose passage produced marked changes in local hydrography and current structure by depressing the thermocline, elevating coastal sea levels, and promoting the transport of warm and salty (spicy) water from the south [Strub and James, 2002]. Propagating oceanic disturbances were reinforced by regional atmospheric anomalies manifest as an unusually weak North Pacific high through the summer of 1997 and a strengthened Aleutian low through the following winter [Schwing et al., 2002; Strub and James, 2002]. Negative sea level pressure and cyclonic wind anomalies over the northeast Pacific forced poleward, downwelling-favorable winds along the coast, further contributing to the accumulation of heat within the coastal ocean by forcing onshore Ekman transport and by strengthening poleward flow [Schwing et al., 2002]. Local atmospheric and distant oceanic forcing combined during the fall and winter of 1997-1998 to produce extreme surface temperature anomalies throughout much of the region (Figure 6.2) [Durazo and Baumgartner, 2002; Kosro, 2002; Lynn et al., 1998; Peterson et al., 2002; Schwing et al., 2002; Smith et al., 2001; Strub and James, 2002].

As described by Durazo and Baumgartner [2002], anomalous advection appears to have played a dominant role in the evolution of water property anomalies off the Baja Peninsula during peak El Niño conditions. Hydrographic surveys conducted off Baja California in October 1997 and January 1998 found a strengthened and greatly expanded poleward undercurrent and a broad system of poleward surface currents coalescing into a

narrow jet over the shelfbreak north of ~30° N. The equatorward flow of cool and fresh subarctic water within the CC core was deflected offshore of ~116° W by a broad front of spicy water within the upper 100 m. Temperature and salinity distributions clearly identified the dominant source of spicy surface waters not as tropical surface water from the south as may have been expected, but as subtropical surface water from the west. Tropical surface water appears to have been blocked at the Gulf of California by an intruding mass of high temperature, high salinity surface water originating in the subtropical gyre. The eastward advance of this water mass and its subsequent entrainment within a system of inshore poleward currents provided the principle means with which extremely warm and salty surface waters were distributed throughout the region, at the expense of cooler water from the north. The pattern of elevated SST variance seen off Baja California in Figure 6.1a is similar to the January 1998 pattern of elevated near-surface spiciness as reported by Durazo and Baumgartner [2002], although they do not resolve the outer boundary of this feature south of ~27° N. An intrusion of warm water from the west, however, may help explain the sharp drop in SST variance at ~24° N (Figure 6.1a).

Along the Oregon coast, the passage of propagating oceanic disturbances had clearly contributed to the warming of subsurface waters by September [Lynn et al., 1998; Smith et al., 2001]. Surface temperature anomalies, however, remained separated from those at depth by a strong seasonal thermocline [Smith et al., 2001], suggesting a leading influence of atmospheric forcing in the early development of SST anomalies. Monthly SST anomalies (not shown) suggest that the spatial distribution of elevated interannual variance along Oregon and California is largely a product of the relative intensity of

anomalies present at the onset of our study period. Off central Oregon, the summer of 1997 was one of record low levels of coastal upwelling, with surface temperatures already near typical seasonal maxima by early summer [Peterson et al., 2002]. Although nearshore temperatures fell somewhat in mid-summer during the season's only period of sustained upwelling, a strong southwesterly storm initiated intense downwelling in late August [Peterson et al., 2002] coincident with the arrival of a propagating coastal wave [Kosro, 2002]. Equatorward currents quickly reversed and surface temperatures rose to record levels in September [Kosro, 2002; Smith et al., 2001]. Offshore of Newport, Oregon (44.6° N), the highest temperatures were associated with the onshore movement of a mass of low salinity water that had originated at the Columbia River during an unusually strong spring freshet [Smith et al., 2001]. This fresh water plume should have enhanced surface heating by improving the stability of the surface layer, and may in part explain the very strong gradients of SST variance seen in Figure 6.1a.

Farther to the south, weak or poleward winds were not sustained until the winter of 1997-1998 [Lynn et al., 1998]. Cold-water bands and weak upwelling filaments were present off much of the California coastline throughout most of the summer [Strub and James, 2002]. Surface temperatures off central California peaked with the passage of a coastal wave in August but dropped thereafter [Chavez et al., 2002; Kosro, 2002; Schwing et al., 2002] as equatorward flow resumed through September [Strub and James, 2002]. Cool upwelling filaments were once again visible off Cape Mendocino and Point Arena [Strub and James, 2002] and were evidently strong enough to have caused the patterning of SST variance seen in Figure 6.1 off northern California. Because our study period began in the middle of these events, Figure 6.1 may present a somewhat biased

depiction of characteristic patterns of SST variance acting over interannual scales. This figure does indicate, however, that local mesoscale processes off northern California can substantially mitigate the impact of basin-scale forcing of surface temperature patterns.

Surface temperatures throughout the CCS gradually fell to normal levels through the spring and summer months of 1998 (Figure 6.2) as El Niño conditions dissipated and spicy waters were displaced by the renewed equatorward flow of subarctic water [Durazo and Baumgartner, 2002; Hayward et al., 1999; Smith et al., 2001]. There were clear indications of a basin-wide transition to cool La Niña conditions by July, conditions that would build during the latter half of 1998 and linger over the Northeast Pacific for the next three years [Hayward et al., 1999; McPhaden, 1999; Schwing et al., 2002; Venrick et al., 2003]. Positive sea level pressure and anticyclonic wind anomalies over the Northeast Pacific forced unusually strong upwelling, low coastal sea levels and strengthened equatorward flow throughout the CCS [Hayward et al., 1999; Venrick et al., 2003]. Off Baja California, the cool surface temperatures that generally persisted throughout this period contributed to elevated levels of interannual variance of SST about as much as did the warm temperatures of the preceding El Niño (e.g. Figures 6.2g and 6.2h). Off the Oregon coastline, La Niña conditions had little impact on temperature and salinity distributions [Smith et al., 2001] and contributed little to elevated levels of interannual SST variance (e.g. Figure 6.2a). Smith et al. [2001] attribute this lack of impact to weaker meridional gradients of temperature and salinity found to the north of Oregon. A greater level of change should therefore follow the anomalous poleward transport of El Niño than should follow the strengthened equatorward flow of La Niña.

Perhaps the most recognizable impact of El Niño and La Niña events on the ecosystems of the CCS arise through changes in nutrient availability. The anomalous onshore Ekman transport and downwelling coastal waves of the 1997-1998 El Niño caused a downward displacement of the thermocline and nutricline, isolating the surface layer from water at depth and reducing the effectiveness of the wind-forced upward entrainment of new nutrients. Low nutrients limited primary production and phytoplankton abundance to well below typical levels throughout much of the region [Bograd and Lynn, 2001; Chavez et al., 2002; Corwith and Wheeler; Espinosa-Carreon, 2004; Kahru and Mitchell, 2000, 2002; Kudela and Chavez, 2002]. Off Monterey Bay, where *in situ* time series of nutrient and chlorophyll concentrations are the most extensive and most complete, negative surface chlorophyll anomalies began to build in early August with the intensification of coastal thermocline depth and SST anomalies [Chavez et al., 2002]. The nutricline progressively deepened through the fall and winter, resulting in the collapse of coastal chlorophyll and an inshore incursion of oligotrophic waters dominated by small-celled phytoplankton. Although the coastal thermocline partially recovered during the spring of 1998, an anomalous inshore displacement of fresher water within the CC core evidently suppressed the upward entrainment of nutrient-rich water through the spring and summer. Maximum nutrient and chlorophyll anomalies were observed at this time and a full recovery was delayed until October, coincident with the onset of cool SST anomalies [Chavez et al., 2002]. Conditions much the opposite of El Niño generally prevailed throughout the CCS during the next several years, when the strong and sustained equatorward wind anomalies of La Niña elevated the nutricline to unusually shallow depths [Bograd and Lynn, 2001; Chavez et al., 2002; Corwith and

Wheeler; Espinosa-Carreon, 2004; Kahru and Mitchell, 2000; 2002; Kudela and Chavez, 2002].

Figure 6.3a displays the variance of smoothed residual time series of chlorophyll and examples of those time series are shown in Figure 6.4. El Niño and La Niña conditions generally contributed to elevated levels of interannual variance by depressing and elevating chlorophyll concentrations, respectively (Figure 6.4). Elevated interannual variance adheres to a spatial distribution very similar to those of elevated mean concentrations and strong annual and semiannual amplitudes (Figures 5.2a-5.2c), suggesting that chlorophyll fluctuations acting over interannual scales are forced by the same processes that determine mean concentrations and the magnitude of seasonal fluctuations. This interpretation is consistent with the principle cause of interannual variability resting with the widespread vertical displacement of the nutricline during unusually strong and extended periods of coastal upwelling or downwelling. Although the recovery of inshore chlorophyll during the latter half of 1998 generally coincided with the drop of surface temperatures to near normal levels (compare Figures 6.2 and 6.4), the response of chlorophyll concentrations to El Niño and La Niña conditions appears to have been more locally variable. Furthermore, areas of the strongest SST response do not necessarily stand out as areas of particularly strong chlorophyll variance (and vice versa), suggesting that SST anomalies may have evolved somewhat independently of thermocline depth anomalies. Where this is the case, surface temperature need not necessarily reflect the physical events of greatest biological importance.

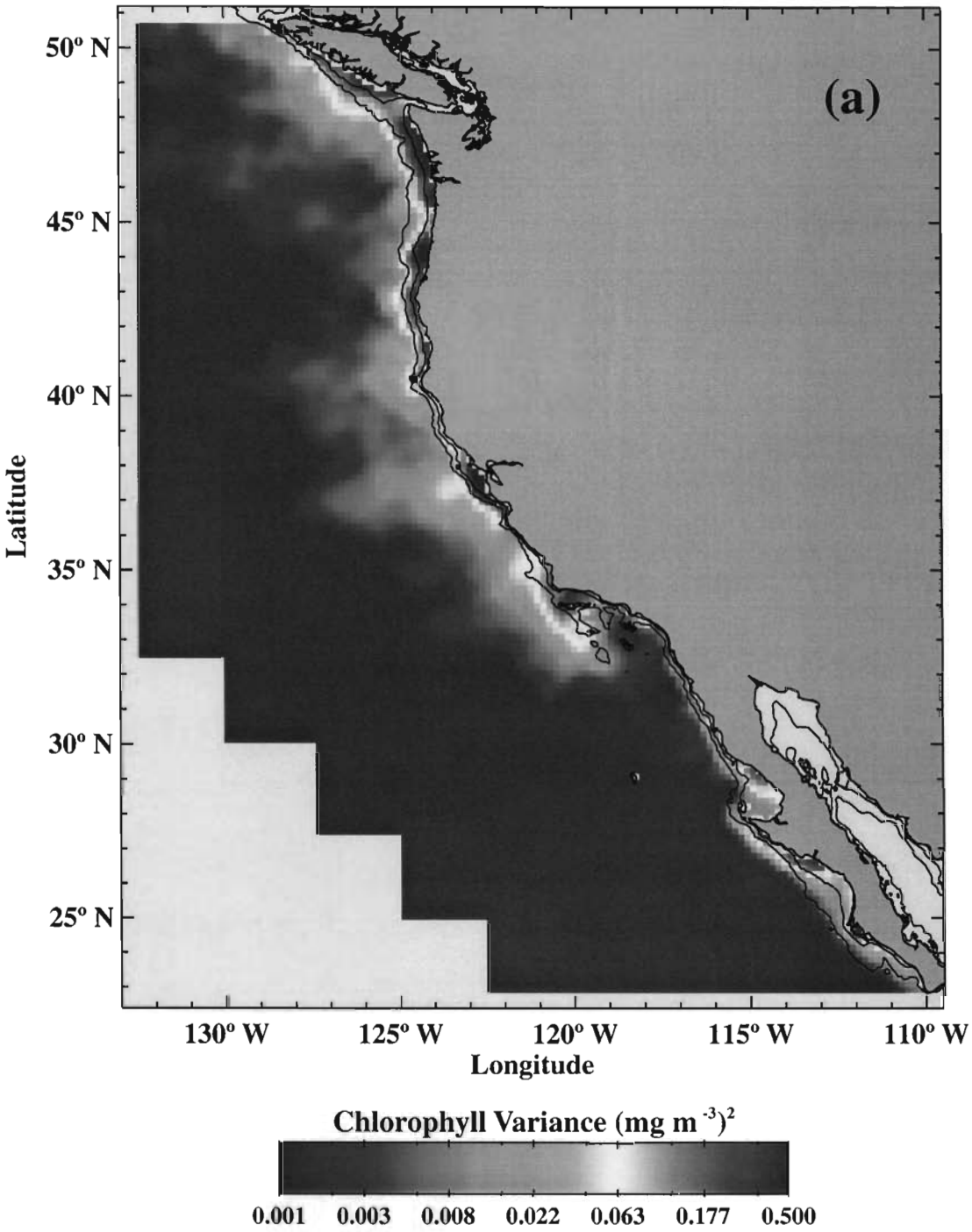

Figure 6.3 - *Interannual Variance of Chlorophyll Time Series*
(a) Interannual variance of chlorophyll, estimated as the variance of smoothed time series following the application of a low-pass Gaussian filter to non-seasonal residual time series. Data were smoothed with a 5 x 5 moving average.

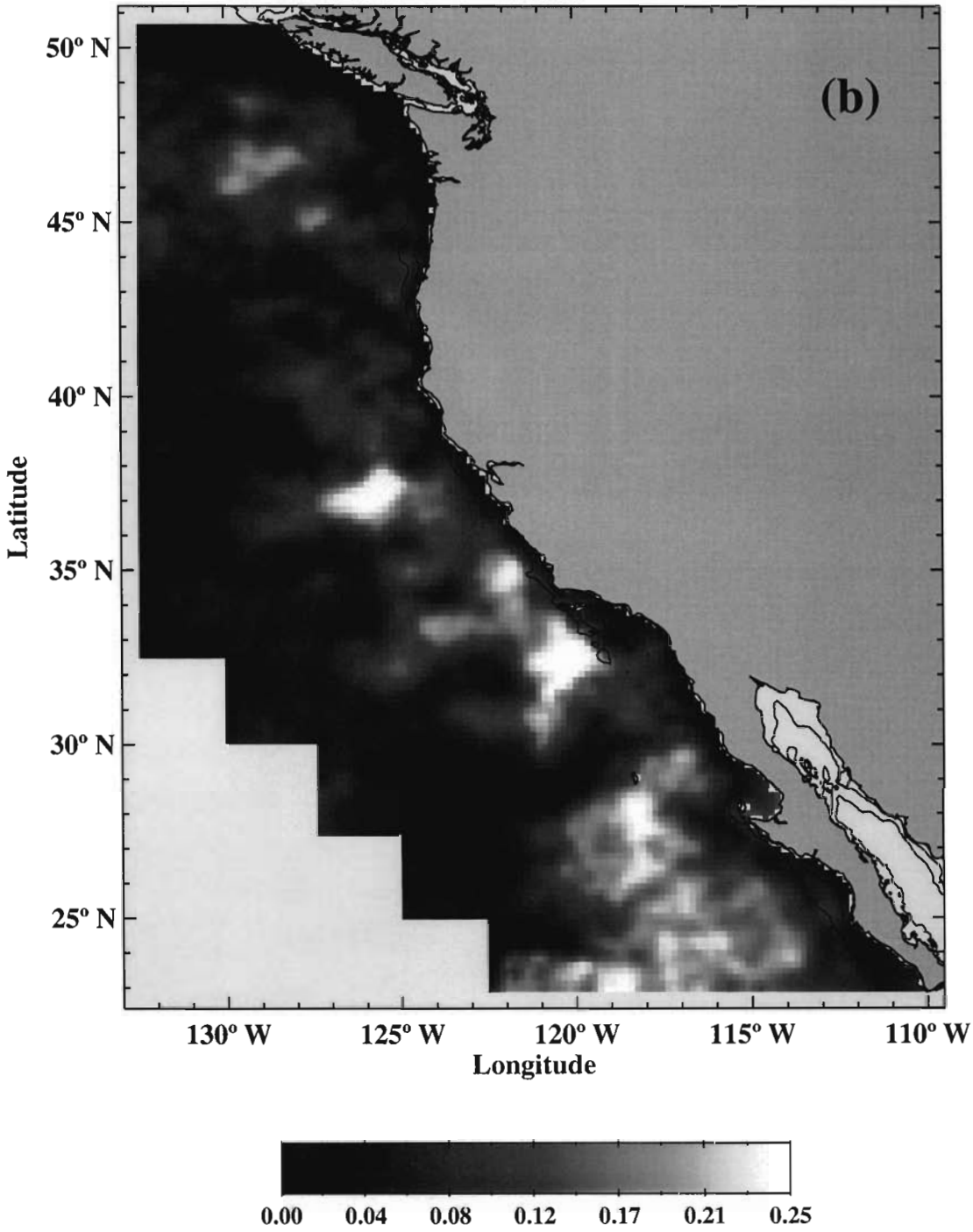

Figure 6.3 - *Continued*
(b) Fraction of total chlorophyll variance contributed by interannual variability. Total variance was approximated as the sum of variance contributed by the mean seasonal cycle, dominant intraseasonal variability and interannual variability. Data were smoothed with a 5 x 5 moving average.

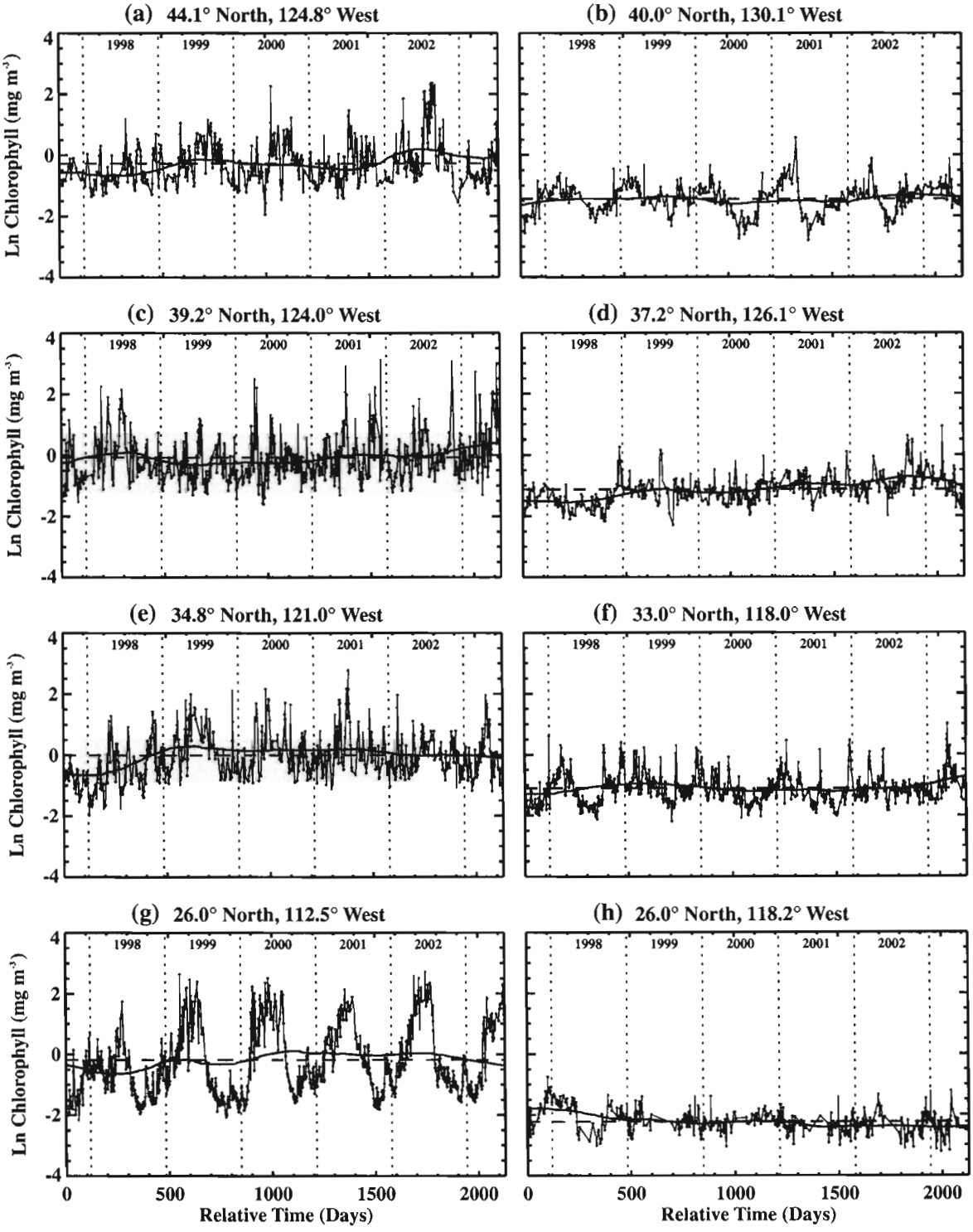

Figure 6.4 - *Chlorophyll Time Series - Interannual Variability*
Time series of ln-transformed SeaWiFS chlorophyll assembled at locations shown in Figure 1.1. Solid trend lines represent interannual variation estimated by filterin non-seasonal time series. Broken horizontal lines indicate annual mean chlorophyll concentrations.

As a fraction of total variance, a relatively narrow inshore band of very low interannual chlorophyll variability runs virtually the full length of the coastline (Figure 6.3b), indicating that coastal concentrations throughout the region are generally less affected by interannual change. Whereas interannual contributions to total SST variance are concentrated at the coast (Figure 6.1b), offshore chlorophyll concentrations appear to be most susceptible to interannual variation. Similar observations have been made by others. Whether maintained by episodic upwelling, runoff or other alternative means of enrichment, chlorophyll concentrations and modeled levels of new production near the coast at Monterey Bay were less sensitive to El Niño conditions than those farther from the coast [Chavez et al., 2002; Kudela and Chavez, 2002]. Inshore levels of new production also displayed a lesser sensitivity to the expansion of productive waters during cool La Niña conditions [Kudela and Chavez, 2002]. From five years of Coastal Zone Color Scanner imagery, Thomas and Strub [2001] found that the most consistent patterns of year-to-year variations in cross-shelf pigment distributions occur in waters seaward of a narrow coastal band. Pigment concentrations within these offshore waters appear to be most susceptible to negative deviations during El Niño and positive deviations during La Niña.

Whereas warm El Niño conditions were associated with lower than normal chlorophyll concentrations over shelf and slope waters off central and southern Baja, chlorophyll actually increased further from shore during the late fall and winter of 1997-1998 (compare Figures 6.4g and 6.4h). Positive anomalies in the oligotrophic ocean are responsible for the very large area of strong interannual contributions lying ~100-700 km offshore in Figure 6.3b. Kahru and Mitchell [2000] suggest that these positive anomalies

might have been caused by blooms of nitrogen-fixing cyanobacteria. Espinosa-Carreon [2004] argue that the phytoplankton assemblages responsible for these anomalies would have had to contain large concentrations of cells other than cyanobacteria in order for the unusually high chlorophyll concentrations to have been detected by standard SeaWiFS ocean color algorithms. This in turn suggests an unusual enrichment of offshore waters either through the upward entrainment of nutrients or through the advection of phytoplankton or nutrients from the north or east. Equatorward flow of subarctic water within the core of the CC was deflected well offshore of its typical path during this period [Durazo and Baumgartner, 2002] and may have contributed to offshore chlorophyll anomalies. Using a limited set of historic observations obtained at coastal stations along southern California and central Baja, Ladah [2003] document the episodic enrichment of warm surface waters during El Niño winters and further suggest that the periodic shoaling of nutrient-rich subsurface waters might have been partially responsible for offshore anomalies. It is not clear, however, whether conclusions drawn from these coastal locations might apply to such an expansive area of open ocean.

The consolidation of large interannual contributions to total chlorophyll variance within discrete pockets offshore of the California coastline (Figure 6.3b) suggests partial control of interannual variability through changes in mesoscale circulation. Between ~100 and ~500 km from shore, interannual variation is of a greater relative importance to chlorophyll fluctuations than to SST fluctuations (compare Figures 6.1b and 6.3b), implying that SST variability need not reflect interannual changes in physical structure important to offshore phytoplankton distributions. Sustained variations in the path of the CC core, the lengths or strengths of local upwelling jets and filaments, and the locations

or intensities of mesoscale eddies may affect chlorophyll distributions over interannual scales through several means, including the cross-shelf exchange of nutrients and phytoplankton and changes in nutricline topography. Durazo and Baumgartner [2002] observed unusually low levels of mesoscale activity offshore of the Baja Peninsula during the peak El Niño conditions of winter 1997-1998. Increased levels of coastal dynamic height caused decreased cross-shelf gradients of dynamic height and generally weaker flow. A virtual absence of cool and salty upwelled water reduced frontal structure between inshore and offshore domains. These changes apparently limited the role of instability processes in generating mesoscale current structure. Energetic patterns of surface circulation dominated by an intensified CC core returned with the transition to La Niña conditions during the latter half of 1998 [Durazo and Baumgartner, 2002]. Similar changes are likely to have occurred farther to the north and may in part explain the seaward extension of anomalous concentrations over interannual scales, as has recently been suggested for the Chilean upwelling system [Hormazabal et al., 2004].

Regional atmospheric conditions established at the onset of La Niña conditions in late 1998 and sustained through the spring of 2002 forced anomalous southward wind stress over the CCS and eastward stress over the eastern North Pacific Current (NPC) [Murphree et al., 2003a; Venrick et al., 2003]. Anomalous winds forced unusually strong southward transport from the Gulf of Alaska into the NPC, strong eastward transport within the NPC and strong equatorward flow within the CC [Murphree et al., 2003a; Strub and James, 2003; Thomas et al., 2003; Venrick et al., 2003]. These conditions ultimately led to a massive intrusion of subarctic water observed from Vancouver Island [Freeland et al., 2003] to Southern California [Bograd and Lynn, 2003] during the

summer of 2002. Cool temperatures and low salinities associated with this intruding mass were centered within the upper pycnocline and contributed to spiciness anomalies on par with those of the 1997-1998 El Niño, although of opposite sign [Freeland et al., 2003; Bograd and Lynn, 2003]. These conditions generally did not provide a comparable contribution to interannual SST variability (Figure 6.2), possibly owing to the mitigation of cooling trends by the development of warm El Niño conditions during the latter half of 2002. Patterns of atmospheric circulation had already shifted to those typical of El Niño by the summer of 2002 and positive SST anomalies followed the spread of cyclonic wind anomalies into the northern CCS later that fall [Murphree et al., 2003a; Venrick et al., 2003]. The El Niño of 2002-2003 was otherwise of little apparent consequence within the CCS [Venrick et al., 2003].

The transport anomalies that led to the subarctic intrusion of 2002 also provided for the widespread enrichment of the northern CCS. Off central Oregon, cold pycnocline waters were associated with high nutrient concentrations, a 2-3 fold increase in primary production and a 2-5 fold increase in chlorophyll fluorescence measured over the shelf [Wheeler et al., 2003]. Satellite-derived chlorophyll concentrations were unusually high through the spring and summer of 2002 over most of the inshore waters of the Pacific Northwest [Thomas et al., 2003], and these elevated concentrations contributed substantially to high levels of interannual variance (e.g. Figure 6.4a). Strong upwelling and equatorward flow within the CC promoted the dissemination of subarctic waters throughout the region so that by July, a cool, fresh and enriched water mass extending from the upper pycnocline to the sea surface lay offshore of the SCB [Bograd and Lynn, 2003]. Strong chlorophyll anomalies were observed more than 400 km offshore of

northern California during the fall of 2002, suggesting extensive equatorward advection of nutrient-rich water within the CC. Chlorophyll anomalies appear to have been distributed along the outer bounds of the CC core consistent with the equatorward advection of nutrients at depth followed by their upward displacement during episodes of strong wind mixing [Thomas et al., 2003]. The contribution of these positive anomalies to the elevated levels of interannual variance within the mesoscale patches seen off California in Figure 6.3b approaches that of the 1997-1998 El Niño and subsequent La Niña (e.g. Figure 6.4d). This suggests an alternative source of strong interannual variation of offshore chlorophyll concentrations forced at the northern boundary of the CCS.

Chapter 7

INTRASEASONAL VARIABILITY

Although physical forcing and biological response within the CCS act over a wide range of scales, variability is particularly intense over the mesoscales. Of fundamental interest to us is the degree to which various scales of change are evident within satellite-derived time series of surface temperature and chlorophyll, and the manner in which patterns of intraseasonal variability may relate to large-scale current structure and wind forcing. We use semivariograms as a means of describing the temporal behavior or variance structure of residual time series obtained from the removal of annual and semiannual harmonics and interannual variability. Figure 7.1 shows empirical semivariograms calculated from residual time series of SST and chlorophyll at locations shown in Figure 1.1. Empirical semivariograms show considerable structural variation and considerable point-to-point scatter. We employ EOF analyses of semivariance data as an objective means of isolating coherent structure of interest from scatter introduced by the incomplete sampling of daily time series. Although scatter caused by sampling irregularities may lead to a somewhat ambiguous interpretation of the structure evident within any given semivariogram, the first few EOF modes should provide a reliable description of dominant structure common to large areas.

EOF analyses of SST and chlorophyll semivariograms calculated over time lags of up to 100 days yielded 100 nonzero statistical modes ordered by the amount of semivariance structure explained by each. Analysis of both variables produced a very similar partitioning of overall structure between modes (Figure 7.2). Mode 1 captures the

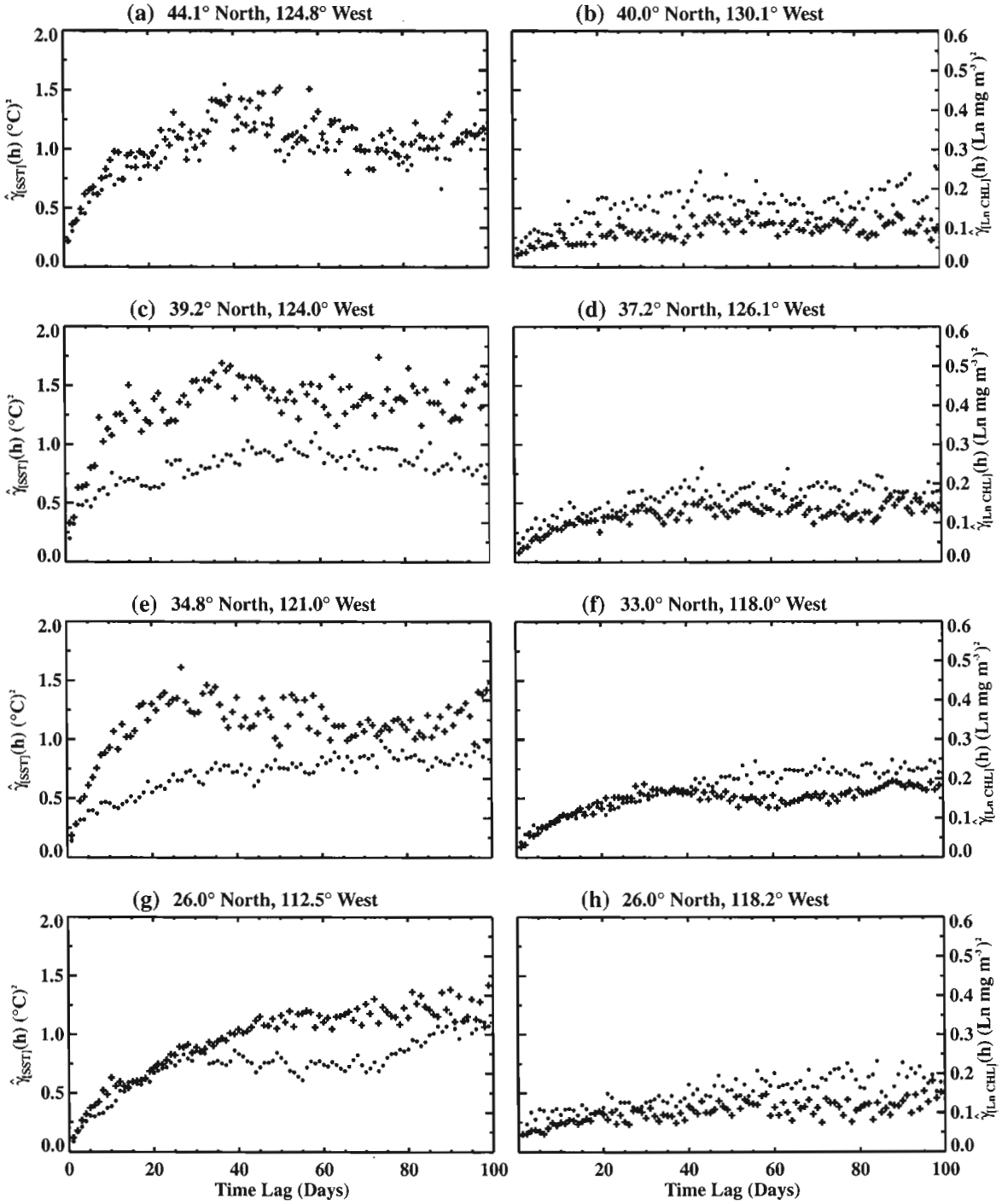

Figure 7.1 - *Empirical Semivariograms Calculated from Satellite-Derived SST and Chlorophyll*

Empirical semivariograms calculated from residual time series of Pathfinder SST (black dots) and ln-transformed SeaWiFS chlorophyll (red +) assembled at locations shown in Figure 1.1. SST and chlorophyll axes are plotted to the left and right, respectively.

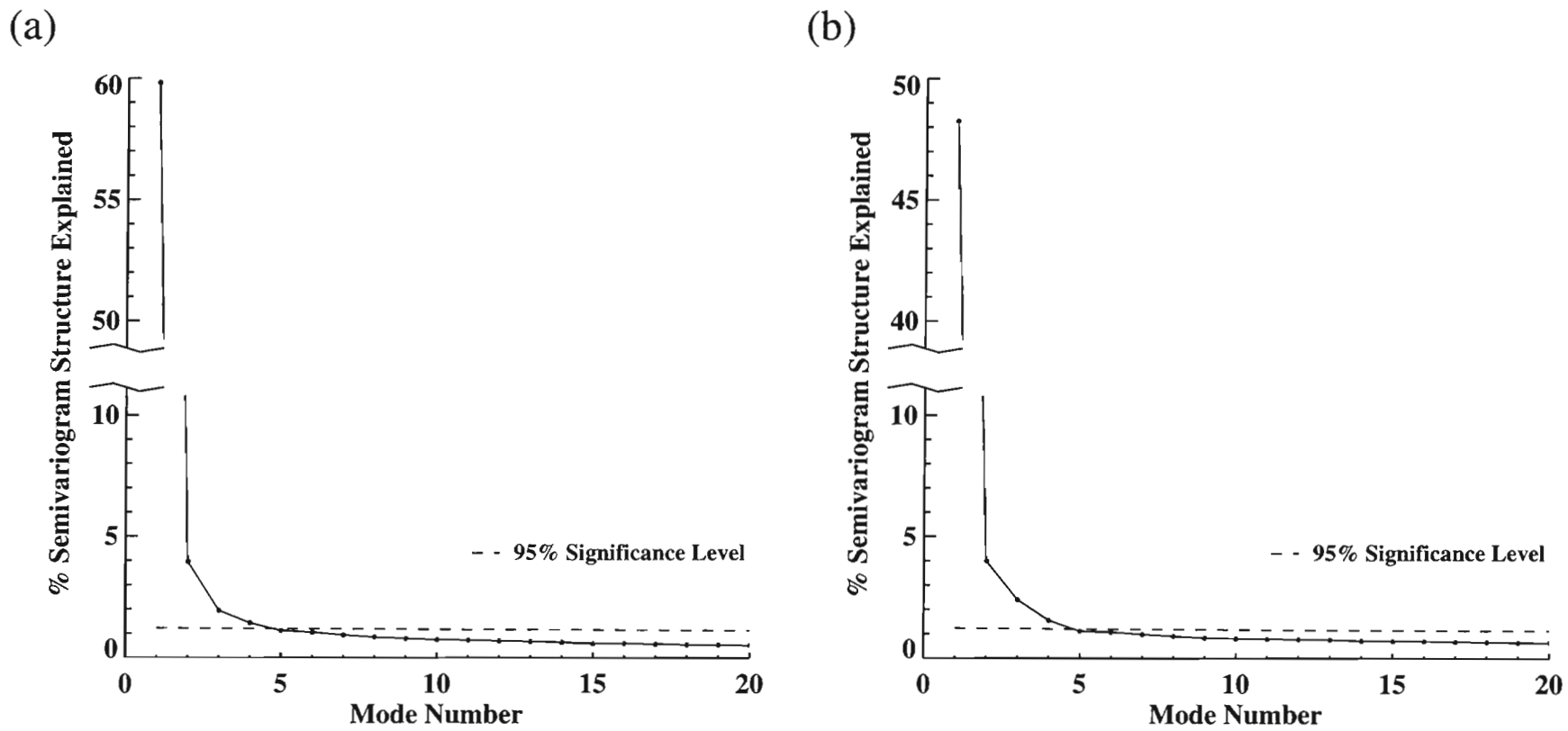

Figure 7.2 - *Partitioning of Semivariogram Structure by EOF Analysis*
Percentage of semivariogram structure explained by the first 20 EOF modes for (a) Pathfinder SST and (b) ln-transformed SeaWiFS chlorophyll. Dashed lines indicate 95% significance levels determined through analyses of random data [from Overland and Priesendorfer, 1982]. The first four, statistically significant modes explain 59.8%, 4.0%, 1.9% and 1.4% of SST semivariogram structure, and 48.3%, 4.0%, 2.4% and 1.6% of chlorophyll semivariogram structure.

most dominant semivariogram shape observed throughout the region, explaining 60% and 48% of SST and chlorophyll semivariance structure, respectively. Mode 2 explains 4% of the overall semivariance structure of both variables, little compared to that of mode 1 but clearly a statistically significant amount according to the criteria used here. Modes 3 and 4 are marginally significant. Structure not explained by the first four modes (32.9% and 43.7% of SST and chlorophyll structure, respectively) is distributed more or less evenly across the remaining insignificant modes, reflecting the considerable scatter evident within individual semivariograms (Figure 7.1).

7.1 SST

The large amount of semivariance structure captured by the first EOF mode indicates a dominant pattern of temporal variability reflected in a common semivariogram shape. That shape is given by the mode 1 EOF itself, presented in Figure 7.3a. The general form of this function follows a negative exponential curve, describing a monotonic increase in semivariance approaching an asymptotic upper bound. Where the mode 1 EOF is representative of empirical semivariograms, this upper bound defines the sill or overall variance of residual time series. Although Figure 7.3a suggests a decorrelation scale of something like 50-60 days, we will generally remain vague with respect to the selection of a specific decorrelation scale. While EOF analysis allows for the definition of dominant structure common to large areas, locally important structure may be relegated to statistically insignificant higher modes. Location-specific decorrelation scales are sensitive to small changes in semivariogram shape and are generally more spatially variable than the patterns of variance structure revealed by EOF

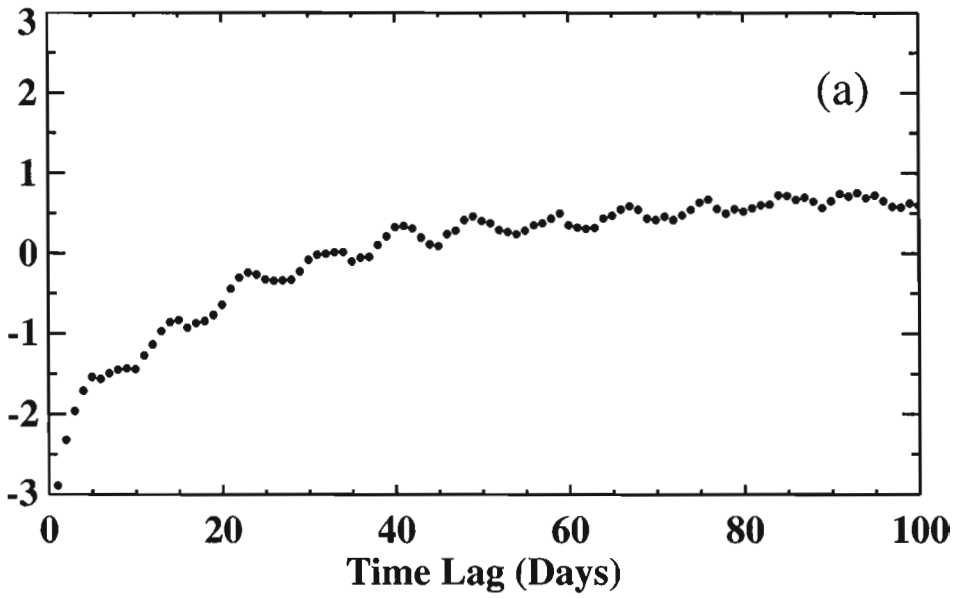

Figure 7.3 - *SST Semivariance Mode 1*
(a) Mode 1 EOF for semivariograms calculated from Pathfinder SST data.

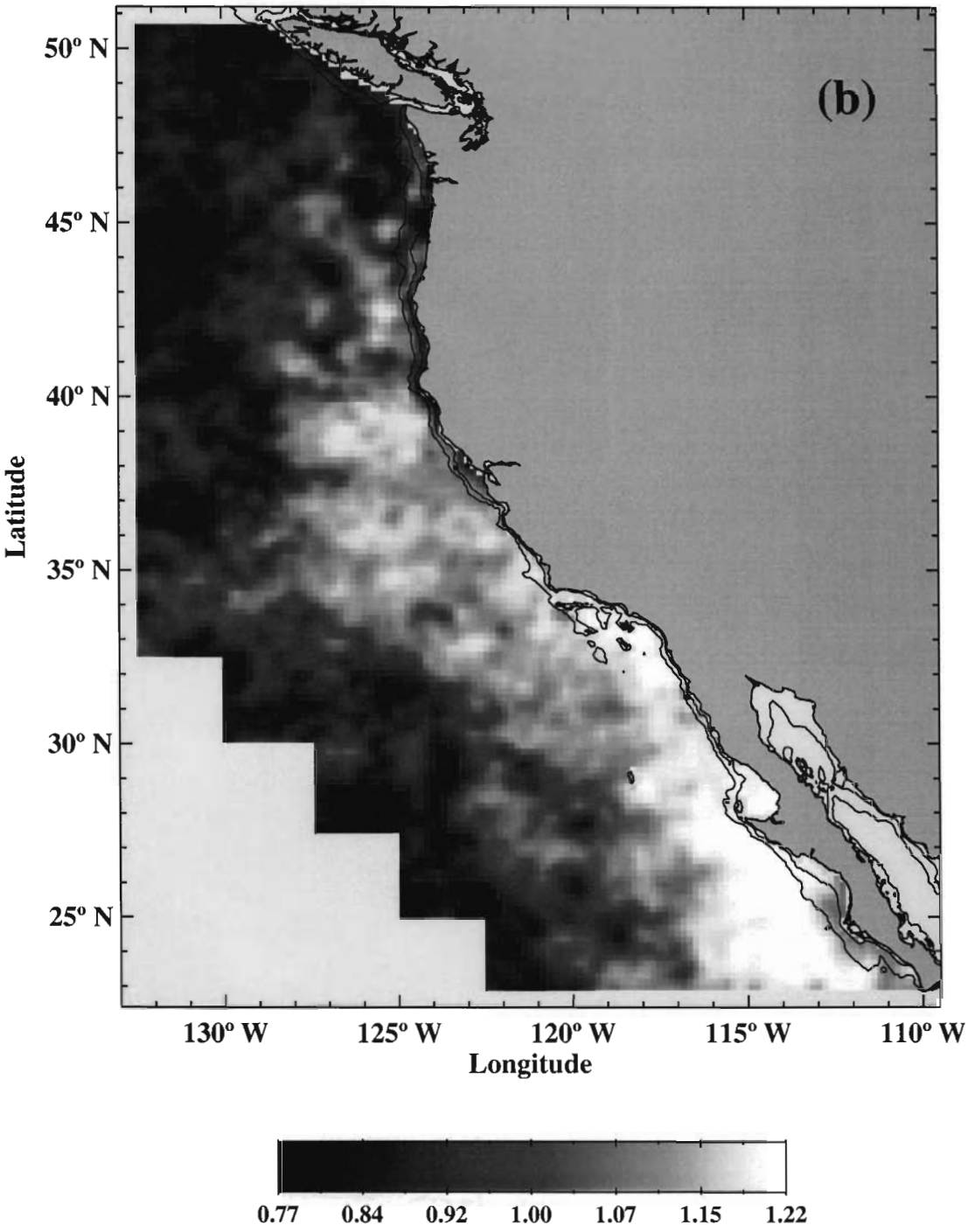

Figure 7.3 - *Continued*
(b) Mode 1 spatial amplitude function for semivariograms calculated from Pathfinder SST data. Data were smoothed with a 5 x 5 moving average.

analysis. We have attempted various means of defining decorrelation scales from individual semivariograms but have found no approach that does not substantially confuse the delineation of regional patterns of variability.

The mode 1 spatial amplitude function displayed in Figure 7.3b describes the relative contribution of the mode 1 EOF to the original empirical semivariogram calculated at each grid location. Semivariograms were individually standardized prior to analysis so that amplitude coefficients are dimensionless. Small values implying poor resemblance are due to either a structural dissimilarity between the mode 1 EOF and the actual semivariogram shape or increased scatter. The largest amplitudes lie within several hundred kilometers of the Baja Peninsula and Southern California. Nearshore amplitudes gradually decrease to the north but remain broadly elevated (>1.0) within a band extending some 400-500 km offshore, from the southern limit of our study region to ~40° N. North of Cape Mendocino, the width of this band tapers toward the coastline of central Oregon. Semivariograms calculated from locations more than ~500 km offshore or north of ~45° N are generally poorly represented by the mode 1 EOF.

The mode 2 EOF and spatial amplitude function describe the most coherent deviation from the dominant temporal structure defined by the mode 1 EOF. A positive contribution of the structure defined by the mode 2 EOF (Figure 7.4a) reduces semivariance at short lags (<15 days) and long lags (>60 days) and increases semivariance over a broad lag interval centered at ~40 days. An irregular band of positive mode 2 amplitude lies within ~200 km of the Pacific Northwest and extends southwestward from southern Oregon and northern California to the outer boundary of our study region (Figure 7.4b). Relative to the structure defined by the mode 1 EOF,

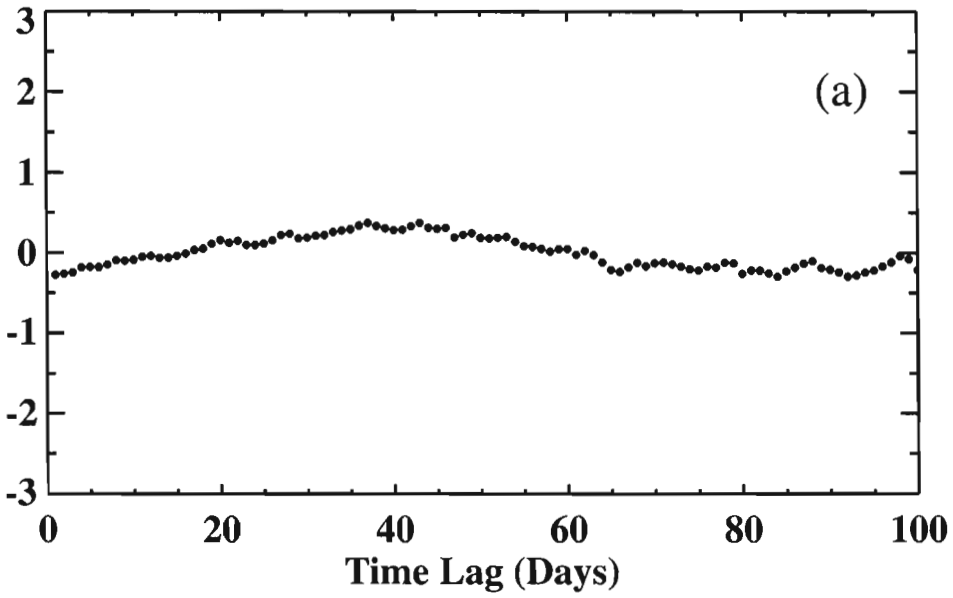

Figure 7.4 - *SST Semivariance Mode 2*
(a) Mode 2 EOF for semivariograms calculated from Pathfinder SST data.

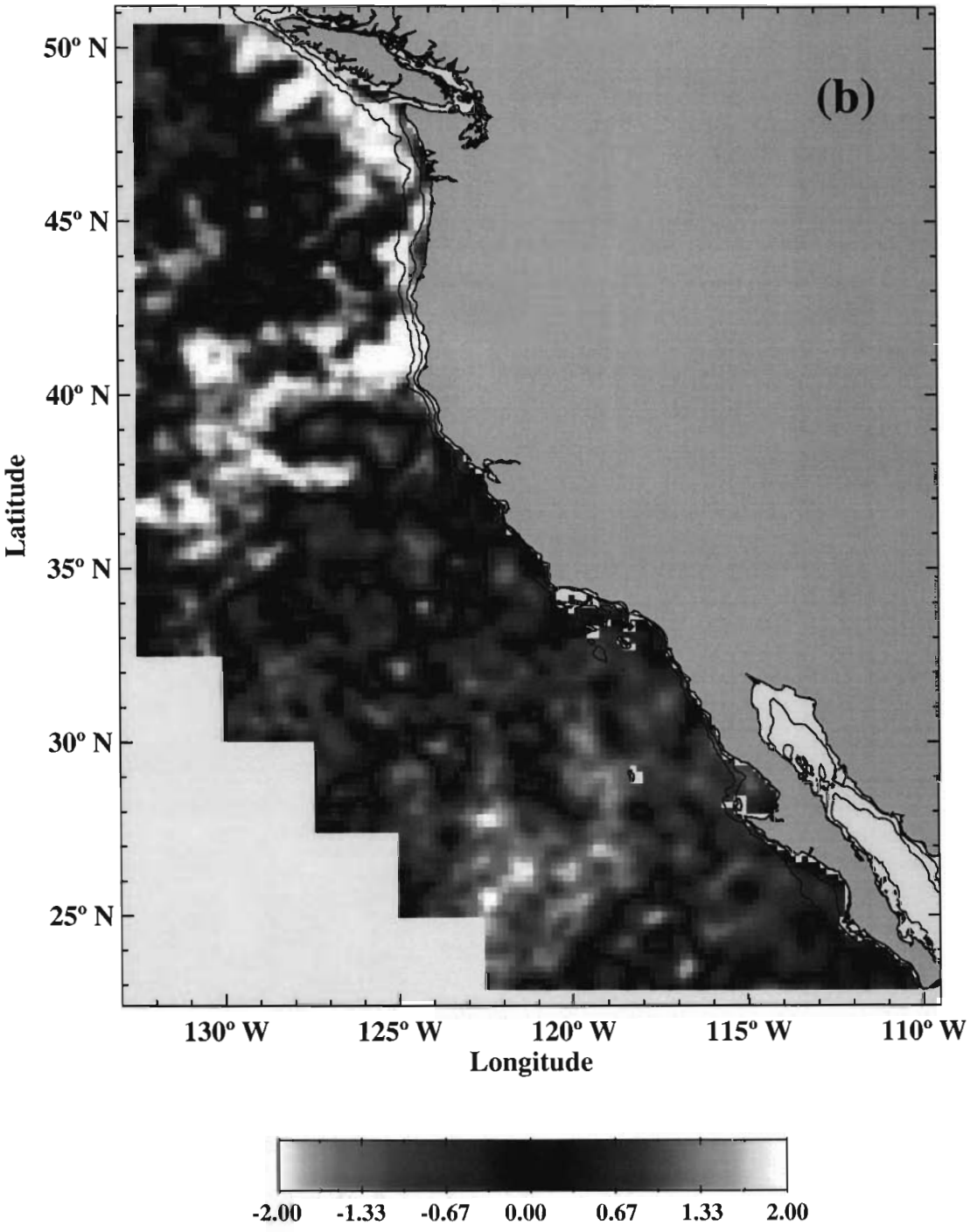

Figure 7.4 - *Continued*
(b) Mode 2 spatial amplitude function for semivariograms calculated from Pathfinder SST data. Data were smoothed with a 5 x 5 moving average.

SST semivariograms lying within this band of positive amplitude tend to show a sharper rise at shorter lags and a shift in peak semivariance to ~40 days, typically followed by a modest drop in semivariance at longer lags (e.g. Figure 7.1a and 7.1b). The generally weaker negative amplitudes found throughout most of the remainder of the region define an increase in semivariance at shorter and longer lags and a decrease at intermediate lags. Modes 3 and 4 (not shown) similarly describe variation over shorter and longer lags and, as is the case with weak negative mode 2 contributions, neither tends to bear a substantial or widespread influence on the dominant correlation structure of interest here.

The mode 1 spatial amplitude function of Figure 7.3b closely resembles patterns of near-surface eddy kinetic energy (EKE) obtained by satellite altimetry. Elevated levels of inshore EKE reflecting more vigorous time-varying geostrophic currents lie within 100 km of the coast north of Cape Blanco but extend some 400-600 km offshore to the south and are surrounded by the low EKE of the comparatively quiescent open ocean [Strub et al., 1997; Strub and James, 2000]. Wavenumber spectra calculated from multiyear time series of TOPEX cross-track velocity estimates show peak nearshore energy at wavelengths of ~300 km, a dominant wavelength associated with prominent meanders of the CC core and the distances between neighboring eddies of the same rotational sense [Kelly et al., 1998; Strub and James, 2000]. Similar calculations of frequency spectra from altimeter data are not available owing to aliased errors in modeled diurnal tides. Strub et al. [1997] do however, qualitatively estimate dominant periods of 100-150 days for vector velocity estimates obtained from altimeter data at a point ~400 km offshore of northern California (37.1° N, 127.5° W). Chereskin et al. [2000] estimate dominant periods of 120-180 days from frequency spectra calculated

from current meter data obtained at the same location, and Kelly et al. [1998] report peak energy at 120 days for currents measured at the base of the Ekman layer by an acoustic Doppler current profiler moored at that location. These dominant periods of velocity fluctuations loosely equate to the dominant scales of 50-60 days suggested by the mode 1 EOF (Figure 7.3a), although the mode 1 EOF itself offers no indication of periodic variations of SST. Nevertheless, the mode 1 EOF and spatial amplitude function taken together suggest that the dominant structure of residual SST time series is associated with the slow advection of prominent eddies and meanders past fixed locations.

The elevated EKE of the CCS is a composite effect of the seasonal evolution of mesoscale circulation initiated with the onset of strong and persistent upwelling winds and the intensification of coastal currents each spring. The potential and kinetic energy of the upwelling front and jet are progressively diverted into near-surface eddy energy through intrinsic instabilities, aided in part by coastal topography and by horizontal and vertical shear between the equatorward flow of the CC core and the poleward flow of the California Undercurrent [Batteen, 1997; Marchesiello et al., 2003]. Dominant wavelengths of ~300 km presumably follow from the dominant contribution of EKE through the baroclinic instability of coastal currents [Batteen, 1997; Marchesiello et al., 2003; Strub and James, 2000]. The seaward displacement and subsequent westward migration of the CC core and associated EKE maxima is well documented by altimetry [Kelly et al., 1998; Strub and James, 2000] and corroborated with multiyear, seasonally forced simulations [Batteen, 1997; Haney et al., 2001; Marchesiello et al., 2003]. The westward migration of EKE results from the westward propagation of individual eddies at speeds consistent with Rossby wave dynamics [Marchesiello et al., 2003] and

comparable to speeds of individual eddies observed off California and the Baja Peninsula [Brink et al., 2000; Huyer et al., 1998; Soto-Mardones et al., 2004]. Hormazabal et al. [2004] have recently provided a similar interpretation of near-surface velocity fluctuations within the Chilean upwelling system where a dominant period of 120 days appears to be determined by the slow westward migration of eddies and meanders generated near the coastline.

The dominant SST structure defined by propagating eddies and meanders likely arises from the distortion of large-scale surface temperature gradients by eddy stirring and from the displacement of eddy core waters from areas of eddy origin [Leeuwenburgh and Stammer, 2001; Lévy, 2003]. In the presence of a large-scale meridional SST gradient, a westward-propagating eddy in particular can produce a propagating SST anomaly due to geostrophic transports of opposite direction along the eddy flanks [Leeuwenburgh and Stammer, 2001]. Far from shore, however, prominent eddies are widely spaced [Chereskin et al., 2000]. Their infrequent and episodic passage over any given location may in part explain the lack of evidence of regular SST fluctuations within the mode 1 EOF despite the periodic behavior of near-surface currents as indicated by frequency spectra [Chereskin et al., 2000; Kelly et al., 1998; Strub and James, 2000]. Alternatively, SST need not reflect all prominent circulation features. Eddies centered at depth but apparent in surface currents (generated by the California Undercurrent) may show little or no surface temperature signature or even surface temperature anomalies of opposite sign to those of surface-intensified eddies of the same rotational direction [Chereskin et al., 2000; Huyer et al., 1998]. Further, storm-driven Ekman drift may

dissociate surface temperature structure from near-surface velocity fields, obscuring jets and eddies from view in SST imagery [Hüyer et al., 1998; Simpson et al., 1986].

The mode 1 spatial amplitude values discussed here are not a direct reflection of relative levels of EKE. Whereas measured and modeled near-surface EKE peaks off northern or central California [Marchesiello et al., 2003; Strub and James, 2000], this is obviously not the case for the amplitude estimates of Figure 7.3b. Mode 1 amplitudes are greatest where SST variability adheres to the structure described by the mode 1 EOF and where daily observations are most frequently available so that SST structure is most clearly defined. The general northward drop in nearshore amplitude values from Baja California to the Pacific Northwest reflects in part an increase in semivariogram scatter caused by a decrease in data availability (Figure 3.1a), and so too must the seaward decrease in amplitude. Offshore and to the north of California, the drop in amplitude estimates is further caused by a structural transition manifest as a greater influence of mode 2 (Figure 7.4b). This presumably follows not only from a greater role of the processes responsible for the mode 2 structure, but also from a lesser role of the eddy variability that we suggest is responsible for the mode 1 structure. Off California, the outer boundary of elevated mode 1 amplitudes at ~128° W does coincide with a marked drop in EKE which Haney et al. [2001] suggest is caused by the tendency for baroclinically unstable currents to become more barotropic in time, leading to a downward flux of EKE to the ocean interior. Farther to the south, the outer boundary of high amplitude and high EKE does not appear to coincide with any coherent change in SST structure. Although Strub and James [2000] suggest a region-wide transition to

shorter eddy spatial scales between 400 and 600 km from shore, such a transition is not reflected in (or resolved by) the SST time series discussed here.

We can quantify and compare the variance attributable to dominant SST structure and coherent deviations from that structure by reconstructing semivariograms according to mode 1 and modes 2-4, respectively (Figure 7.5). The product of the mode 1 EOF and the appropriate spatial amplitude estimate provides a reasonable approximation to the original empirical semivariogram calculated at most locations, once rescaled by the standard deviation and recombined with the mean of the original:

$$\tilde{\gamma}_m(h) = a_1(x_m)e_1(h) \; * \; sdev[\hat{\gamma}_m(h)] \; + \; \langle \hat{\gamma}_m(h) \rangle \tag{11}$$

The mode 1 reconstruction of semivariance defined by equation (8) is itself approximated by the exponential model defined as

$$\gamma(h) = \begin{cases} 0 & h = 0 \\ c_0 + (\sigma^2 - c_0)(1 - e^{-3h/r}) & h \neq 0 \end{cases} \tag{12}$$

where c_0, σ^2 and r are the nugget, sill and range parameters, respectively (Figure 7.5a). Where the mode 1 EOF is fully representative of semivariogram shape, sill and nugget parameters estimate the overall variance and unresolved variance of residual SST time series. The range r is implicitly defined as the lag at which semivariance has increased to ~95% of the asymptotic sill. Nugget, range and sill estimates were obtained at each grid location through a nonlinear least squares fit of the exponential model to each mode 1 reconstruction. Range estimates were typically about 65 days (equivalent to an e-folding scale of ~22 days) and, because model fits were applied to a single common semivariance structure, varied little in comparison to the nugget and sill. The contributions of the statistically significant higher modes were calculated as weighted

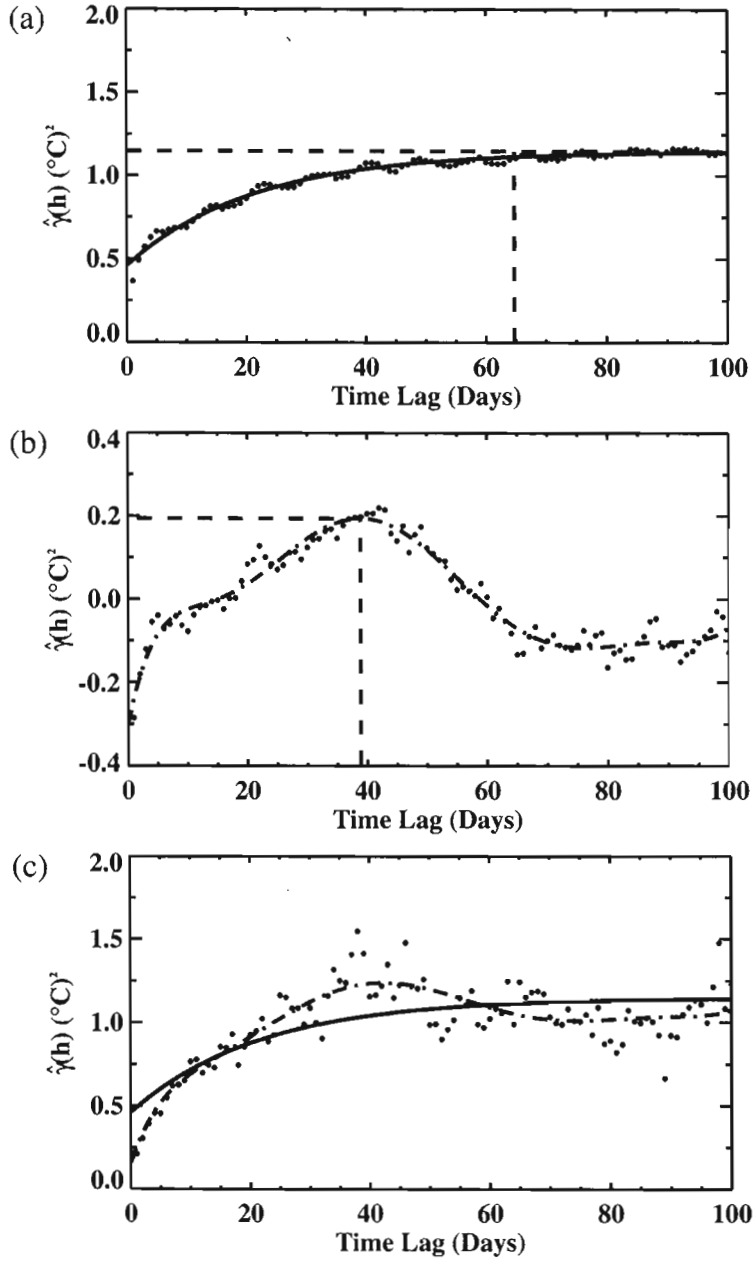

Figure 7.5 - *Example Reconstruction of SST Semivariance from Statistically Significant EOF Modes*

Reconstruction of semivariance estimated from Pathfinder SST data collected at 44.1° N, 124.8° W (location shown in Figure 1.1). (a) Mode 1 reconstruction. The solid red line is the exponential curve fit to the mode 1 structure. Vertical and horizontal dashed lines are the range and sill estimates, respectively. (b) Modes 2-4 reconstruction. The broken blue line is the polynomial curve fit to the modes 2-4 structure. Vertical and horizontal dashed lines identify the time scale and magnitude of the peak contribution of modes 2-4. (c) Empirical semivariogram (also shown in Figure 4.2d). The solid red line is the exponential curve fit to the mode 1 reconstruction as in (a). The broken blue line is the sum of the mode 1 exponential curve and the modes 2-4 polynomial shown in (b).

sums of the second, third and fourth EOFs, with weights provided by the corresponding spatial amplitude functions:

$$\tilde{\gamma}_m(h) = \sum_{k=2}^{4} a_k(x_m) e_k(h) \;\; * \;\; sdev[\hat{\gamma}_m(h)] \;\; + \;\; \langle \hat{\gamma}_m(h) \rangle \tag{13}$$

Reconstructions of semivariance based on modes 2-4 were modeled by eighth-order polynomials as a simple and flexible means of describing their more variable structural contributions (Figure 7.5b). The combined contributions of the mode 1 exponential and the high-mode polynomial generally provide an accurate representation of the form of the original empirical semivariogram (Figure 7.5c).

Discrete estimates of semivariance appear to approach a nonzero y-intercept (Figure 7.1), the so-called nugget variance introduced by measurement error and geophysical variation not adequately resolved by the daily sampling of SST. We can generally interpret the geophysical contribution as sub-diurnal variability of the area-integrated SST estimates. As can be seen in Figure 7.5c, the mode 1 nugget parameter estimate, equal to the y-intercept of the mode 1 exponential model, can substantially overestimate the actual nugget. By summing the mode 1 nugget parameter and the y-intercept of the high-mode polynomial, we can incorporate coherent structure acting over small lags to obtain a far more accurate estimate of nugget variance (e.g. Figure 7.5c). The geographic distribution of nugget estimates is shown in Figure 7.6. Elevated values (>0.20 $°C^2$) are centered over the slopes of the Pacific Northwest and central California, and very low values (<0.05 $°C^2$) lie within the inner SCB and just south of Cape Blanco and Punta Eugenia. Variations in estimation bias caused by variations in the representation of short time-scale structure by EOF modes likely contribute to these spatial patterns. Using empirical estimates of covariance, Walker and Wilkin [1998]

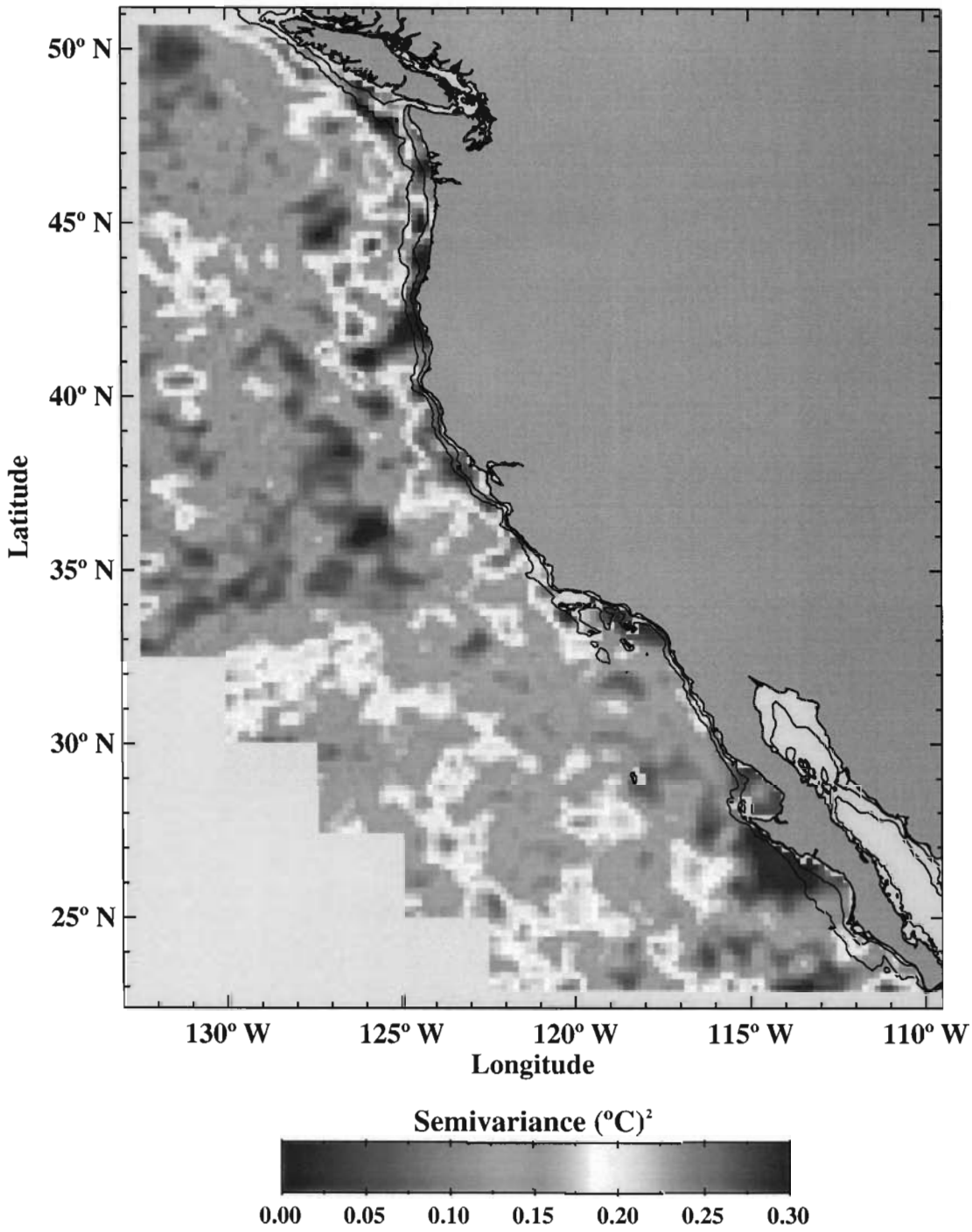

Figure 7.6 - *Unresolved SST Semivariance*
Unresolved SST semivariance calculated as the combined contribution of the nugget parameter estimate of the mode 1 exponential model and the y-intercept of the modes 2-4 polynomial model. Data were smoothed with a 5 x 5 moving average.

report a relatively constant level of unresolved variance of 0.15 °C^2 for Pathfinder SST time series over the varied oceanographic provinces of the Indo-Australian region, a value very near to the mean nugget estimate of 0.14 °C^2 for the CCS. A nugget variance of 0.14 °C^2 corresponds to an estimation error of 0.37 °C, well within the bounds of the accepted measurement error of 0.3-0.5 °C for Pathfinder data (NOAA/NASA AVHRR Oceans Pathfinder home page, http://podaac.jpl.nasa.gov/sst/).

Figure 7.7a displays the sill estimates derived from the exponential model fit to mode 1 semivariogram reconstructions. High sill estimates are generally confined to two areas; the first extending ~200 km offshore of southern Oregon and northern California and the second extending seaward of the southern Baja Peninsula to ~116 °W. These are not only areas of intense jet and eddy activity [e.g. Strub et al., 1997; Espinosa-Carreon et al., 2004] but are also areas of strong seasonal heating gradients (Figures 5.1b and 5.1c), where we would expect mesoscale circulation to induce the strongest SST variability. As a fraction of total variance, the greatest contributions over intraseasonal scales (exceeding 40% of total variability) are found near upwelling centers south of Cape Blanco and Cape Mendocino (Figure 7.7b). Dominant intraseasonal variation otherwise accounts for about 25% of total variability from southern Oregon to Point Conception and along the outer boundary of the SCB. Save for the immediate vicinity of Punta Eugenia, intraseasonal contributions to total variance are considerably lower along the Baja Peninsula, within the inner Bight and along the Pacific Northwest, where seasonal variations are comparatively stronger (Figures 5.1b-d).

Figure 7.8 shows the magnitude of the most prominent peak of the high-mode polynomial models (where peak semivariance occurs at a time lag shorter than the

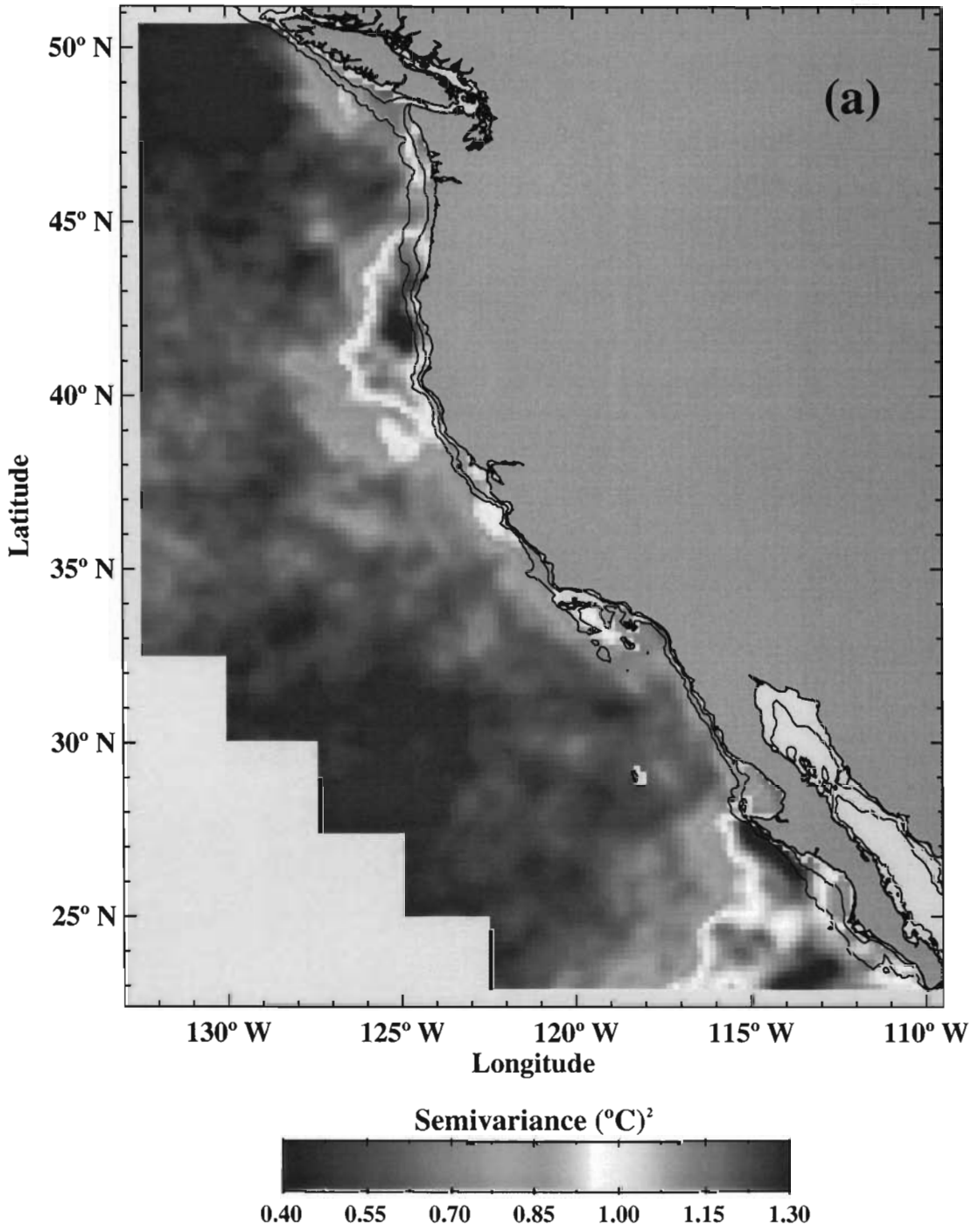

Figure 7.7 - *Semivariance Contributed by SST Mode 1*
(a) SST semivariance contributed by the mode 1 semivariogram structure, calculated as the sill of the mode 1 exponential model. Data were smoothed with a 5 x 5 moving average.

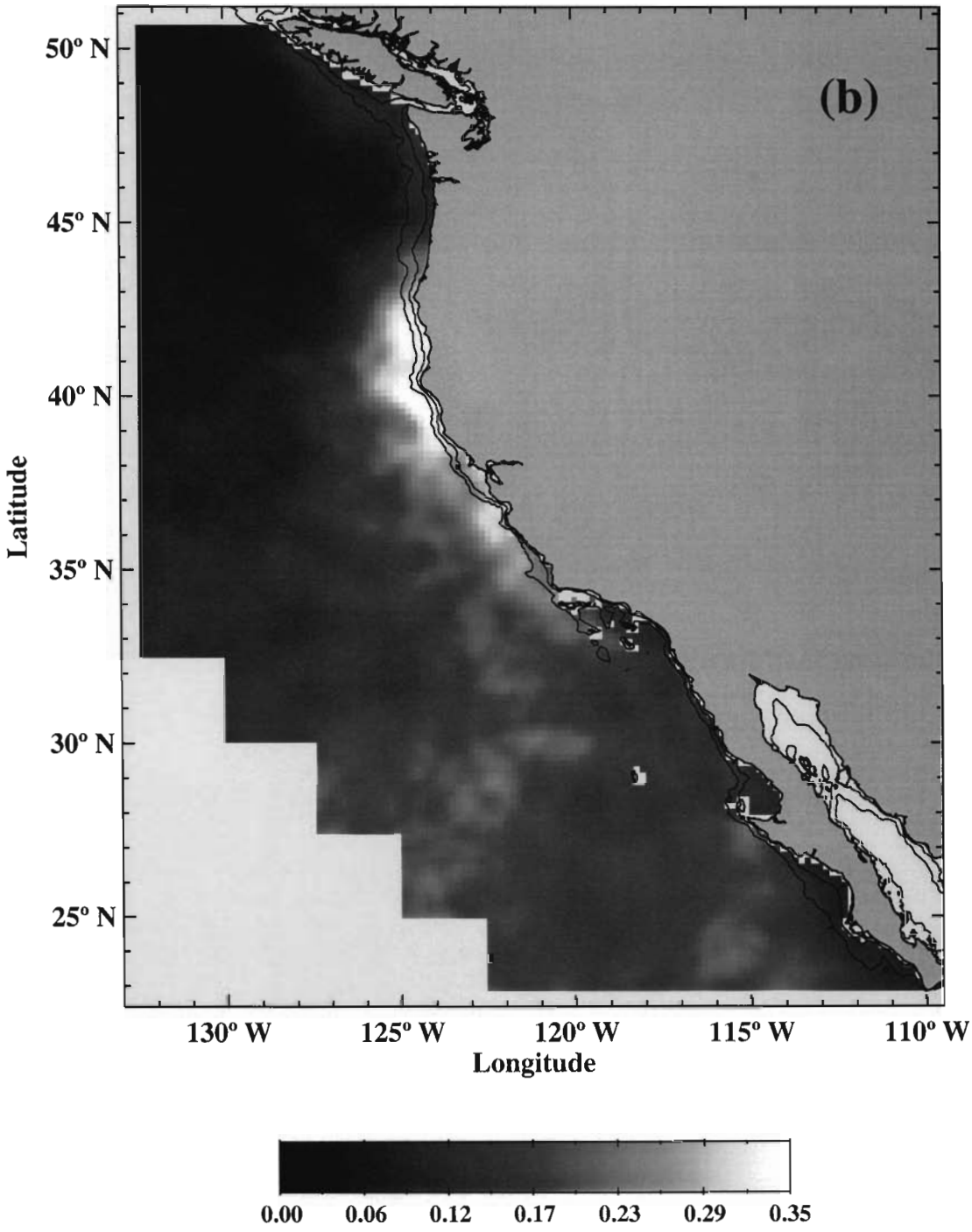

Figure 7.7 - *Continued*
(b) Fraction of total SST variance contributed by the mode 1 semivariogram structure. Total variance was approximated as the sum of variance contributed by the mean seasonal cycle, dominant intraseasonal variability described by the mode 1 structure, and interannual variability. Data were smoothed with a 5 x 5 moving average.

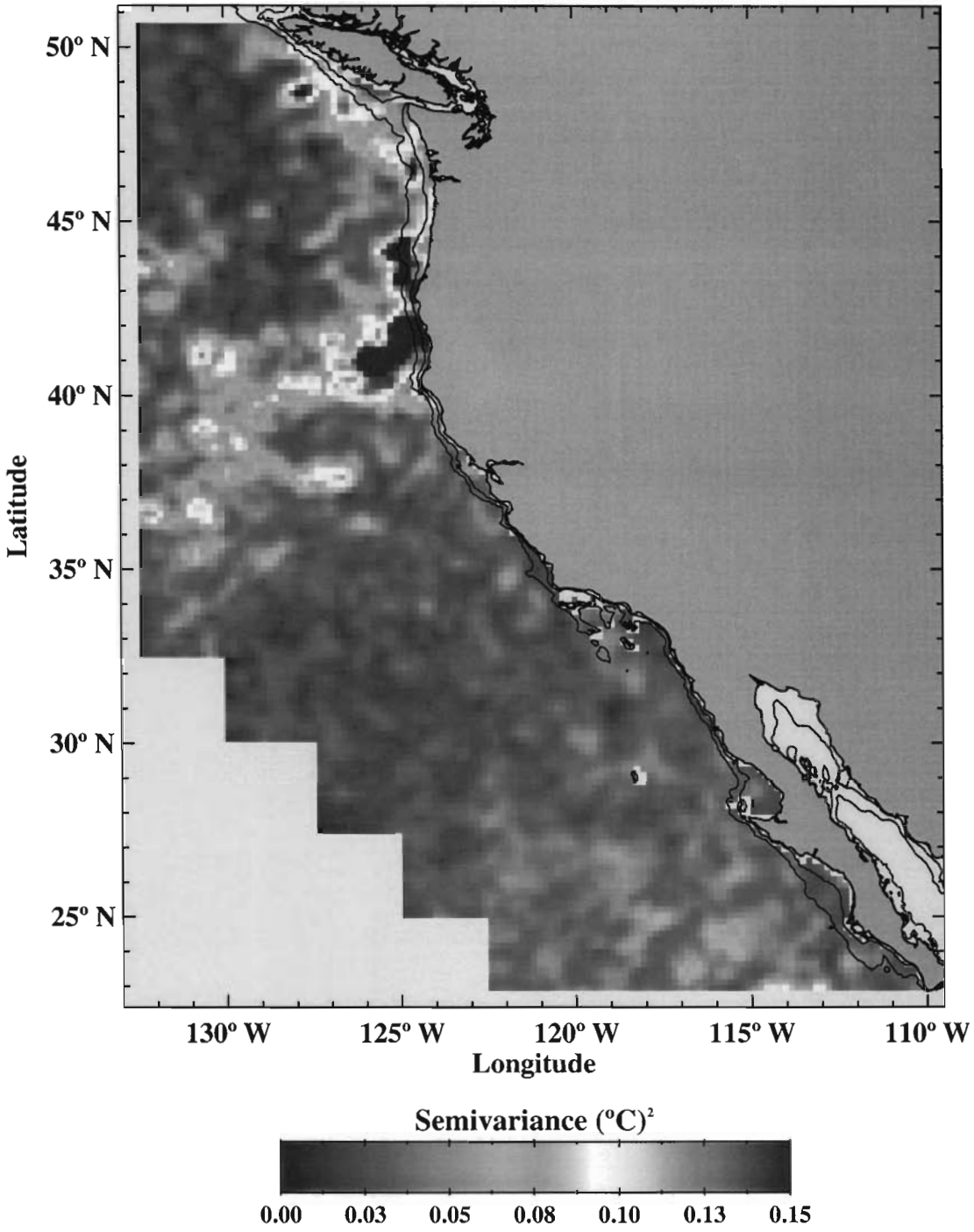

Figure 7.8 - *Semivariance Introduced by SST Modes 2-4*
SST semivariance introduced by modes 2-4, estimated from the largest positive peak of the modes 2-4 semivariogram reconstruction. Data were smoothed with a 5 x 5 moving average.

mode 1 range of ~65 days). We use the magnitude of this high-mode peak as a measure of the relative contributions of modes 2-4 and the degree to which temporal structure is shifted to characteristic scales shorter than that of the dominant mode 1 structure. As seen in Figure 7.8, the greatest high-mode contributions (>0.15 $°C^2$) lie along southern Oregon and northern California and extend several hundred kilometers offshore between Cape Blanco and Cape Mendocino. Weaker and more diffuse bands of elevated semivariance extend along the coast to the north and offshore to the southwest in a pattern very similar to that of the strong positive mode 2 amplitudes shown in Figure 7.4b. Peak high-mode semivariance values exceeding 0.8 $°C^2$ (Figure 7.8) occur on average at a time lag of 39 days, confirming the dominance of mode 2 in defining structural deviations from the mode 1 EOF. Statistically significant higher modes introduce very little structure throughout the remainder of the region. While more localized variations in semivariogram shape do occur (e.g. Figure 7.1g), EOF decomposition isolates coherent structure occurring over large areas.

The amount of semivariance introduced by modes 2-4 is generally quite small relative to that contributed by the dominant mode 1 structure (compare Figures 7.7a and 7.8). Between Cape Blanco and Cape Mendocino, the high-mode contribution is strong enough to cause a clear shift in peak semivariance to lags near 40 days (e.g. Figures 7.1a and 7.5). Even at these locations, the mode 1 sill appears to remain a reasonable approximation to the overall variance of dominant intraseasonal scales (e.g. Figure 7.5c). A discrete peak at 40 days suggests some degree of regular variation of SST at periods of ~80 days. Such an interpretation, however, presupposes a level of statistical stationarity that may not be realistic. A few dominant and regularly spaced events of the appropriate

40-day duration may be sufficient to produce a local peak in semivariance [Radeloff et al., 2000]. Here we can conclude only that a coherent and widespread introduction of variance at a time scale of ~40 days occurs across the northern CCS.

It is difficult to offer any substantive physical explanation for the 40-day time scales contributed by mode 2. Cape Mendocino itself tends to act as a climatological boundary between the sustained influence of the North Pacific high to the south and the frequent passage of storm systems to the north [Dorman and Winant, 1995]. Even during summer months when high pressure often extends into the Pacific Northwest, temporal patterns of wind forcing have been observed to differ to the north and south of Cape Mendocino or Point Arena [Abbott and Barksdale, 1991; Halliwell and Allen, 1987; Kelly, 1985; Largier et al., 1993; Winant et al., 1987], as have patterns of SST [Kelly, 1985]. Edwards et al. [2002] relate spatial patterns of surface winds obtained through microwave imaging to buoy-measured atmospheric pressure gradients during June 1994 and 1996. In the prevailing case where the background pressure gradient pointed downcoast, northeasterly winds accelerated as they rounded Cape Mendocino, forming a high-speed region extending several hundred kilometers seaward of the California coast. When the background pressure gradient pointed upcoast and geostrophic winds had an onshore component, flow separated at Cape Mendocino and the highest speeds were found to the north and offshore of the Cape, in the northwest corner of our study region where high-mode contributions are weak. Systematic variations in regional atmospheric pressure gradients may thereby impose variations in organized patterns of wind forcing to either side of the high-variance band extending offshore of southern Oregon and northern California in Figure 7.8. It is not clear, however, whether such variations may force a

substantial signal in SST at the time scale of 40 days. A 3-month quasi-periodic fluctuation in the Bakun upwelling index (a pressure-derived measure of inshore wind forcing) is sometimes evident off the northern U.S. west coast [e.g. Lynn et al., 1998; Venrick et al., 2003]. We could also note that the pattern of elevated high-mode contributions of Figure 7.8 is very similar to that of the February/August semiannual phase estimates of Figure 5.1f, suggesting a nonstationary signal modulated by the seasons. At any rate, it would appear that northern California lies at a transition in SST forcing between the dominant eddy variability of the CC to the south and the vigorous atmospheric forcing of higher latitudes, where strong Ekman drift or surface heat exchange likely confound the temporal signature of propagating features originating at the coast [Leeuwenburgh and Stammer, 2001].

The long time scales discussed thus far are seemingly inconsistent with the rapid evolution of surface patterns expected of coastal upwelling systems. Denman and Abbott [1994] used spectral statistics to calculate temporal decorrelation scales from 1 km AVHRR imagery according to discrete spatial wavelengths of up to 100 km off northern California. Decorrelation scales varied with spatial scale and with proximity to areas of active upwelling but were generally found to be no more than about 10 days. These results were, however, derived from select cloud-free late spring or early summer imagery and were very likely biased toward high-wind, strong-upwelling conditions typically associated with clear skies [Edwards et al., 2002; Kelly, 1985]. A meaningful comparison between our results and theirs is complicated because our statistics integrate variability through all seasons and wind conditions. The temporal statistics calculated by Denman and Abbott [1994] were also specific to SST patterns of relatively short spatial

scales. Temporal structure estimated from empirical semivariograms includes variability acting over much larger scales, and EOF analysis of semivariogram structure favors the description of variability manifest over large areas.

Largier et al. [1993] describe an energetic band of current and SST fluctuations over the northern California shelf and slope at frequencies lower than those of dominant wind forcing. Variability of alongshore currents over 10-45 day periods was found to be disproportionately high relative to alongshore winds, and the coherence between the two was correspondingly low. Current and SST fluctuations in this instance were attributed to mesoscale eddy variability in adjacent oceanic waters. Flow associated with impinging eddies was occasionally observed to dominate the local upwelling circulation for more than a month as warmer oceanic water flooded the inner shelf [Largier et al., 1993]. Alternatively, the seaward displacement of eddies and meanders can provoke a realignment of local inshore currents, thereby altering inshore SST patterns [Huyer et al., 1991; Lagerloef, 1992]. Eddy-induced current fluctuations over the shelf and slope, however, are typically dominated by periods on the order of 10-50 days corresponding to decorrelation scales of 5-25 days [Chereskin et al., 2000; Denman and Freeland, 1985; Hickey, 1998; Largier et al., 1993]. Although there is no *a priori* reason to expect patterns of surface temperature variability to adhere to patterns of surface current fluctuations, these scales are similar to those obtained from multiyear time series of *in situ* SST. Breaker and Lewis [1988] identified dominant 40-50 day quasi-periodic fluctuations (corresponding to decorrelation scales of 20-25 days) in multiyear time series of *in situ* SST collected off central California. In this case fluctuations were coherent with alongshore winds at a phase lag consistent with the modulation of SST by

coastal upwelling, although Breaker et al. [2001] later showed that dominant SST variability at this location was not always related to wind forcing. Dorman and Winant [1995] found significant coherence between SST and alongshore winds over an energetic band of 5-50 day periods in buoy data collected along the U.S. west coast. Phase lags were consistent with a wind-forced SST response.

We have calculated semivariograms from time series of *in situ* SST provided by the National Data Buoy Center at some of the same U.S. west coast locations discussed by Dorman and Winant [1995]. Hourly buoy data was sampled at 1400 hr, the nominal acquisition time of the AVHRR data used to construct the Pathfinder time series discussed here. As with satellite data, seasonal and interannual variability was removed prior to the calculation of semivariograms. Long data gaps were present in buoy time series at most locations. We have therefore selected only relatively complete time series. We then subsampled collocated Pathfinder time series according to buoy data availability to produce the most sensible buoy-satellite data comparisons. Figures 7.9a and 7.9b display empirical semivariograms calculated from buoy and satellite time series at two representative locations shown in Figure 1.1. It seems reasonable to expect a shift to shorter scales of variability in buoy time series owing to the small spatial extent and short temporal persistence of coastal currents. Such a shift in variance structure is evident off Point Arguello, where buoy semivariance increases more rapidly over time lags of ~5-20 days than does semivariance calculated from collocated satellite data (Figure 7.9b). This result is not consistent across buoy locations and is not, for example, evident in the buoy semivariogram calculated off Point Arena (Figure 7.9a). Significant differences between the temporal structure of the area-averaged Pathfinder data and point data of buoy SST

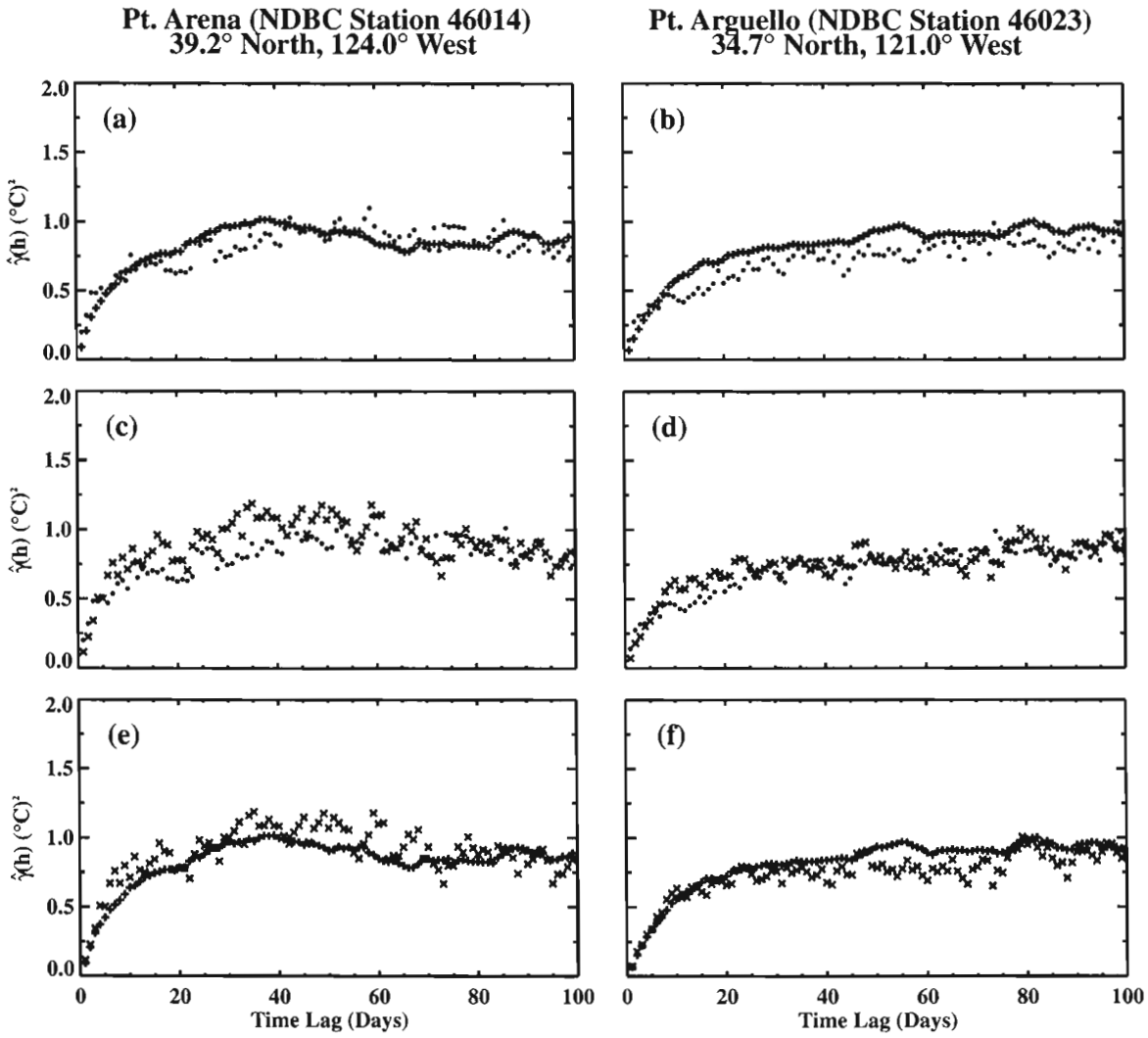

Figure 7.9 - *Empirical Semivariograms Calculated from In Situ and Satellite-Derived SST* Empirical semivariograms calculated from daily SST time series data collected by NDBC buoys off the California coast (locations shown in Figure 1.1) and assembled from Pathfinder data aggregated over an 18 km sampling box centered over the buoy locations (black dots). Buoy semivariance estimates are calculated from full time series (red +) or from time series sampled according to the availability of Pathfinder observations (blue x).

appear to be location-dependent. Where present in satellite-derived SST, strong variability at time scales of 25 days or less is not widespread and does not represent a regionally dominant pattern of variation.

We can inquire as to whether the temporal sampling characteristics of the satellite-derived SST data are responsible for any structure evident in empirical semivariograms. To this end, we have calculated indicator semivariograms defined as

$$\hat{\gamma}_I(h) = \frac{1}{2n(h)} \sum_{n(h)} [ind(t_i) - ind(t_i + h)]^2 \tag{14}$$

where each indicator datum ind(t_i) is set to 1 if an observation is available at time t_i and 0 if not. The indicator semivariogram defined by equation (11) is a scale-dependent measure of the connectivity between two classes defined by the presence or absence of observations. A smaller value for a given lag implies a greater degree of connectivity between days for which an observation is available and days for which no observation is available. A larger value for a given lag implies a lesser degree of connectivity, and hence a tendency for observations to be either consistently present or consistently absent on days separated by that particular lag interval. Figure 7.10 shows the indicator semivariogram calculated from a Pathfinder SST time series collected over the upper slope of southern Baja California (the empirical semivariogram calculated at this location is shown in Figure 7.1g). Indicator semivariance oscillates with a period of 8-10 days, suggesting a tendency for observations to be systematically grouped according to an 8-10 day sampling interval. Time series across much of the region possess the same periodic sampling structure. The strength of this periodicity appears to vary according to latitude and overall data availability, peaking off Punta Eugenia but virtually absent in the northern CCS. Walker and Wilkin [1998] identified a similar sampling structure in

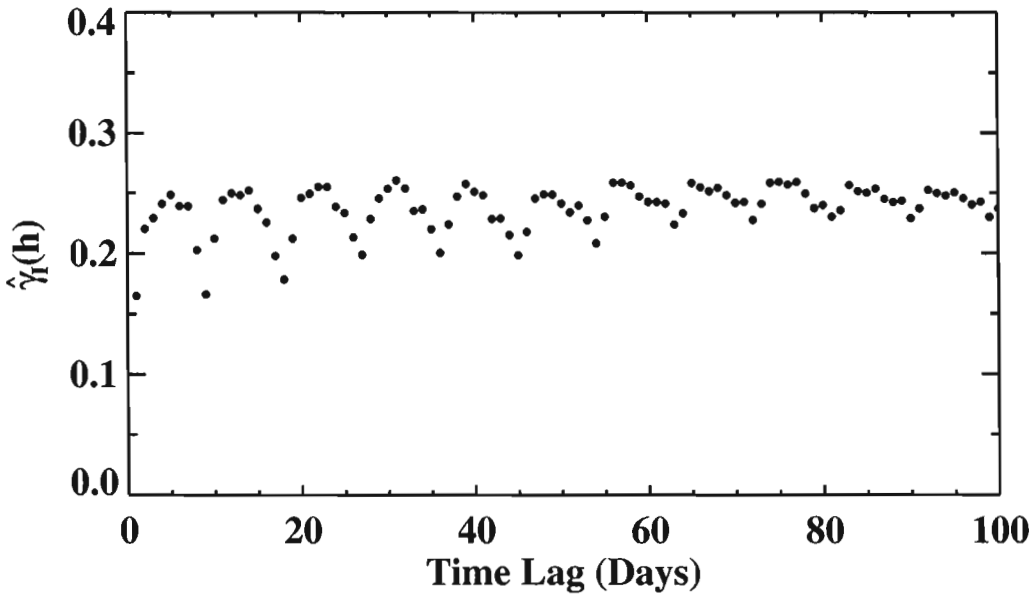

Figure 7.10 - *Pathfinder SST Presence / Absence Indicator Semivariogram*
Presence / absence indicator semivariogram calculated from Pathfinder SST time series collected at 26.0° N, 112.5° W (location shown in Figure 1.1).

Pathfinder data collected across the Indo-Australian region and attribute its presence to the orbital characteristics of the NOAA satellites carrying the AVHRR instrument.

Where sampling fluctuations are strong at lower latitudes, they appear to introduce 8-10 day fluctuations in empirical SST semivariograms (e.g. Figure 7.1g). These fluctuations are evidently strong enough and prevalent enough to have been captured by the mode 1 EOF (Figure 7.3a). More generally, the impact of sampling oscillations varies in more complicated ways according to the variance structure of the SST signal itself. High-frequency SST variability may be poorly resolved or aliased into longer time scales, potentially altering the shape of empirical semivariograms. We can further assess the impact of sampling structure on the calculation of SST semivariograms off the U.S. west coast by sampling NDBC residual time series according to the days for which Pathfinder observations are available. Although weaker than off Baja, sampling structure is capable of affecting the shape of empirical buoy semivariograms at short lags. At both Point Arena and Point Arguello, semivariograms calculated from sampled buoy time series show a somewhat sharper break in slope at 8-10 days compared to semivariograms calculated from the full buoy time series (Figures 7.9c-f). The impact of sampling oscillations on the shape of buoy semivariograms, however, is location-dependent, typically slight, and generally most pronounced either at short time lags or at lags exceeding the apparent decorrelation scale of the SST data. Although non-random patterns of data availability may affect relatively subtle features of empirical semivariograms, EOF analysis of semivariance appears to provide a conservative and reliable means of defining widespread patterns of intraseasonal variability.

7.2 Chlorophyll

The mode 1 EOF calculated from chlorophyll semivariograms (explaining 48.3% of semivariogram structure) follows the same general form as that of SST, a negative exponential curve approaching an upper bound at time lags of 50-60 days (Figure 7.11a). The chlorophyll mode 1 EOF, however, increases smoothly with no 8-10 day oscillation as is evident in the mode 1 EOF calculated from Pathfinder SST data. Coherent high frequency oscillations were similarly absent from presence/absence indicator semivariograms and were less apparent in empirical semivariograms calculated from residual SeaWiFS time series (e.g. Figure 7.1g). Mode 1 amplitude functions calculated from SST and chlorophyll show prominent commonalities as well as marked differences. As with SST, chlorophyll amplitude estimates are generally elevated within 400-500 km of the coastline from northern California to the southern boundary of our study region, with maximum amplitudes off southern Baja. Elevated chlorophyll amplitudes (>1.0) extend some 100 km further offshore of California than do elevated SST amplitudes. Chlorophyll semivariograms calculated at locations far from shore are very poorly represented by the mode 1 structure, and the transition from high inshore amplitudes to low offshore amplitudes is much sharper than that observed of SST. Elevated amplitude estimates extend into the northernmost portion of our study region, where SST amplitudes are relatively low. Also unlike SST, a narrow inshore band of generally low amplitude extends from Vancouver Island south to Point Conception and along the outer boundary of the SCB.

The mode 2 EOF and amplitude function jointly define the most coherent deviation from the dominant mode 1 structure (explaining 4.0% of semivariogram

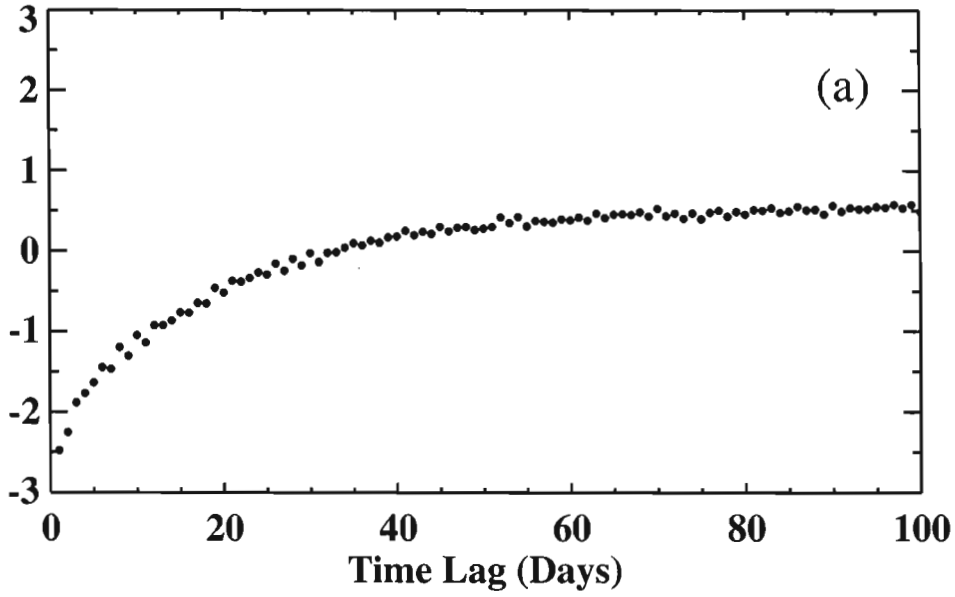

Figure 7.11 - *Chlorophyll Semivariance Mode 1*
(a) Mode 1 EOF for semivariograms calculated from ln-transformed SeaWiFS chlorophyll data.

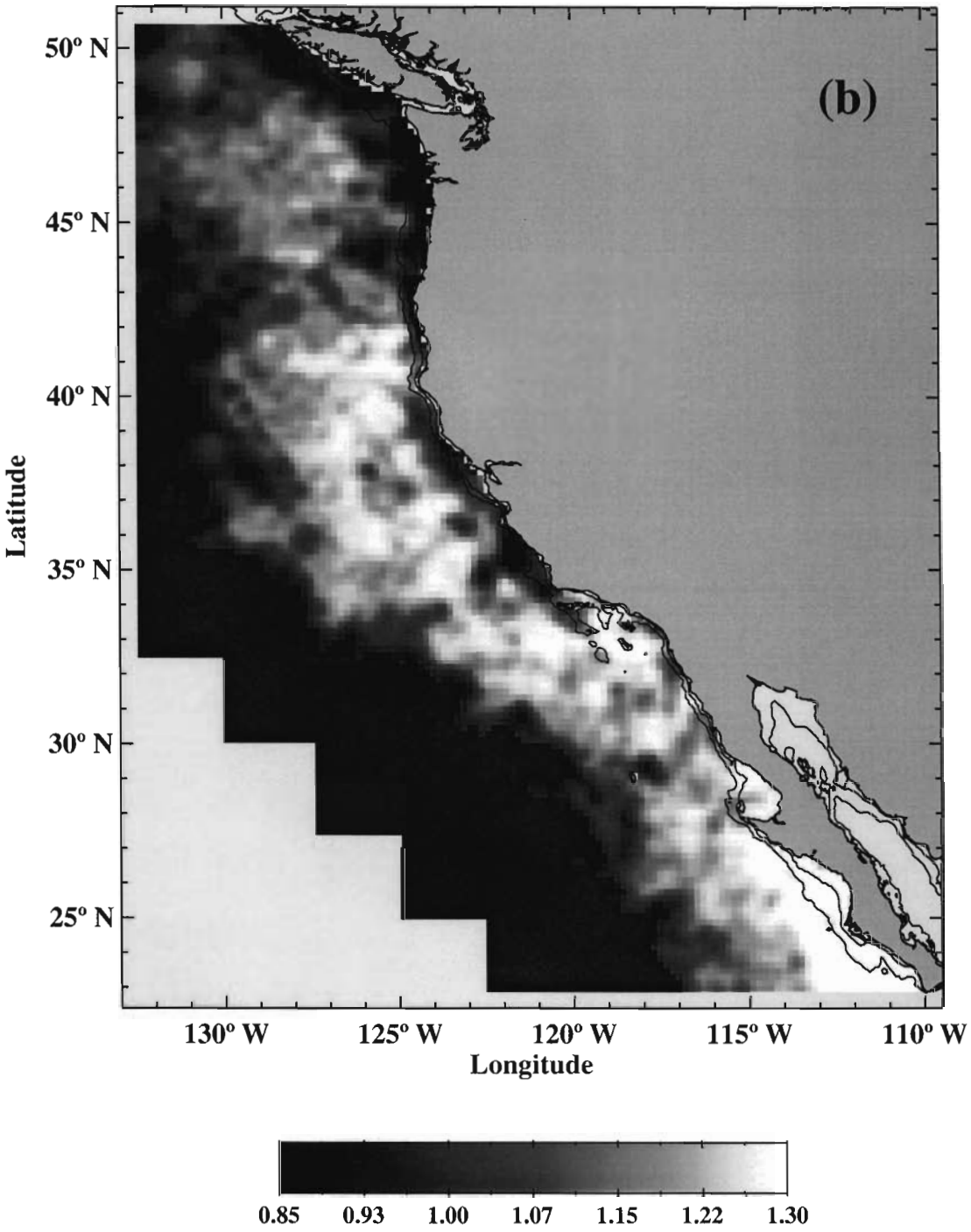

Figure 7.11 - *Continued*
(b) Mode 1 spatial amplitude function for semivariograms calculated from ln-transformed SeaWiFS chlorophyll data. Data were smoothed with a 5 x 5 moving average.

structure). The mode 2 EOF is very similar to that of SST, gradually increasing to a broad peak centered at ~40 days (Figure 7.12a). Strong positive amplitude estimates are concentrated within 100-200 km of North-central California and the Pacific Northwest (Figure 7.12b). As with SST, strong positive mode 2 amplitudes capture the most prominent structural contribution beyond that of mode 1, introducing a sharper rise in semivariance at short lags, a shift in peak semivariance toward ~40 days and a modest drop in semivariance thereafter (e.g. Figure 7.1a). Modes 3 and 4 (not shown) are qualitatively similar to mode 2, with EOFs describing relatively regular oscillations of semivariance with peak contributions at 20-30 days. The strongest positive amplitudes are similarly concentrated near to shore. Mode 3 contributions in particular shift peak semivariance toward 25-30 days within ~100 km of the California coast south of Monterey Bay and along the outer boundary of the SCB (e.g. Figures 7.1e and 7.1f). Although modes 3 and 4 are locally important, their contributions are far less spatially coherent than that of mode 2, consistent with their marginal statistical significance (Figure 7.2b).

As previously described, we calculated the variance contributed by the dominant mode 1 structure and coherent deviations from that structure by first reconstructing semivariance from mode 1 and modes 2-4 (according to equations 8 and 10, respectively). An exponential model parameterized by nugget, range and sill (equation 9) was fit to each mode 1 reconstruction. Range estimates were typically about 56 days and varied little. Nugget and sill parameters provide estimates of the unresolved and overall variance of residual ln-transformed chlorophyll time series where the mode 1 EOF reasonably reflects the structure of empirical semivariograms. A polynomial model was

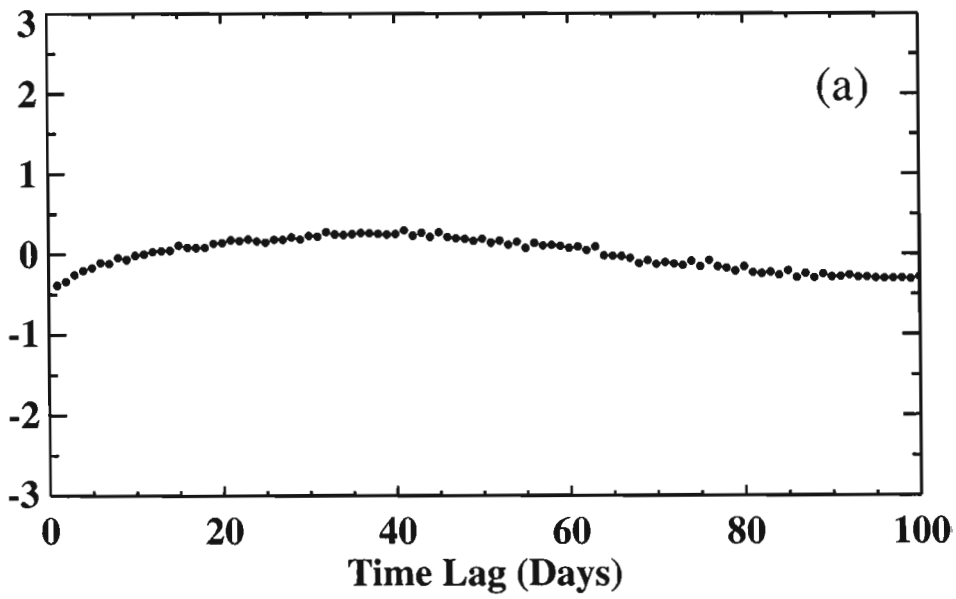

Figure 7.12 - *Chlorophyll Semivariance Mode 2*
(a) Mode 2 EOF for semivariograms calculated from ln-transformed SeaWiFS chlorophyll data.

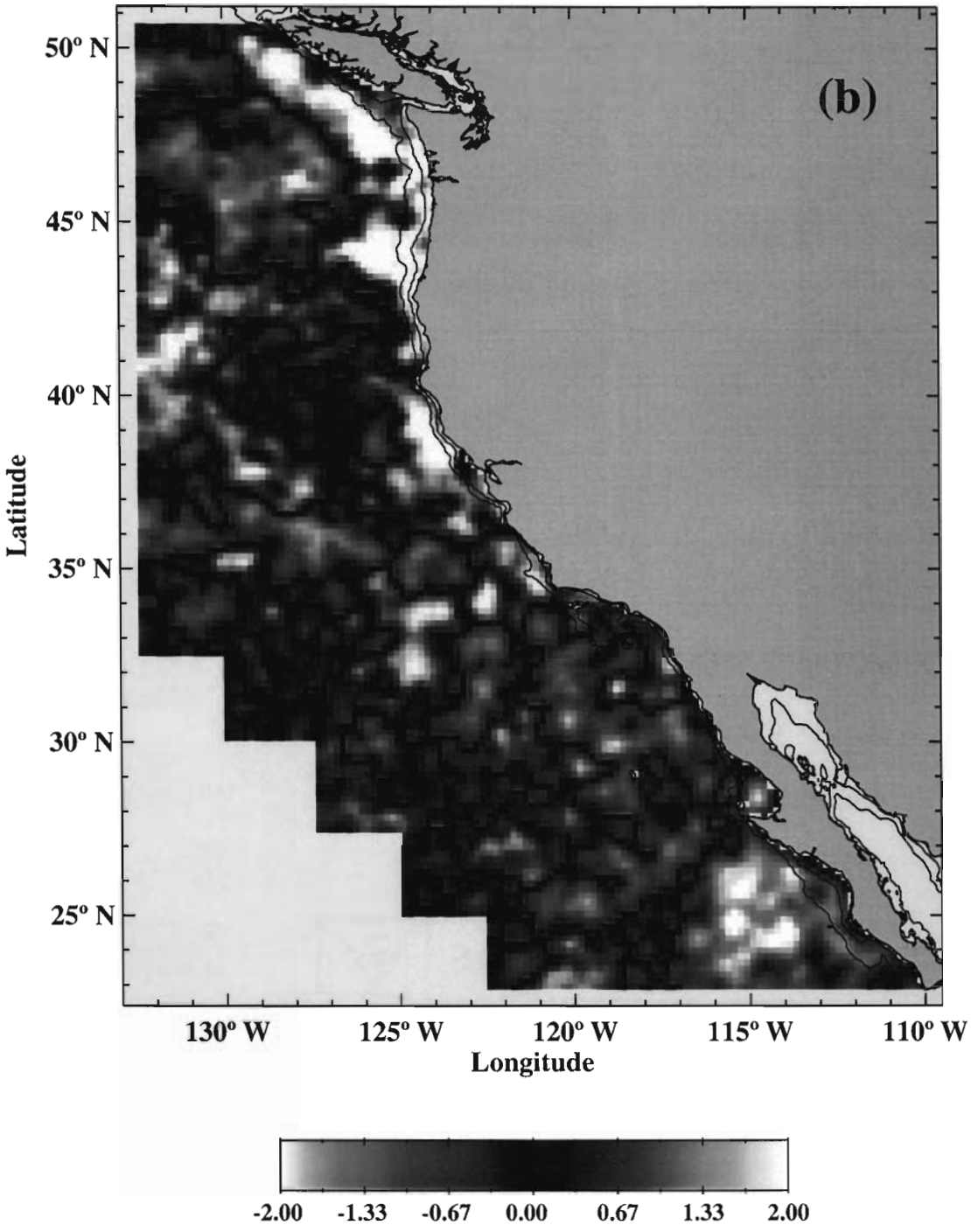

Figure 7.12 - *Continued*
(b) Mode 2 spatial amplitude function for semivariograms calculated from ln-transformed SeaWiFS chlorophyll data. Data were smoothed with a 5 x 5 moving average.

fit to each high-mode reconstruction and the magnitude of the most prominent peak of each polynomial was used as a measure of the degree to which variance structure is shifted toward characteristic scales shorter than the mode 1 range. Reasonably accurate estimates of nugget variance were obtained by summing the mode 1 nugget parameter estimates and the y-intercepts of high-mode polynomials. Because chlorophyll semivariograms were calculated from ln-transformed data, nugget, sill and peak high-mode semivariance estimates were rescaled into the original data units prior to their interpretation (Appendix B). Estimates of dominant time scales were little affected by this rescaling of semivariance.

Doney et al. [2003] describe global patterns of SeaWiFS spatial structure determined through a semivariogram analysis somewhat analogous to ours. Nugget variance resulted from the combined contributions of measurement error and submesoscale spatial structure with dimensions on the order of 10 km, and varied in proportion to mean chlorophyll concentrations where mean concentrations exceeded ~0.2 mg m^{-3} [Doney et al., 2003]. Nugget variance estimated from residual time series of SeaWiFS data described here result from measurement error and from unresolved temporal variability of chlorophyll concentrations aggregated over 18 km sampling units. The pattern of nugget variance shown in Figure 7.13 generally adheres to the description of Doney et al. [2003] in that unresolved variability, whether rooted in measurement error or submesoscale geophysical variation, follows a geographic distribution very similar to that of annual mean chlorophyll (Figure 5.2a). Nugget values are disproportionately high over the wide shelves of the Pacific Northwest and outside of San Francisco Bay (37.7° N), where suspended sediments and dissolved organic matter of

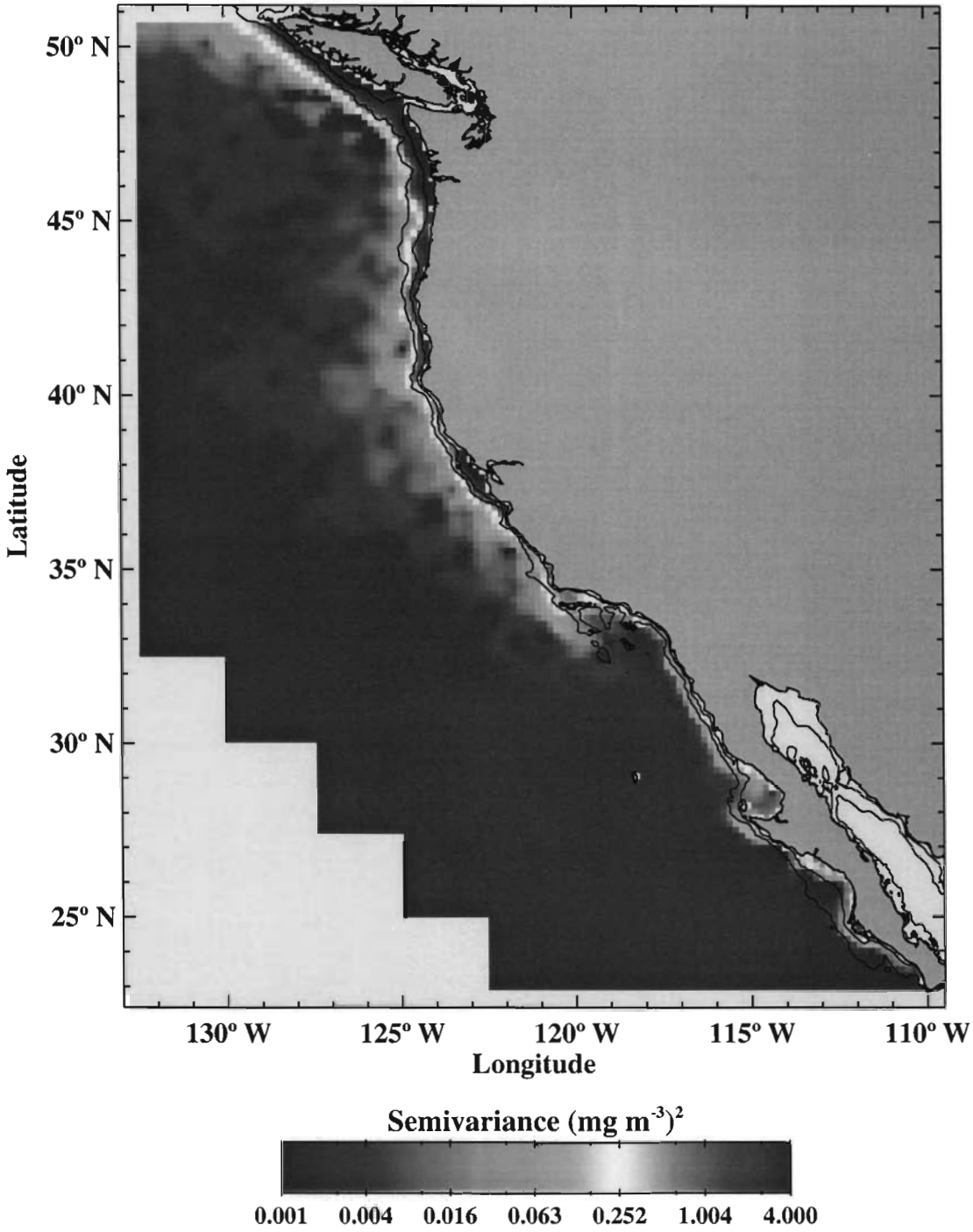

Figure 7.13 - *Unresolved Chlorophyll Semivariance*
Unresolved chlorophyll semivariance calculated as the combined contribution of the nugget parameter estimate of the mode 1 exponential model and the y-intercept of the modes 2-4 polynomial model. Data were smoothed with a 5 x 5 moving average.

terrigenous origin likely contribute error to estimates of chlorophyll concentrations, or where rapid temporal variation associated with frontal movement may be strong. Interestingly, nugget estimates appear to be disproportionately low within the SCB and over the wide shelves of the southern Baja Peninsula, where very low values typical of the subtropical gyre lie within ~50 km of the coast.

Sill estimates calculated from mode 1 model fits follow a spatial distribution similar to mean chlorophyll concentrations and, where elevated near the shelf and slope, similar to annual and semiannual amplitudes (Figure 7.14a). Strong similarities between the magnitude of dominant intraseasonal fluctuations, mean concentrations and the strength of seasonal fluctuations suggest a close coupling between intraseasonal variability and large-scale, seasonally variable distributions. Furthermore, strong similarities between the mode 1 EOFs and spatial amplitude functions of SST and chlorophyll suggest a regionally dominant, shared source of intraseasonal variability. According to our interpretation of SST structure, dominant chlorophyll variability thereby follows from the distortion of large-scale horizontal gradients by mesoscale surface currents. As with SST, the seasonally recurrent development, intensification and slow westward migration of the CC core and surrounding eddies likely contributes a regionally dominant mode of variability with characteristic time scales centered at ~60 days, equivalent to dominant periods of ~120 days.

The spatial distribution of peak contributions from high-mode structure is similar to that of the mode 1 sill, though everywhere much weaker and with limited offshore extension (Figure 7.15). Peak contributions are typically centered over time lags of 20-45 days close to the coast where modes 2-4 play a prominent role in describing

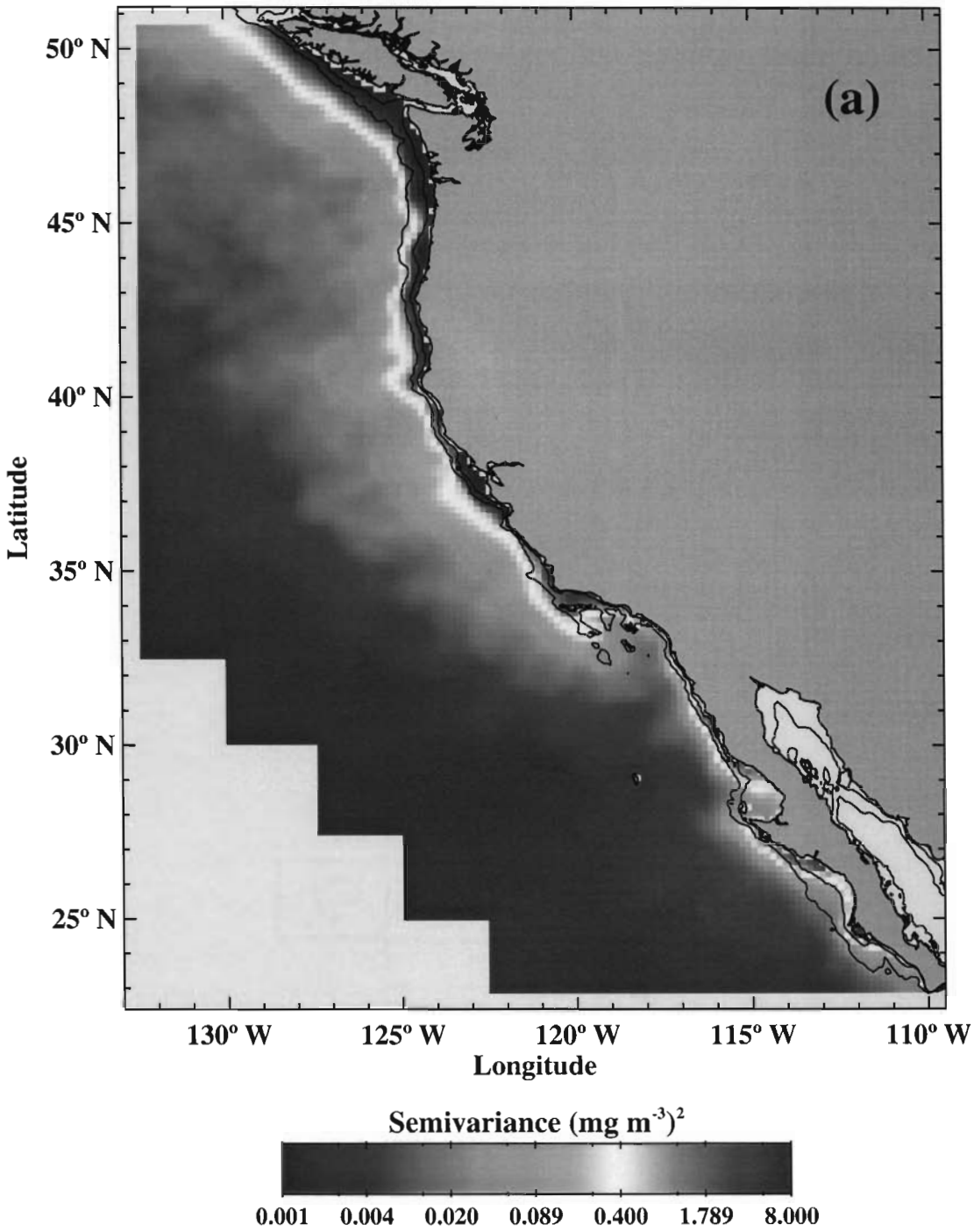

Figure 7.14 - *Semivariance Contributed by Chlorophyll Mode 1*
(a) Chlorophyll semivariance contributed by the mode 1 semivariogram structure, calculated as the sill of the mode 1 exponential model. Data were smoothed with a 5 x 5 moving average.

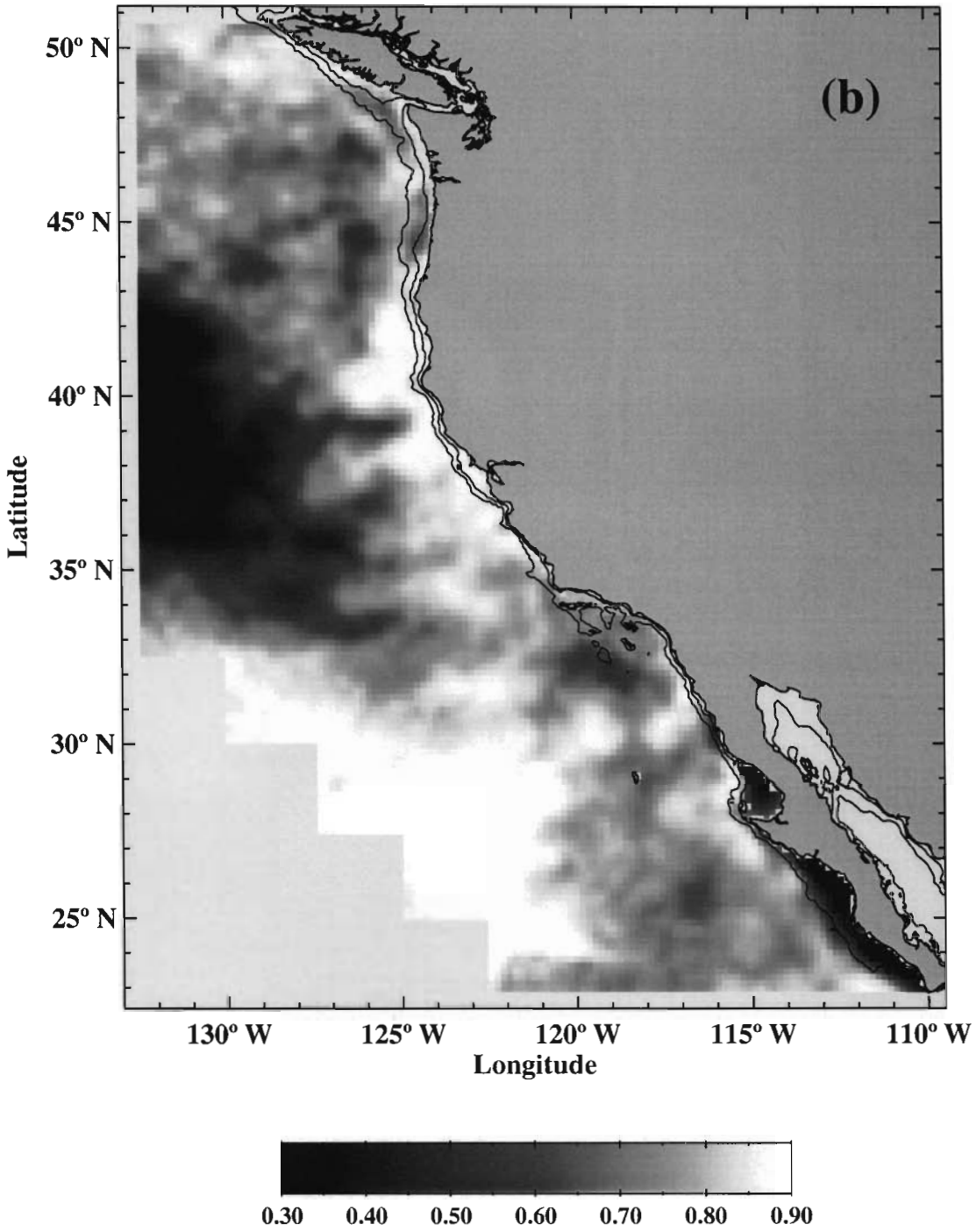

Figure 7.14 - *Continued*
(b) Fraction of total chlorophyll variance contributed by the mode 1 semivariogram structure. Total variance was approximated as the sum of variance contributed by the mean seasonal cycle, dominant intraseasonal variability described by the mode 1 structure, and interannual variability. Data were smoothed with a 5 x 5 moving average.

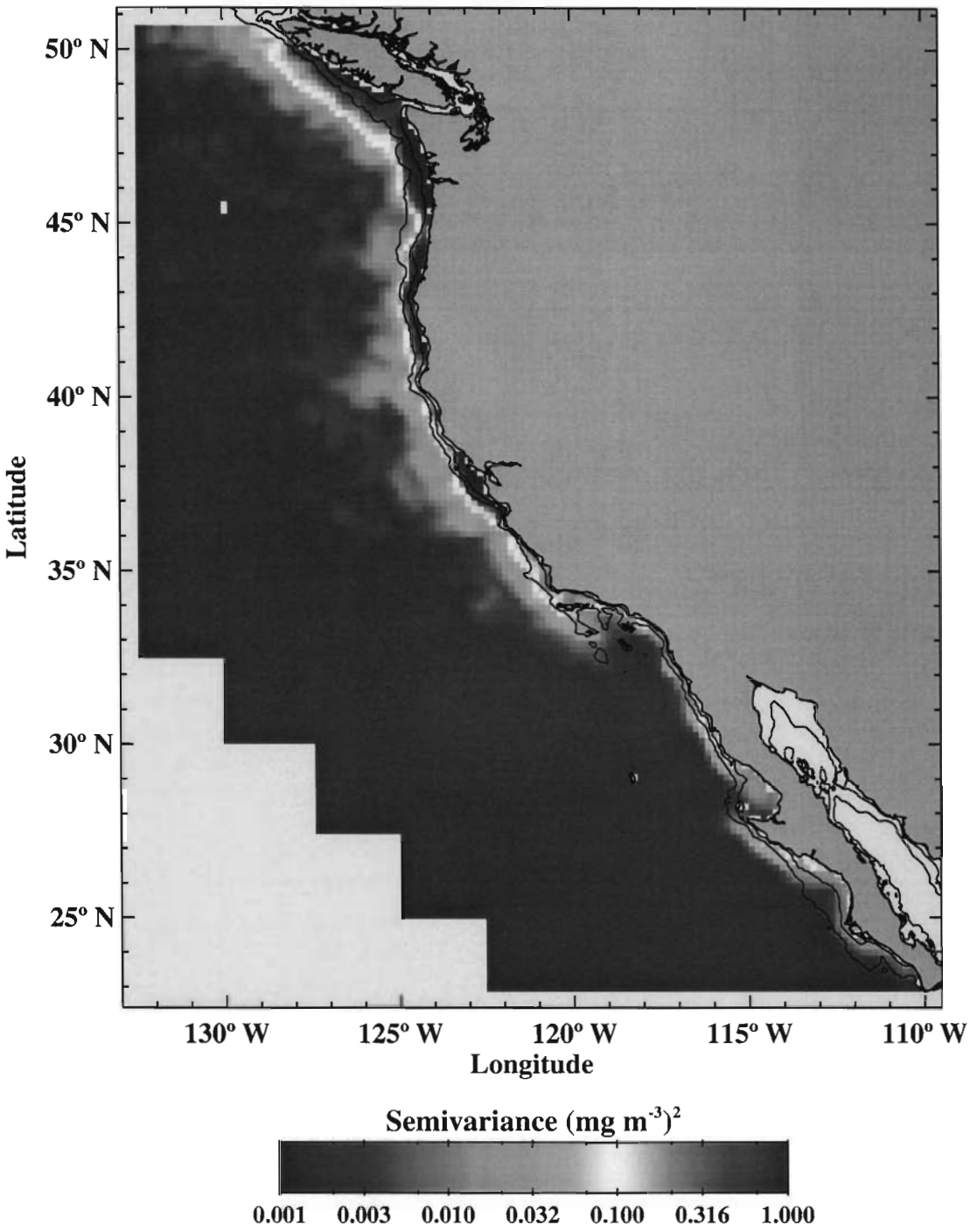

Figure 7.15 - *Semivariance Introduced by Chlorophyll Modes 2-4*
Chlorophyll semivariance introduced by modes 2-4, estimated from the largest positive peak of the modes 2-4 semivariogram reconstruction. Data were smoothed with a 5 x 5 moving average.

semivariogram shape. The time lags of peak contributions at high-variance locations are considerably more variable than was the case with SST, consistent with the slightly stronger contributions of the less coherent, more locally variable modes 3 and 4 (Figure 7.2). Inshore from Vancouver Island to Point Conception and along the outer boundary of the SCB, the structure introduced by modes 2-4 shifts peak semivariance to shorter lags inshore, where mode 1 contributions are notably weak. A similar tendency is evident along the inner boundary of the SCB and along the northernmost Baja Peninsula (Figure 7.1). Although these peaked semivariograms suggest a more or less regular pattern of chlorophyll variation, this assumes a stationary variance structure, constant across seasons and between years. Chlorophyll fluctuations are likely influenced by irregularly spaced events of 20-45 days duration. Here we can conclude only that chlorophyll variance structure is consistently shifted toward lags of 20-45 days inshore. This shift is most prominent north of Point Conception and most clearly divergent from patterns of SST variation between Point Conception and Cape Mendocino (Figure 7.1).

The spatial and temporal statistics of surface temperature and chlorophyll are often compared as a means of diagnosing the strength of physical control of phytoplankton distributions over the mesoscales [e.g. Abbott and Letelier, 1998; Denman and Abbott, 1994; Smith et al., 1988]. Divergent statistical structure may indicate increased biological control through nonconservative processes such as growth or grazing. SST is not however, a strictly conservative tracer of horizontal mesoscale circulation as it responds to variations in surface heating and vertical exchange between the surface and deeper layers. Furthermore, divergent patterns of temporal variability between chlorophyll and SST provide a reliable indication of the dominance of different

structuring processes only under an assumption of statistical stationarity. Semivariograms calculated from residual time series of SST and chlorophyll provide a measure of average variance structure aggregated over the length of the data record. If patterns of variability and overall levels of variability change in time, the shape of the semivariogram may preferentially reflect structure present during periods of high variance. Within the CCS, the mesoscale circulation that appears to contribute the dominant intraseasonal variability of SST and chlorophyll is itself seasonally variable, sensitive to interannual events, and superimposed over seasonal and interannual variations in the intensity of large-scale gradients that in turn affect the magnitude of intraseasonal variance. The degree to which mesoscale forcing is reflected in the shapes of SST and chlorophyll semivariograms will thereby depend in part on the relative timing of evolving patterns of mesoscale currents and large-scale distributions. Such an explanation of statistical divergence between SST and chlorophyll seems less plausible inshore along the California coastline, where the strongest horizontal gradients of both should coincide with periods of strong upwelling.

Past statistical descriptions of SST and chlorophyll variability near the California coast have emphasized the apparent simultaneous evolution of mesoscale surface patterns. Denman and Abbott [1994] found no significant difference between wavenumber spectra or temporal decorrelation scales calculated from satellite-derived SST and surface pigment concentrations off northern California. Their results suggest that over space scales of 25-100 km and time scales of about 1-10 days, phytoplankton essentially act as passive tracers of mesoscale flow. The horizontal mesoscale circulation of the surface layer immediately offshore of northern California is apparently so

energetic that the collective impact of growth, grazing, mortality, etc. is incapable of imposing persistent structure at these scales. Based on spatial power spectra calculated from satellite imagery collected off southern California, Smith et al. [1988] similarly infer a shared response of SST and surface pigment concentrations to turbulent stirring over scales of 10-100 km. Abbott and Letelier [1998] present Lagrangian decorrelation scales calculated from time series of surface temperature and chlorophyll obtained by drifters deployed off California. They too infer common control of surface temperature and chlorophyll variability by the highly energetic surface circulation found within several hundred kilometers of the California coast.

Statistical structure shared between surface temperature and chlorophyll over the shorter time scales and limited spatial scales considered by the studies just described are not inconsistent with divergent structure over the longer time scales considered here. Chavez et al. [1991] and Huyer et al. [1991] describe a sequence of hydrographic surveys mapping the flow of the CC core as it meandered seaward of Point Arena during the summer of 1988. The path of the current core remained stable for close to a month before rapidly realigning to a more alongshore orientation. Whereas patterns of dynamic topography, surface temperature and surface nitrate concentrations evolved in parallel throughout the survey sequence, chlorophyll concentrations and neritic diatom populations decreased dramatically in areas where nutrients remained high or actually increased. Chavez et al. [1991] suggest a possible disruption of physical conditions needed for diatom proliferation during the realignment, including perhaps an interruption of diatom seeding. These observations further suggest that the otherwise simultaneous evolution of SST and surface chlorophyll concentrations may be interrupted by major

realignments of coastal currents. The specific consequences of such events likely vary according to complex interactions between local currents, coastal topography or shelf/slope morphology, and the life history strategies of dominant members of coastal phytoplankton assemblages. Major current realignments may, however, dominate chlorophyll fluctuations over time scales of several weeks or longer and may force the inshore shift in chlorophyll variance toward time lags of 20-45 days. Once again, this shift is most clearly divergent from dominant patterns of SST variation between Cape Mendocino and Point Conception.

As a fraction of total variance, the magnitude of dominant intraseasonal variability estimated by the mode 1 sill reflects many of the same features evident in patterns of seasonality, with areas of high intraseasonal variance coinciding with areas of low seasonality (compare Figures 5.2d and 7.14b). Contributions of intraseasonal variance are very strong within the subtropical gyre where seasonality is correspondingly weak. Intraseasonal variation within this area is, however, poorly resolved by our daily time series and sill estimates reflect in part large nugget values (e.g. Figure 7.1h). High-frequency chlorophyll fluctuations within gyre waters may result from submesoscale nutrient enrichment in a region where mesoscale turbulent stirring of nutrients and phytoplankton is generally weak [Lévy, 2003]. Immediately to the north, weak intraseasonal variability coincides with strong seasonality at the eastern end of the North Pacific transition zone, where chlorophyll fluctuations are dominated by seasonal changes in near-surface stratification [Longhurst, 1998]. Nearshore waters at the same latitudes and adjacent to the California coast are dominated by heavy contributions of intraseasonal variance, bounded offshore by the seasonally recurrent path of the CC core.

Dominant chlorophyll fluctuations inshore appear to be defined by intense mesoscale jet and eddy variability, as described above. Intraseasonal contributions progressively weaken offshore and consistently constitute a lesser fraction of total variability throughout the Pacific Northwest and within the SCB. Seasonal variability dominates the shelf and upper slope of southern Baja in stark contrast to California waters. Whereas the strong seasonality of alongshore winds off California forces the recurrent evolution of energetic jets and eddies, the weak seasonality of wind forcing along the Baja coast may favor a more subordinate role of intraseasonal variation through less intense mesoscale circulation.

Chapter 8

SUMMARY

Physical forcing and biological response within the CCS vary greatly over a wide range of scales. The seasonal evolution of large-scale wind systems introduces strong latitudinally dependent seasonal cycles of physical and biological processes. Patterns of mesoscale variability are dominated by an energetic jet and eddy field formed through intrinsic instabilities of coastal currents. Basin-scale atmospheric and oceanic processes modulate seasonal and intraseasonal variation over interannual time scales. Complex interactions between coastal topography or shelf/slope morphology and coastal currents or winds provide for considerable local variation over all time scales. Here we have quantified and compared dominant patterns of physical and biological variability acting over seasonal, interannual and intraseasonal time scales throughout the CCS using multiyear time series of satellite-derived SST and chlorophyll.

Spring and summer upwelling winds are strongest and most persistent along central and northern California, where equatorward winds are channeled along the coastal boundary [Dorman and Winant, 1995]. Coastal upwelling within this region arrests summer heating and strongly depresses seasonal cycles of SST within several hundred kilometers of the coast. The timing, duration and intensity of the upwelling season determine annual and semiannual phases, and surface temperatures fluctuate between spring minima and late summer maxima. Inshore chlorophyll concentrations peak in mid- to late summer when cross-shelf distributions are determined in part by the position of the seasonally recurrent CC core. Annual amplitudes are depressed along the

boundary of inshore summer maxima and offshore summer minima, which off northern California coincides with the path of the current core as it meanders seaward of Cape Mendocino and Point Arena. Semiannual harmonics within several hundred kilometers of the coast describe a tendency for diffuse blooms to follow the transition to strong and sustained wind forcing each spring and the westward displacement of mesoscale circulation each fall.

Seasonal cycles of SST and chlorophyll differ considerably further to the north and south. Propagating storms dominate wind forcing throughout the Pacific Northwest, where summer winds are strong but highly variable [Dorman and Winant, 1995]. SST fluctuates between winter minima and summer maxima. Chlorophyll follows a strong seasonal progression similar to that off northern and central California, though summer maxima arrive at progressively later dates moving northward of Cape Mendocino. The inner SCB shows a more oceanic character owing to an intrusion of oligotrophic water and generally weak wind forcing. Chlorophyll typically peaks in mid- to late winter when the upper ocean is well mixed and surface temperatures are low. Near-surface concentrations drop to seasonal minima in mid- to late summer as surface temperatures peak and deep chlorophyll maxima develop within a stratified water column. Upwelling-favorable winds persist year-round along the central and southern Baja coast, but are generally weaker than off northern and central California. Very strong SST seasonality along the Baja margin south of Punta Eugenia appears to be driven more by cycles of surface heat exchange than by upwelling, although spring minima coincide with the strongest wind forcing. Strong seasonal cycles peaking in late spring dominate

chlorophyll variability, and mesoscale circulation appears to play a minimal role in determining seasonally recurrent spatial distributions.

Interannual variation of SST is concentrated along southern Oregon and northern California, where interannual variability is of comparable strength to mean seasonality, and off South-central Baja. Propagating oceanic disturbances and regional atmospheric anomalies during the El Niño of 1997-1998 forced anomalous patterns of surface advection and a dramatic elevation of SST in both areas. Local upwelling filaments present off Cape Mendocino and Point Arena at the onset of our study period appear to have mitigated the impact of El Niño conditions to some extent. Elevated levels of coastal upwelling and southward advection during the cool La Niña conditions of 1999-2001 contributed to elevated levels of interannual variance off Baja but had little impact on SST across the northern CCS. Unlike SST, elevated levels of chlorophyll variability acting over interannual scales follow a spatial distribution similar to the annual mean and to strong seasonal fluctuations. This is consistent with a principle cause of interannual variability rooted in the widespread depression and elevation of the nutricline, resulting in predominantly negative and positive anomalies during El Niño and La Niña, respectively. As a fraction of total variance, coastal concentrations are less sensitive to interannual variation than those further from shore. Large interannual contributions to total chlorophyll variability are concentrated within discrete mesoscale pockets off California, suggesting some degree of control by variations in mesoscale circulation.

Dominant patterns of intraseasonal variability of both SST and chlorophyll are caused by the seasonally recurrent formation, intensification and westward migration of the CC core and surrounding eddies. The slow advection of prominent eddies and

meanders defines a characteristic time scale of ~60 days (equivalent to a period of ~120 days). Dominant intraseasonal structure of SST and chlorophyll is most clearly defined within ~400-600 kilometers of the coast south of Cape Mendocino, where eddy energy associated with time-varying geostrophic currents is strongest [Strub and James, 2000]. SST variance at dominant intraseasonal scales is greatest off southern Baja and along southern Oregon and northern California. These are areas of strong seasonal heating gradients and intense jet and eddy activity, where mesoscale circulation induces strong SST variability. Elevated levels of chlorophyll variance coincide with elevated mean concentrations and strong seasonal fluctuations, consistent with dominant intraseasonal variability arising through the distortion of large-scale, seasonally variable distributions.

Coherent deviations from dominant patterns of SST and chlorophyll variation occur over similar time scales but with differing spatial patterns. A coherent and widespread introduction of SST variance at time scales of ~40 days occurs across much of the northern CCS, most notably along southern Oregon and northern California. 40-day fluctuations of SST may be rooted in organized patterns of wind forcing associated with fluctuations in regional atmospheric pressure gradients. Northern California appears to lie at a transition in dominant SST forcing between eddy variability to the south and vigorous atmospheric forcing to the north. Chlorophyll variance is consistently shifted to time scales of 20-45 days inshore, most notably north of Point Conception. These scales of chlorophyll variability most clearly diverge from the longer time scales of SST within several hundred kilometers of the coast between Point Conception and Cape Mendocino. Divergence at these longer time scales is not inconsistent with the simultaneous evolution of SST and chlorophyll distributions over shorter time scales. 20-45 day fluctuations of

inshore chlorophyll concentrations may arise from major realignments of mesoscale currents that disrupt the physical conditions needed for diatom proliferation.

Although satellite remote sensing offers the sole means of quantifying physical and biological variability over such large regional scales, biased and nonrandom sampling caused by cloud cover and orbital constraints confound the description of SST and chlorophyll variability over intraseasonal time scales. An 8-10 day oscillation in the availability of SST observations is apparent at lower latitudes and appears capable of altering semivariogram shape at short time lags. A comparable sampling fluctuation is not apparent in chlorophyll time series. Subtle or locally variable features evident in semivariograms may not always faithfully reflect patterns of oceanic variability nonetheless. We further need to assess the degree to which one or a few events may dominate patterns of variability resolved by various statistical tools including the semivariogram. Where significant nonstationarity of SST or chlorophyll variance occurs, we need to better understand the nature of these events, their interactions with variability at shorter and longer time scales, and their importance to local and regional marine ecology.

REFERENCES

Abbott, M.R., and B. Barksdale, Phytoplankton pigment patterns and wind forcing off central California, *J. Geophys. Res.*, 96, 14,649-14,667, 1991.

Abbott, M.R., and R.M. Letelier, Decorrelation scales of chlorophyll as observed from bio-optical drifters in the California Current, *Deep-Sea Res. II*, 45, 1639-1667, 1998.

Bakun, A., and C.S. Nelson, The seasonal cycle of wind-stress curl in subtropical eastern boundary current regions, *J. Phys. Oceanogr.*, 21, 1,815-1,834, 1991.

Barth, J.A., T.J. Cowles, P.M. Kosro, R.K. Shearman, A. Huyer, and R.L. Smith, Injection of carbon from the shelf to offshore beneath the euphotic zone in the California Current, *J. Geophys. Res.*, 107(C6), 3057, doi:10.1029/2001JC000956, 2002.

Barth, J.A., S.D. Pierce, and R.L. Smith, A separating coastal upwelling jet at Cape Blanco, Oregon and its connection to the California Current System, *Deep-Sea Res. II*, 47, 783-810, 2000.

Batteen, M.L., Wind-forced modeling studies of currents, meanders, and eddies in the California Current system, *J. Geophys. Res.*, 102, 985-1,010, 1997.

Beardsley, R.C., C.E. Dorman, C.A. Friehe, L.K. Rosenfeld, and C.D. Winant, Local atmospheric forcing during the Coastal Ocean Dynamics Experiment, I, A description of the marine boundary layer and atmospheric conditions over a Northern California upwelling region, *J. Geophys. Res.*, 92, 1,467-1,488, 1987.

Bograd, S.J., and R.J., Lynn, Anomalous subarctic influence in the southern California Current during 2002, *Geophys. Res. Lett.*, 30(15), 8020, doi:10.1029/2003GL017446, 2003.

Bograd, S.J., and R.J. Lynn, Physical-biological coupling in the California Current during the 1997-99 El Niño-La Niña cycle, *Geophys. Res. Lett.*, 28, 275-278, 2001.

Botsford, L.W., Physical influences on recruitment to California Current invertebrate populations on multiple scales, *ICES J. Mar. Sci.*, 58, 1,081-1,091, 2001.

Breaker, L.C., and P.A.W. Lewis, A 40-50 day oscillation in sea-surface temperature along the central California coast, *Estuarine, Coastal and Shelf Sci.*, 26, 395-408, 1988.

Breaker, L.C., P.C. Liu, and C. Torrence, Intraseasonal oscillations in sea surface temperature, wind stress, and sea level off the central California coast, *Cont. Shelf Res.*, 21, 727-750, 2001.

Brink, K.H., R.C. Beardsley, J. Paduan, R. Limeburner, M. Caruso, and J.G. Sires, A view of the 1993-1994 California Current based on surface drifters, floats, and remotely sensed data, *J. Geophys. Res.*, 105, 8,575-8,604, 2000.

Caldeira, R.M.A., and P. Marchesiello, Ocean response to wind sheltering in the Southern California Bight, *Geophys. Res. Lett.*, 29(13), 1635, doi:10.1029/2001GL014563, 2002.

Campbell, J.W., The lognormal distribution as a model for bio-optical variability in the sea, *J. Geophys. Res.*, 100, 13,237-13,254, 1995.

Chavez, F.P., R.T. Barber, P.M. Kosro, A. Huyer, S.R. Ramp, T.P. Stanton, and B.R. de Mendiola, Horizontal transport and distribution of nutrients in the coastal transition zone off northern California: Effects on primary production, phytoplankton biomass and species composition, *J. Geophys. Res.*, 96, 14,833-14,848, 1991.

Chavez, F.P., J.T. Pennington, C.G. Castro, J.P. Ryan, R.P. Michisaki, B. Schlining, P. Walz, K.R. Buck, A. McFadyen, and C.A. Collins, Biological and chemical consequences of the 1997-1998 El Niño in central California waters, *Prog. Oceanogr.*, 54, 205-232, 2002.

Chelton, D.B., Large-scale response of the California Current to forcing by the wind stress curl, *CalCOFI Rep.*, 23, 130-148, 1982.

Chelton, D.B., and M.G. Schlax, Estimation of time averages from irregularly spaced observations: With application to Coastal Zone Color Scanner estimates of chlorophyll concentration, *J. Geophys. Res.*, 96, 14,669-14,692, 1991.

Chereskin, T.K., M.Y. Morris, P.P. Niiler, P.M. Kosro, R.L. Smith, S.R. Ramp, C.A. Collins, and D.L. Musgrave, Spatial and temporal characteristics of the mesoscale circulation of the California Current from eddy-resolving moored and shipboard measurements, *J. Geophys. Res.*, 105, 1,245-1,269, 2000.

Corwith, H.L., and P.A. Wheeler, El Niño related variations in nutrient and chlorophyll distributions off Oregon, *Prog. Oceanogr.*, 54, 361-380, 2002.

Cressie, N., and D.M. Hawkins, Robust estimation of the variogram, *J. Int. Assoc. Math. Geol.*, 12, 115-125, 1980.

D'Agostino, R.B., Tests for the normal distribution, in: *Goodness-of-fit techniques*, edited by R.B. D'Agostino and M.A. Stephens, pp. 367-419, Marcel Dekker, New York, 1986.

Davis, R.E., Predictability of sea surface temperature and sea level pressure anomalies over the North Pacific Ocean, *J. Phys. Oceanogr.*, 6, 249-266, 1976.

Denman, K.L., and M.R. Abbott, Time scales of pattern evolution from cross-spectrum analysis of advanced very high resolution radiometer and coastal zone color scanner imagery, *J. Geophys. Res.*, 99, 7,433-7,442, 1994.

Denman, K.L., and H.J. Freeland, Correlation scales, objective mapping and a statistical test of geostrophy over the continental shelf, *J. Mar. Res.*, 43, 517-539, 1985.

Deschamps, P.Y., R. Frouin, and L. Wald, Satellite determination of the mesoscale variability of the sea surface temperature, *J. Phys. Oceanogr.*, 11, 864-870, 1981.

Doney, S.C., D.M. Glover, S.J. McCue, and M. Fuentes, Mesoscale variability of SeaWiFS satellite ocean color: Global patterns and spatial scales, *J. Geophys. Res.*, 108(C2), 3024, doi:10.1029/2001JC000843, 2003.

Dorman, C.E., Possible role of gravity currents in Northern California's coastal summer wind reversals, *J. Geophys. Res.*, 92, 1,497-1,506, 1987.

Dorman, C.E., A.G. Enriquez, and C.A. Friehe, Structure of the lower atmosphere over the northern California coast during winter, *Mon. Wea. Rev.*, 123, 2,384-2,404, 1995.

Dorman, C.E., and C.D. Winant, Buoy observations of the atmosphere along the west coast of the United States, 1981-1990, J. Geophys. Res., 100, 16,029-16,044, 1995.

Durazo, R., and T.R. Baumgartner, Evolution of oceanographic conditions of Baja California: 1997-1999, *Prog. Oceanogr.*, 54, 7-31, 2002.

Edwards, K.A., D.P. Rogers, and C.E. Dorman, Adjustment of the marine atmospheric boundary layer to the large-scale bend in the California coast, *J. Geophys. Res.*, 107(C12), 3213, doi:10.1029/2001JC000807, 2002.

Efron, B., and R.J. Tibshirani, *An introduction to the bootstrap*, Chapman and Hall/CRC, Boca Raton, 1998.

Espinosa-Carreon, T.L., P.T. Strub, E. Beier, F. Ocampo-Torres, and G. Gaxiola-Castro, Seasonal and interannual variability of satellite-derived chlorophyll pigment, surface height, and temperature off Baja California, *J. Geophys., Res.*, 109, C03039, doi:10.1029/2003JC002105, 2004.

Freeland, H.J., G. Gatien, A. Huyer, and R.L. Smith, Cold halocline in the northern California Current: An invasion of subarctic water, *Geophys. Res. Lett.*, 30(3), 1141, doi:10.1029/2002GL016663, 2003.

Fuentes, M., S.C. Doney, D.M. Glover, and S.J. McCue, Spatial structure of the SeaWiFS ocean color data for the North Atlantic Ocean, in: *Studies in the atmospheric sciences (Lecture notes in statistics Vol. 144)*, edited by M. Berliner, D. Nychka, and T. Hoar, pp. 153-171, Springer-Verlag, New York, 2001.

Goovaerts, P., *Geostatistics for natural resources evaluation*, Oxford Univ. Press, New York, 1997.

Halliwell, G.R., and J.S. Allen, The large-scale coastal wind field along the west coast of North America, 1981-1982, *J. Geophys. Res.*, 92, 1,861-1,884, 1987.

Haney, R.L., R.A. Hale, and D.E. Dietrich, Offshore propagation of eddy kinetic energy in the California Current, *J. Geophys. Res.*, 106, 11,709-11,717, 2001.

Hayward, T.L., T.R. Baumgartner, D.M. Checkley, R. Durazo, G. Gaxiola-Castro, K.D. Hyrenbach, A.W. Mantyla, M.M. Mullin, T. Murphree, F.B. Schwing, P.E. Smith, and M. Tegner, The state of the California Current, 1998–99: Transition to cool-water conditions, *CalCOFI Rep.*, 40, 29-62, 1999.

Hayward, T.L., and E.L. Venrick, Nearsurface pattern in the California Current: Coupling between physical and biological structure, *Deep-Sea Res. II*, 45, 1,617-1,638, 1998.

Hickey, B.M., Coastal oceanography of western North America from the tip of Baja California to Vancouver Island, in: *The Sea*, Vol. 11, edited by A.R. Robinson and K.H. Brink, pp. 345-393, John Wiley, New York, 1998.

Hill, A.E., B.M. Hickey, F.A. Shillington, P.T. Strub, K.H. Brink, E.D. Barton, and A.C. Thomas, Eastern ocean boundaries, in: *The Sea*, Vol. 11, edited by A.R. Robinson and K.H. Brink, pp. 29-67, John Wiley, New York, 1998.

Hood, R.R., M.R. Abbott, and A. Huyer, Phytoplankton and photosynthetic light response in the coastal transition zone off northern California in June 1987, *J. Geophys. Res.*, 96, 14,769-14,780, 1991.

Hood, R.R., M.R. Abbott, A. Huyer, and P.M. Kosro, Surface patterns in temperature, flow, phytoplankton biomass, and species composition in the coastal transition zone off northern California, *J. Geophys. Res.*, 95, 18,081-18,094, 1990.

Hooker, S.B., and W.E. Esaias, An overview of the SeaWiFS project, *EOS, Trans. Amer. Geophys. Union*, 74, 241-248, 1993.

Hormazabal, S., G. Shaffer, and O. Leth, Coastal transition zone off Chile, *J. Geophys. Res.*, 109, C01021, doi:10.1029/2003JC001956, 2004.

Husby, D.M., and C.S. Nelson, Turbulence and vertical stability in the California Current, *CalCOFI Rep.*, 23, 113-129, 1982.

Hutchings, L., Fish harvesting in a variable, productive environment – Searching for rules or searching for exceptions?, in: *Benguela trophic functioning*, edited by A.I.L. Payne, K.H. Brink, K.H. Mann, and R. Hilborn, *S. Afr. J. Mar. Sci.*, 12, 297-318, 1992.

Hutchings, L., G.C. Pitcher, T.A. Probyn, and G.W. Bailey, The chemical and biological consequences of coastal upwelling, in: *Upwelling in the ocean: Modern processes and ancient records*, edited by C.P. Summerhayes, K.-C. Emeis, M.V. Angel, R.V. Smith, and B. Zeitzschel, pp. 65-81, John Wiley, New York, 1995.

Huyer, A., J.A. Barth, P.M. Kosro, R.K. Shearman, and R.L. Smith, Upper-ocean water mass characteristics of the California current, Summer 1993, *Deep-Sea Res. II*, 45, 1,411-1,442, 1998.

Huyer, A., P.M. Kosro, J. Fleischbein, S.R. Ramp, T. Stanton, L. Washburn, F.P. Chavez, T.J. Cowles, S.D. Pierce, and R.L. Smith, Currents and water masses of the coastal transition zone off northern California, June to August 1988, *J. Geophys. Res.*, 96, 14,809-14,831, 1991.

Huyer, A., E.J. Sobey, and R.L. Smith, The spring transition in currents over the Oregon continental shelf, *J. Geophys. Res.*, 84, 6,995-7,011, 1979.

Journel, A.G., and C.J. Huijbregts, *Mining geostatistics*, Academic Press, London, 1978.

Kahru, M., and B.G. Mitchell, Influence of the El Niño-La Niña cycle on satellite-derived primary production in the California Current, *Geophys. Res. Lett.*, 29(17), 1846, doi:10.1029/2002GL014963, 2002.

Kahru, M., and B.G. Mitchell, Influence of the 1997-98 El Niño on the surface chlorophyll in the California Current, *Geophys. Res. Lett.*, 27, 2,937-2,940, 2000.

Kelly, K.A., The influence of winds and topography on the sea surface temperature patterns over the northern California slope, *J. Geophys. Res.*, 90, 11,783-11,789, 1985.

Kelly, K.A., R.C. Beardsley, R. Limeburner, K.H. Brink, J.D. Paduan, and T.K. Chereskin, Variability of the near-surface eddy kinetic energy in the California Current based on altimetric, drifter, and moored current data, *J. Geophys. Res.*, 103, 13,067-13,083, 1998.

Kidwell, K.B., NOAA Polar Orbiter Data User's Guide (TIROS-N through NOAA-14), NOAA, NESDIS, NCDC, Climate Services Division, Satellite Services Branch, 1998.

Kosro, P.M., A poleward jet and equatorward undercurrent observed off Oregon and northern California, during the 1997-98 El Niño, *Prog. Oceanogr.*, 54, 343-360, 2002.

Kosro, P.M., Huyer, A., Ramp, S.R., Smith, R.L., Chavez, F.P., Cowles, T.J., Abbott, M.R., Strub, P.T., Barber, R.T., Jessen, P., and L.F. Small, The structure of the transition zone between coastal waters and the open ocean off Northern California, winter and spring 1987, *J. Geophys. Res.*, 96, 14,707-14,730, 1991.

Kudela, R.M., and F.P. Chavez, Multi-platform remote sensing of new production in central California during the 1997-1998 El Niño, *Prog. Oceanogr.*, 54, 233-249, 2002.

Kutzbach, J.E., Empirical eigenvectors of sea-level pressure, surface temperature, and precipitation complexes over North America, *J. Appl. Meteorol.*, 6, 791-802, 1967.

Ladah, L.B., The shoaling of nutrient-enriched subsurface waters as a mechanism to sustain primary productivity off Central Baja California during El Niño winters, *J. Mar. Systems*, 42, 145-152, 2003.

Lagerloef, G.S.E., The Point Arena eddy: A recurring summer anticyclone in the California Current, *J.Geophys. Res.*, 97, 12,557-12,568, 1992.

Landry, M.R., R.T. Barber, R.R. Bidigare, F. Chai, K.H. Coale, H.G. Dam, M.R. Lewis, S.T. Lindley, J.J. McCarthy, M.R. Roman, D.K. Stoecker, P.G. Verity, and J.R. White, Iron and grazing constraints on primary production in the central equatorial Pacific: An EqPac synthesis, *Limnol. Oceanogr.*, 42, 405-418, 1997.

Largier, J.L., B.A. Magnell, and C.D. Winant, Subtidal circulation over the northern California shelf, *J. Geophys. Res.*, 98, 18,147-18,179, 1993.

Leeuwenburgh, O., and D. Stammer, The effect of ocean currents on sea surface temperature anomalies, *J. Phys. Oceanogr.*, 31, 2,340-2,358, 2001.

Legendre, L., and J. Le Fèvre, Interactions between hydrodynamics and pelagic ecosystems: Relevance to resource exploitation and climate change, in: *Benguela trophic functioning*, edited by A.I.L. Payne, K.H. Brink, K.H. Mann, and R. Hilborn, *S. Afr. J. Mar. Sci.*, 12, 477-486, 1992.

Lévy, M., Mesoscale variability of phytoplankton and of new production: Impact of the large-scale nutrient distribution, *J. Geophys. Res.*, 108(C11), 3358, doi:10.1029/2002JC001577, 2003.

Logerwell, E.A., B. Lavaniegos, and P.E. Smith, Spatially-explicit bioenergetics of Pacific sardine in the Southern California Bight: Are mesoscale eddies areas of exceptional prerecruit production?, *Prog. Oceanogr.*, 49, 391-406, 2001.

Longhurst, A., *Ecological geography of the sea*, Academic Press, San Diego, 1998.

Lynn, R.J., T. Baumgartner, J. Garcia, C.A. Collins, T.L. Hayward, K.D. Hyrenbach, A. W. Mantyla, T. Murphree, A. Shankle, F.B. Schwing, K.M. Sakuma, and M.J. Tegner, The state of the California Current 1997–1998: Transition to El Niño Conditions, *CalCOFI Rep.*, 39, 25-50, 1998.

Lynn, R.J., S.J. Bograd, T.K. Chereskin, and A. Huyer, Seasonal renewal of the California Current: The spring transition off California, *J. Geophys. Res.*, 108(C8), 3279, doi:10.1029/2003JC001787, 2003.

Lynn, R.J., and J.J. Simpson, The California Current System: The seasonal variability of its physical characteristics, *J. Geophys. Res.*, 92, 12,947-12,966, 1987.

Marchesiello, P., J.C. McWilliams, and A. Shchepetkin, Equilibrium structure and dynamics of the California Current System, *J. Phys. Oceanogr.*, 33, 753-783, 2003.

McPhaden, M.J., Genesis and evolution of the 1997-1998 El Niño, *Science*, 283, 950-954, 1999.

Mejía, J.M., and I. Rodríguez-Iturbe, Correlation links between normal and log normal processes, *Water Resources Res.*, 10, 689-690, 1974.

Michaelsen, J., X. Zhang, and R.C. Smith, Variability of pigment biomass in the California Current System as determined by satellite imagery 2. Temporal variability, *J. Geophys. Res.*, 93, 10,883-10,896, 1988.

Murphree, T., S.J. Bograd, F.B. Schwing, and B. Ford, Large scale atmosphere-ocean anomalies in the northeast Pacific during 2002, *Geophys. Res. Lett.*, 30(15), 8026, doi:10.1029/2003GL017303, 2003.

Murphree, T., P. Green-Jessen, F.B. Schwing, and S.J. Bograd, The seasonal cycle of wind stress curl and its relationship to subsurface ocean temperature in the Northeast Pacific, *Geophys. Res. Lett.*, 30(9), 1469, doi:10.1029/2002GL016366, 2003.

Narimousa, S., and T. Maxworthy, Application of a laboratory model to the interpretation of satellite and field observations of coastal upwelling, *Dyn. Atmos. Oceans*, 13, 1-46, 1989.

Narimousa, S., and T. Maxworthy, Coastal upwelling on a sloping bottom: Formation of plumes, jets and pinched-off cyclones, *J. Fluid Mech.*, 176, 169-190, 1987.

Nelson, C.S., and D.M. Husby, Climatology of surface heat fluxes over the California current region, *NOAA Tech. Rep. NMFS SSRF-763*, U.S. Department of Commerce, Washington, D.C., 1983.

O'Reilly, J.E., S. Maritorena, B.G. Mitchell, D.A. Siegel, K.L. Carder, S.A. Garver, M. Kahru, and C. McClain, Ocean color chlorophyll algorithms for SeaWiFS, *J. Geophys. Res.*, 103, 24,937-24,953, 1998.

O'Reilly, J.E. et al., Ocean color chlorophyll *a* algorithms for SeaWiFS, OC2, and OC4: Version 4, in: *SeaWiFS Postlaunch Calibration and Validation Analyses*, Part 3, edited by S.B. Hooker and E.R. Firestone, *NASA Tech. Memo. 206892*, Vol. 11, 9-23, NASA Goddard Space Flight Center, Greenbelt, Maryland, 2000.

Overland, J.E., and R.W. Preisendorfer, A significance test for principal components applied to a cyclone climatology, *Mon. Weather Rev.*, 110, 1-4, 1982.

Parrish, R.H., C.S. Nelson, and A. Bakun, Transport mechanisms and reproductive success of fishes in the California Current, *Biol. Oceanogr.*, 1, 175-203, 1981.

Pauly, D., and V. Christensen, Primary production required to sustain global fisheries, *Nature*, 374, 255-257, 1995.

Peláez, J., and J.A. McGowan, Phytoplankton pigment patterns in the California Current as determined by satellite, *Limnol. Oceanogr.*, 31, 927-950, 1986.

Peterson, W.T., J.E. Keister, and L.R. Feinberg, The effects of the 1997-99 El Niño/La Niña events on hydrography and zooplankton off the central Oregon coast, *Prog. Oceanogr.*, 54, 381-398, 2002.

Pickett, M.H., and J. D. Paduan, Ekman transport and pumping in the California Current based on the U.S. Navy's high-resolution atmospheric model (COAMPS), *J. Geophys. Res.*, 108 (C10), 3327, doi:10.1029/2003JC001902, 2003.

Priesendorfer, R.W., *Principle components analysis in meteorology and oceanography*, Elsevier, Amsterdam, 1988.

Radeloff, V.C., T.F. Miller, H.S. He, and D.J. Mladenoff, Periodicity in spatial data and geostatistical models: Autocorrelation between patches, *Ecography*, 23, 81-91, 2000.

Samelson, R., P. Barbour, J. Barth, S. Bielli, T. Boyd, D. Chelton, P. Kosro, M. Levine, and E. Skyllingstad, Wind stress forcing of the Oregon coastal ocean during the 1999 upwelling season, *J. Geophys. Res.*, 107, 2002.

Schwing, F.B., T. Murphree, L. deWitt, and P.M. Green, The evolution of oceanic and atmospheric anomalies in the northeast Pacific during the El Niño and La Niña events of 1995-2001, *Prog. Oceanogr.*, 54, 459-491, 2002.

Simpson, J.J., C.J. Koblinsky, J. Peláez, L.R. Haury, and D. Weisenhahn, Temperature-plant pigment-optical relations in a recurrent offshore mesoscale eddy near Point Conception, California, *J. Geophys. Res.*, 91, 12,919-12,936, 1986.

Smith, R.C., X. Zhang, and J. Michaelsen, Variability of pigment biomass in the California Current System as determined by satellite imagery 1. Spatial variability, *J. Geophys. Res.*, 93, 10,863-10,882, 1988.

Smith, R.L., The physical processes of coastal ocean upwelling systems, in: *Upwelling in the ocean: Modern processes and ancient records*, edited by C.P. Summerhayes, K.-C. Emeis, M.V. Angel, R.V. Smith, and B. Zeitzschel, pp. 39-64, John Wiley, New York, 1995.

Smith, R.L., A. Huyer, and J. Fleischbein, The coastal ocean off Oregon from 1961 to 2000: is there evidence of climate change or only of Los Niños?, *Prog. Oceanogr.*, 49, 63-93, 2001.

Soto-Mardones, L., A. Parés-Sierra, J. Garcia, R. Durazo, and S. Hormazabal, Analysis of the mesoscale structure in the IMECOCAL region (off Baja California) from hydrographic, ADCP and altimetry data, *Deep-Sea Res. II*, 51, 785-798, 2004.

Strub, P.T., J.S. Allen, A. Huyer, and R.L. Smith, Large-scale structure of the spring transition in the coastal ocean off western North America, *J. Geophys. Res.*, 92, 1,527-1,544, 1987.

Strub, P.T., T.K. Chereskin, P.P. Niiler, C. James, and M.D. Levine, Altimeter-derived variability of surface velocities in the California Current System: 1. Evaluation of TOPEX altimeter velocity resolution, *J. Geophys. Res.*, 102, 12,727-12,748, 1997.

Strub, P.T., and C. James, Altimeter estimates of anomalous transports into the northern California Current during 2000-2002, *Geophys. Res. Lett.*, 30(15), 8025, doi:10.1029/2003GL017513, 2003.

Strub, P.T., and C. James, Altimeter-derived surface circulation in the large-scale NE Pacific Gyres, Part 2: 1997-1998 El Niño anomalies, *Prog. Oceanogr.*, 53, 185-214, 2002.

Strub, P.T., and C. James, Altimeter-derived variability of surface velocities in the California Current System: 2. Seasonal circulation and eddy statistics, *Deep-Sea Res. II*, 47, 831-870, 2000.

Strub, P.T., and C. James, Atmospheric conditions during the spring and fall transitions in the coastal ocean off western United States, *J. Geophys. Res.*, 93, 15,561-15,584, 1988.

Strub, P.T., C. James, A.C. Thomas, and M.R. Abbott, Seasonal and nonseasonal variability of satellite-derived surface pigment concentration in the California Current, *J. Geophys. Res.*, 95, 11,501-11,530, 1990.

Strub, P.T., P.M. Kosro, A. Huyer, and CTZ Collaborators, The nature of cold filaments in the California Current system, *J. Geophys. Res.*, 96, 14,743-14,768, 1991.

Thomas, A.C., M.-E. Carr, and P.T. Strub, Chlorophyll variability in eastern boundary currents, *Geophys. Res. Lett.*, 28, 3421-3424, 2001.

Thomas, A.C., and W.J. Emery, Relationships between near-surface plankton concentrations, hydrography, and satellite-measured sea surface temperature, *J. Geophys. Res.*, 93, 15,733-15,748, 1988.

Thomas, A.C., F. Huang, P.T. Strub, and C. James, Comparison of seasonal and interannual variability of phytoplankton pigment concentrations in the Peru and California Current systems, *J. Geophys. Res.*, 99, 7355-7370, 1994.

Thomas, A., and P.T. Strub, Cross-shelf phytoplankton pigment variability in the California Current, *Cont. Shelf Res.*, 21, 1,157-1,190, 2001.

Thomas, A.C., and P.T. Strub, Seasonal and interannual variability of pigment concentrations across a California Current frontal zone, *J. Geophys. Res.*, 95, 13,023-13,042, 1990.

Thomas, A.C., and P.T. Strub, Interannual variability in phytoplankton pigment distribution during the spring transition along the west coast of North America, *J. Geophys. Res.*, 94, 18,095-18,117, 1989.

Thomas, A.C., P.T. Strub, and P. Brickley, Anomalous satellite-measured chlorophyll concentrations in the northern California Current in 2001-2002, *Geophys. Res. Lett.*, 30(15), 8022, doi:10.1029/2003GL017409, 2003.

Vazquez, J., K. Perry, and K. Kilpatrick, NOAA/NASA AVHRR oceans pathfinder sea surface temperature data set user's reference manual, version 4.0, *Jet Propulsion Laboratory Pub.*, 74 (D-14070), Jet Propulsion Laboratory, Pasadena, California, 1998.

Venrick, E., S.J. Bograd, D. Checkley, R. Durazo, G. Gaxiola-Castro, J. Hunter, A. Huyer, K.D. Hyrenbach, B.E. Laveniegos, A. Mantyla, F.B. Schwing, R.L. Smith, W.J. Sydeman, and P.A. Wheeler, The state of the California Current, 2002-2003: Tropical and subarctic influences vie for dominance, *CalCOFI Rep.*, 44, 28-60, 2003.

Wald, L., Some examples of the use of structure functions in the analysis of satellite images of the ocean, *Photogramm. Eng. and Rem. Sens.*, 55, 1,487-1,490, 1989.

Walker, A.E., and J.L. Wilkin, Optimal averaging of NOAA/NASA Pathfinder satellite sea surface temperature data, *J. Geophys. Res.*, 103, 12,869-12,883, 1998.

Webster, R., and M.A. Oliver, *Geostatistics for environmental scientists*, John Wiley, Chichester, 2001.

Wheeler, P.A., A. Huyer, and J. Fleischbein, Cold halocline, increased nutrients and higher chlorophyll off Oregon in 2002, *Geophys. Res. Lett.*, 30(15), 8021, doi:10.1029/2003GL017395, 2003.

Winant, C.D., Beardsley, R.C., and R.E. Davis, Moored wind, temperature, and current observations made during Coastal Ocean Dynamics Experiments 1 and 2 over the northern California continental shelf and upper slope, *J. Geophys. Res.*, 92, 1,569-1,604, 1987.

Winant, C.D., and C.E. Dorman, Seasonal patterns of surface wind stress and heat flux over the Southern California Bight, *J. Geophys. Res.*, 102, 5,641-5,653, 1997.

Yashayaev, I.M., and I.I. Zveryaev, Climate of the seasonal cycle in the North Atlantic and the North Pacific oceans, *Int. J. of Climatology*, 21, 401-417, 2001.

Yoder, J.A., C.R. McClain, J.O. Blanton, and L.-Y. Oey, Spatial scales in CZCS-chlorophyll imager of the southeastern U.S. continental shelf, *Limnol. Oceanogr.*, 32, 929-941, 1987.

Yoder, J.A., J.E. O'Reilly, A.H. Barnard, T.S. Moore, and C.M. Ruhsam, Variability in coastal zone color scanner (CZCS) chlorophyll imagery of ocean margin waters off the U.S. East Coast, *Cont. Shelf Res.*, 21, 1,191-1,218, 2001.

APPENDICES

Appendix A

EMPIRICAL ORTHOGONAL FUNCTION ANALYSIS OF SEMIVARIANCE DATA

Consider a semivariance data set of M semivariograms, each comprised of K semivariance estimates and each calculated at a different location. The data set is therefore comprised of a set of K spatial maps, each with M pieces of data. When performing an EOF analysis of a two-dimensional data set, one data dimension is treated as the dimension in which structure is defined; the second is treated as the dimension through which structure is sampled. Having defined lag time as the structuring dimension and space as the sampling dimension, EOF analysis seeks to express the semivariogram $\hat{\gamma}_m(h)$ calculated at some location x_m as the weighted sum of K empirical orthogonal functions (EOFs) $e_k(h)$, for k=1, 2, …, K, such that

$$\hat{\gamma}_m(h) = \sum_{k=1}^{K} a_k(x_m) e_k(h) \tag{1}$$

where $a_k(x)$ is the spatial amplitude function or principle component corresponding to the k^{th} orthogonal function. In this context, the semivariogram at location x_m is expressed as a linear combination of K functions $e_k(h)$, whose contributions are determined by K location dependent amplitude functions evaluated at x_m. For each EOF, the amplitude function $a_k(x)$ constitutes a spatial map of coefficients which define the relative contribution of that EOF to the structure of the original semivariograms calculated at all locations. The set of K amplitude functions constitutes a second set of orthogonal structures. As defined by the analysis, the K functions e_k form a basis set that explains as

much data structure or variance as possible with the fewest possible functions. This constrains the location-dependent amplitudes to be uncorrelated over the data set so that

$$\frac{1}{M}\sum_{m=1}^{M} a_k(x_m)a_l(x_m) = \lambda_k \delta_{kl} \tag{2}$$

where

$$\delta_{kl} = \begin{cases} 1, & l = k \\ 0, & l \neq k \end{cases} \tag{3}$$

and

$$\lambda_k = \frac{1}{M}\sum_{m=1}^{M} a_k(x_m)^2 \tag{4}$$

is the variance explained by the k^{th} structure.

As described by Kutzbach [1967], the mathematics behind EOF analysis can be readily developed from the desire to describe a data set within a coordinate system in which a maximum amount of variance is explained by a minimum number of coordinate directions. Consider the data set described above as a K x M matrix Y_{km}. Each of the M columns corresponds to one of the M semivariograms of length K, and each of the K rows corresponds to the set of M semivariance estimates for one of the K time lags considered. Define the matrix P by removing the mean semivariance from each of the columns of the data matrix Y and then standardizing the data by dividing each de-meaned semivariogram by its standard deviation:

$$P_{km} = \frac{Y_{km} - \frac{1}{K}\sum_{k=1}^{K} Y_{km}}{\left[\frac{1}{K-1}\sum_{k=1}^{K}\left(Y_{km} - \frac{1}{K}\sum_{k=1}^{K} Y_{km}\right)^2\right]^{\frac{1}{2}}} \tag{5}$$

Each column of P can be thought of as a K-element vector lying within a K-dimensional coordinate system. We wish to define a column vector e as having the greatest possible similarity to the sample set of vectors that constitute our de-meaned and standardized data matrix P. The unknown vector e can be determined by maximizing its squared projection onto the data matrix P. In order to ensure that the squared projection is not biased by the size of the data set, we must divide the projection by the sample size K so that we maximize the value

$$\frac{\left(e^T P\right)^2}{K} = \frac{e^T P P^T e}{K} \tag{6}$$

where e^T and P^T are the transposes of the vector e and matrix P. Maximization of equation (6) should be subject to the constraint that the vector e has unit length ($e^Te = 1$) so that the projection cannot be made arbitrarily large simply by defining e to be arbitrarily long. Given this constraint, the similarity between e and the set of observation vectors will be determined by the orientation of e alone. Now let $C_P = (K^{-1})PP^T$. Then we are seeking to maximize

$$e^T C_P e \tag{7}$$

subject to the condition that $e^Te = 1$. Notice that the K x K matrix $C_P = (K^{-1})PP^T$ provides a measure of the dispersion of the data set across the sampling dimension, which in this case is taken to be space. C_P is in fact the correlation matrix of the K time lags as defined by variation in space. Each element of C_P is a correlation computed from two spatial maps or two rows of the original semivariance data matrix Y.

In order to find a solution to the maximization of equation (7), define λ to be the maximum value of the squared projection, or equivalently, the amount of data variance explained by the vector e. We seek a solution to the equation

(8) $$e^T C_P e = \lambda$$

or

(9) $$C_P e = e\lambda$$

which can be recognized as an eigenvalue problem. The normalized vector or function which is most representative of the data is the eigenvector e of the matrix C_P corresponding to the eigenvalue λ. In keeping with the definition of λ as a squared projection or variance, the eigenvalues of the real symmetric matrix C_P are guaranteed to be non-negative. An EOF analysis amounts to an eigenanalysis of the matrix $C_P = (K^{-1})PP^T$ wherein all K eigenvectors e_k and all K eigenvalues λ_k are determined by solution of the K linear equations

(10) $$C_P e_k = e_k \lambda_k$$

or

(11) $$(C_P - \lambda_k I)e_k = 0$$

for k=1,2,...,K, where I is the K x K identity matrix. In matrix notation, EOF analysis seeks a solution to

(12) $$C_P E = \Lambda E$$

where E is a K x K orthogonal matrix whose columns are the eigenvectors e_k, and Λ is a K x K matrix whose diagonal elements are the eigenvalues λ_k and whose off-diagonal elements are zeros.

Solution of equation (12) yields a basis set of K orthonormal vectors, the EOFs, which can be used to form an alternative expression of the data set provided we have the K weighting vectors or spatial amplitude functions $a_k(x_m)$. The set of amplitude functions

can be readily derived by projecting the set of eigenvectors or EOFs onto the data matrix P. Let

(13) $$A = E^T P$$

where A is a K x M matrix whose rows are the M-element amplitude functions or principle components $a_k(x_m)$. Because E is an orthogonal matrix, $EE^T = I$, and

(14) $$P = EA$$

Notice that multiplication by the transposed eigenvector matrix in equation (13) defines a linear transformation of the data into a coordinate system defined by the orthonormal basis set of eigenvectors. Transformation of the K de-meaned semivariograms by the linear operator defined by E^T yields the K principle components $a_k(x_m)$. Within the new coordinate system, the correlation matrix C_P becomes the diagonal eigenvalue matrix Λ. Because the correlation matrix C_P is diagonalized by the transformation, variability along different axes of the new coordinate system is uncorrelated. In other words, the eigenvectors define directions within the old coordinate system along which variability in one direction is uncorrelated with variability in another. The set of K EOFs and corresponding amplitude functions define a set of K statistical modes of variability which collectively partition the structure of the de-meaned and standardized semivariograms of P.

The fraction of overall variance explained by any one EOF mode is equivalent to the amount of variance operating along the direction defined by the eigenvector e_k within the original coordinate system, and this quantity is given by the ratio of the eigenvalue λ_k to the trace of the eigenvalue matrix Λ. The trace of Λ is equal to the trace of the correlation matrix C_P, which is the sum of the data variances given by

(15) $$\sum_{k=1}^{K} \lambda_k = \sum_{m=1}^{M} \left[\frac{1}{K} \sum_{k=1}^{K} {P_{km}}^2 \right]$$

The EOF modes are generally ordered according to the amount of variance they explain. The first mode explains the greatest amount of overall variance; the second mode explains the greatest amount of the remaining variance not explained by the first, and so on.

Appendix B

RESCALING SEMIVARIANCE CALCULATED FROM LOG-TRANSFORMED DATA

Consider a realization of a lognormal random process $z(t_i)$, i=1,2,...N, having mean μ_z, variance σ_z^2, autocorrelation function ρ_z, and semivariogram γ_z. The variable $y(t) = \ln z(t)$ is normally distributed with mean μ_y, variance σ_y^2, autocorrelation function ρ_y, and semivariogram γ_y. The n^{th} moment of the lognormal variable z is given by the expression

$$E(z^n) = \exp\left(n\mu_y + \frac{n^2\sigma_y^2}{2}\right) \tag{1}$$

where $E(\cdot)$ denotes the expectation function. It follows that the mean and variance of z are given by

$$\mu_z = \exp\left(\mu_y + \frac{\sigma_y^2}{2}\right) \tag{2}$$

and

$$\begin{aligned}\sigma_z^2 &= \mu_z^2\left[\exp(\sigma_y^2) - 1\right] \\ &= \exp(2\mu_y + \sigma_y^2)\left[\exp(\sigma_y^2) - 1\right]\end{aligned} \tag{3}$$

respectively. From Mejía and Rodríguez-Iturbe [1974], the autocorrelation functions of y and z are related according to the equation

$$\rho_z = \frac{\exp(\sigma_y^2\rho_y) - 1}{\exp(\sigma_y^2) - 1} \tag{4}$$

The autocorrelation function ρ_z is related to the semivariogram γ_z by

(5) $$\rho_z = 1 - \frac{\gamma_z}{\sigma_z^2}$$

or

(6) $$\rho_z = \frac{\gamma_z}{\exp(2\mu_y + \sigma_y^2)[\exp(\sigma_y^2) - 1]}$$

by substitution of equation (3). Similarly, we have

(7) $$\rho_y = 1 - \frac{\gamma_y}{\sigma_y^2}$$

Substituting equations (6) and (7) into equation (4) and simplifying yields the following expression relating the semivariogram of the ln-transformed variable y to the semivariogram of the lognormal variable z:

(8) $$\gamma_z = \exp(\mu_y)[\exp(2\sigma_y^2) - \exp(2\sigma_y^2 - \gamma_y)]$$

Assuming the sills of the semivariograms γ_z and γ_y to be equal to the overall variances σ_z^2 and σ_y^2, the sill of the ln-transformed process y can be rescaled into the data units of z by substituting the sills as measures of semivariance to obtain

(9) $$\sigma_z^2 = \exp(\mu_y)[\exp(2\sigma_y^2) - \exp(\sigma_y^2)]$$

where σ_z^2 and σ_y^2 are taken to be the sills of the semivariograms of z and y. Similar expressions can be derived for other discrete values of semivariance, including nugget estimates.

BIOGRAPHY OF THE AUTHOR

Kasey Legaard was born in Twin Falls, Idaho on April 26, 1978. He was raised in Pocatello, Idaho and graduated from Pocatello High School in 1995. He attended Idaho State University and graduated in May of 2001 with Bachelor degrees in Biology and Mathematics with a Computer Science Emphasis. He moved to Maine in August of 2001 to enter the Oceanography graduate program at The University of Maine. After receiving his degree, Kasey will pursue a Ph.D. in the Department of Forest Management at The University of Maine.

Kasey is a candidate for the Master of Science degree in Oceanography from The University of Maine in December, 2004.